Author:
Dlaka, David

Title:
Designing bright single photon sources with low Q-factors at telecom O band wavelengths

Designing bright single photon sources with low Q-factors at telecom O band wavelengths

By

David Dlaka

University of Bristol

Department of Physics

A dissertation submitted to the University of Bristol in accordance with the requirements of the degree of *Master of Science by Research* in the Faculty of Science. October, 2020

Author's Declaration

I declare that the work in this dissertation was carried out in accordance with the requirements of the University's Regulations and Code of Practice for Research Degree Programmes and that it has not been submitted for any other academic award. Except where indicated by specific reference in the text, the work is the candidate's own work. Work done in collaboration with, or with the assistance of, others, is indicated as such. Any views expressed in the dissertation are those of the author.

David Dlaka

Abstract

Bright quantum dot single photon sources (SPS) have mostly relied on coupling to optical cavities with high quality (Q) factors. Since the Q-factor represents the damping of the optical resonator in time, which can be shown to correspond to the resonance spectrum width[1], bright sources with high Q-factors rely on the (small) probability of a quantum dot emitting within the very narrow resonance peak. In this thesis I have investigated the possibility of bright emission from emitters in low-Q cavities, which are easier to fabricate and result in a higher device yield than their high-Q counterparts. With the use of computerised numerical modelling methods such as the finite-difference time-domain (FDTD) method and the transfer matrix method (TMM) I have investigated two types of devices: optical micropillars, and emitters exploiting Tamm Plasmons (TPs).

In my inspection of the properties of Tamm Plasmon based emitters, I focused on the photonic properties of the interface between the metal and cavity (spacer). I show that multiple values of the metal and spacer thickness can result in the same Tamm eigenfrequency. This in turn allows me to account for spectral detuning of the Tamm mode when the metal thickness is varied, which can cause brightness filtering. This reveals considerable effects of the metal layer on the absorption and side emission, the two most significant loss channels. Significant effects on the far-field of the emission within optic fibre collection angles (NA$\leq$0.22) are also shown. By demonstrating differences in the total extraction efficiency of up to 75% of the peak value within the range considered, I demonstate the benefits of optimising TP structures with the metal-spacer interface in mind.

By simulating a variety of micropillars, I examine the visible effects of the changing physical structure on the cavity quantum electrodynamics (QED). By optimising the active coupling to the cavity with the diameter I demonstrate the theoretical possibility of high-β ($> 90\%$) low-Q ($\approx 10^2$) micropillars. I then demonstrate how the passive efficiency of the cavity mode depends on the ratio of the top and bottom DBR trans-

[1]The Q-factor can be mathematically defined as Q = λ/FWHM

missivity, and that internally efficient pillars can be designed with Q-factors in the low 1000s. I also demonstrate the theoretical possibility of exctracting over 80% of QD created photons within numerical apertures easily reached by bulk optics.

Acknowledgements

This work wouldn't have been possible without the supervision of Dr. Edmund Harbord and Prof. Ruth Oulton. With the guidance and support they've provided in these past two years, which has gone above and beyond reasonable expectations, I was able to better myself not just as a physicist and researcher, but also as a person. I consider myself extremely privileged to have been given the opportunity to benefit from their exemplary mentorship and I feel honoured to have worked in this research group.

I also have to express gratitude to Huili Hou, through whom I was first introduced to FDTD simulations which would eventually become a central topic of my master's thesis. I learned a lot during our work on imaging and aligning optical fibres to Tamm Plasmon microchips. I'd also like to thank other member of the group with whom I've worked, whose feedback and assistance throughout this project has been very valuable.

On a personal note, I would like to thank my family and friends for the constant love and encouragement they've provided. Particular gratitude is expressed to my dear friend Jovan, who endured too many hours of me talking about this research (despite him not being a physicist).

Finally, I would like to thank the Ministry of Education and Science of the Republic of North Macedonia for funding my MSc studies in the form of a scholarship. Without their patronage I would not have been able to pursue a masters degree at a world-class research institution. I'd also like to acknowledge the research funding provided by the UKRI as parts of the "Project 1D QED" (EP/N003381/1) and "Spin Space" (EP/M024156/1) grants.

Contents

Introduction

Current communication machines rely on a constant supply of electric current to use for computation and memory storage. In a similar way, quantum information technology requires a reliable source of photons to operate, and an on-demand single photon source (SPS) which successfuly meets certain criteria has many quantum communication applications. Some of these include: quantum key distribution (QKD), where a bona fide SPS would eliminate the need for security protocols when using attenuated lasers[1]; as qubits in linear optical quantum computing despite poor photon-photon interactions [2]; or in quantum metrology, where states of many entangled photons can be used to beat the classical limit of precision $N^{-\frac{1}{2}}$[3].

As a result, the design and optimisation of efficient[1] SPS devices is an active field of research. Although micropillars have been demonstrated to be bright sources, they have often relied on strong coupling to cavities with high Q-factors. In order to be scalable, any bright single photon source would benefit significantly from a lower quality factor. This is because low-Q cavities can result in significantly higher device yields and are simpler and cheaper to make. In this text, I examine two types of emitters which potentially satisfy these requirements: Tamm Plasmon (TP) based emitters (which are low-Q, but not sufficiently bright), and optical micropillars (which traditionally have used high-Q cavities to achieve high efficiencies). By calculating the brightness[2] of the device while changing some of the structural parameters, I show novel optimisations of Tamm Plasmon devices, as well as demonstrate the theoretical possibility of micropillar cavities with low quality factors.

[1]The efficiency of a component is the ratio of successful output events to input events. Regarding emitters, the efficiency is defined as the number of emitted (produced) single photons per external trigger (i.e. input event).

[2]The brightness of an emitter is the value of single photons successfully extracted (within some numerical aperture) for each external trigger.

1.1 Tamm Plasmon Emmitters

One method of extracting photons from a quantum dot is by coupling to an optical Tamm mode. These devices could potentially be fibre-coupled, as they utilise flat metal discs on distributed Bragg reflectors to create an optical cavity, resulting in the excitation of confined surface modes which can be extracted on the air side. An advantage of such a device over current state-of-art micropillar devices would be the significantly simpler production of physical samples, as there is no need for any etching. Furthermore, the structures are more robust and only require the deposition of a metal film on top of the self assembled dielectric photonic crystal; these discs are a fraction of the thickness of the other layers resulting in a lack of any elements "sticking out" considerably. However, the brightness of such devices is impeded by the absorption in the metal, as well as considerable side losses due to weaker coupling into the cavity mode.

One part of this thesis is an exploration of the properties of these surface states between metal and dielectric surfaces (below the metal plasma frequency) called optical Tamm states, or Tamm plasmons (TPs)[4], in relation to their suitability for use as SPS emitting mechanisms. It has been established both in theory and experiment that eigenfrequencies of the Tamm plasmon depend on both the thickness of the metal and the dielectric layer on which it's deposited (refered to as the spacer layer). However, to the best of the author's knowledge, there has been no direct comparison[3] between devices with different metal and spacer thicknesses, but the same eigenfrequency for the Tamm mode. One challenge faced by TP SPS devides is the existence of a significant loss channel in the absorption of the metal, caused by the high imaginary part of the refractive index. Previous research on absorption in thin metals suggests that the imaginary part of the film's refractive index can decrease as more metal is deposited[5]; further to this, absorption in thin metal films has been found to "peak" at a thickness on the order of 10 nm[6], suggesting that variations in the film thickness in this range could reduce the loss of emitted single photons into the metal i.e. increase the passive device efficiency. The focus of this research is to answer the question of whether there are any possible advantages of choosing one pair of metal and spacer depths which over another (which results in the same λ_{TP}) in terms of the SPS efficiency. Structures which result in eigenfrequencies within the telecomms O band ($\lambda \approx 1300$ nm) have been examined.

[3] In terms of their applicability as single photon sources

1.2 Optical Micropillars

Optical micropillars, formed by a quantum-dot containing "cavity" layer sandwiched between two distributed Bragg reflectors have been a popular choice of deterministic single photon source due to their high brightness and low multi-photon probability. By placing distributed Bragg reflectors on top and botom of an optical cavity, the energy leakage of the cavity modes is decreased, and by etching away the sides to leave only a cylindrycal structure resting on a substrate, the field around the emitter is spatially contained. These effects contribute in various ways to the active coupling to the cavity, as well as the passive efficiency. Micropillar cavities with efficiencies as high as $> 65\%$ have been demonstrated [7]. Optical micropillars have also been demonstrated to be well suited as QIT SPS devices by demonstrating significant brightness ($> 65\%$) while simultaneously displaying high purity ($> 99\%$) and indistinguishability[4] ($> 98\%$)[8].

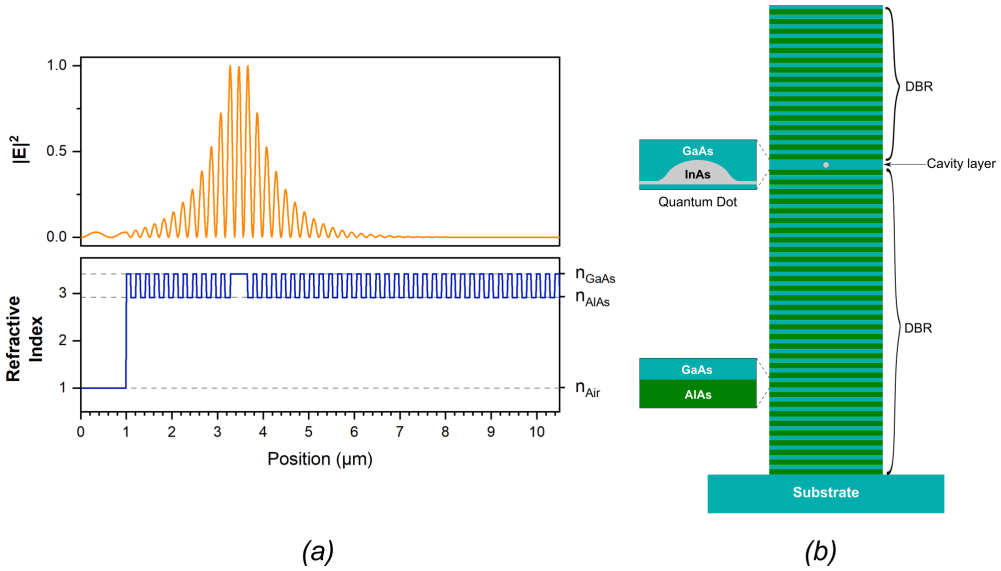

Figure 1.1: *(a) The dielectric and E-field structures of an optical micropillar, calculated with the transfer matrix method (See section 3.2); (b) The physical structure of a typical GaAs/AlAs micropillar, showing the location of the InAs quantum dot within the cavity and the top and bottom distributed Bragg reflectors.*

Part of this thesis addresses the underlying quantum electrodynamics to explain why and how micropillar cavities enhance both brightness and spontaneous emission rate. By pointing out some differences between atomic and micropillar emitters, I claim that some previous techniques of calculating the theoretical brightness of low-Q micropillars could be less accurate than previously thought and that bright low-Q

[4]Indistinguishability can be thought of as the degree of similarity between photons. Perfectly indistinguishable photons have the same wavelength and polarization, as well as temporal and spatial extent. This is further discussed in Sec. 2.1.1

micropillars are indeed plausible. While not as easy to manufacture as Tamm Plasmon devices, micropillars have a significantly higher brightness, but at significantly higher Q-factors. In this text I have investigated low-Q micropillars, made up of fewer stacked DBR layers. These structures are both easier to make, less susceptible to physical stresses, and result in a cavity resonace which is spectrally wider, making them of particular interest to researchers. My goal in researching this type of optical resonator is to see whether micropillars can be low-Q and bright enough to replace equivalently bright but non-deterministic single photon sources.

1.3 Thesis Overview

In Chapter 2, I present the theoretical background behind some of the concepts relevant to this thesis. We begin at the production of the photon in a quantum dot due to the semiconductor band properties and how the placement of the emitter in an optical resonant cavity affects the quantum mechanical properties of the system. In this part I introduce concepts, such as the Purcell enhancement, which are later used to explain my results and conclusions. This is followed by a discussion on how electromagnetic fields interact at boundaries, giving rise to surfact states such as surface plasmon polaritons (SPPs), before concluding with an explanation of the dispersive properties which explain how the emitted light couples into the Tamm plasmon mode, and is later emitted.

Chapter 3 consists of an explanation of modelling techniques used to calculate the various metrics by which the efficiency of a SPS are measured. A formalisation of the transfer matrix method, which is used to solve for the eigenmodes of the Tamm plasmon for a wide span of metal and spacer layer thicknesses is presented. Following this is a brief explanation of the physics behind FDTD simulations, as well as how Yee's technique of truncated voxel grids for the E and H fields allows for a leap-frog method of solving Maxwell's equations. The chapter ends with a discussion on the tools used by the commercial FDTD solver used[9] to realistically and efficiently simulate the CTP structure, such as the conformal meshing techniques, or the use of perfectly matched layers (PMLs).

In Chapter 4, I present results of my investigation in Tamm Plasmon effects. Reflectivity data obtained by the TMM is used to establish the set of metal and spacer heights which result in $\lambda_{TP} = 1300$nm; for convenience of reference, I've called this set the metal-spacer relationship (MSR). Three dimensional FDTD simulations are then used to simulate various structures where the metal height is changed between 0-35nm and the spacer is chosen accordingly for each structure according to the MSR, and the perrformance of these devices is compared; further comparisons to a detuned device

are also presented. After a discussion of the changes in the far-field and the extraction efficiency, the chapter concludes with a closer look at the structure of the fields in the structure with the peak performance.

Results from optimisations of micropillars at both low and high Q-factors are presented in Chapter 5. I show how the diameter of the structure determines the ratio at which Purcell enhancement translates to brightness, and can therefore be selected first. This is followed by results that support discussions in the second chapter, which show both why previous estimations of low-Q pillar brightness are incorrect as well as demonstrate their plausibility as bright emitters.

Single Photon Sources in Optical Resonators

2.1 Quantum Dots as Single Photon Emitters

2.1.1 Single Photon Sources (SPS)

When work by Planck, and 5 years later in 1905 by Einstein, suggested that light is quantised in singular energy packets[10][11](later called photons), our grip on the hidden rules behind our universe got broken in most anti-intuitive ways. The human experience is very much a classical[1] and continuous one, where quantum effects such as superposition, tunneling, or entanglement are not observed [12][13][14]. It is exactly these strange concepts however, among others, which are core mechanisms in humanity's attempt to build a quantum computer.

Quantum communication machines relies on the properties of single photons, and as such cannot exist without a reliable single photon source. While there are multiple types of single photon sources, such as attenuated lasers[15][16], or by photon pair production [17][18], this thesis is concerned with single quantum emitters which can can produce one and only one photon when stimulated. A more formal way to state this would be to use number states called Fock states. In these terms, a state of light can be described by

$$|\gamma\rangle = \sum_i p_i |i\rangle \tag{2.1}$$

where p_i is the normalised probability coefficient for the $|i\rangle$ state, which results in the emission of i photons. A coherent source can therefore[19] be described by

$$|\alpha\rangle = e^{-\alpha^2/2} \sum_n \frac{\alpha^n}{n!} |n\rangle \tag{2.2}$$

where $|\alpha|^2$ is the mean photon number of the Poisson distribution of photons. In an optically stimulated (triggered) atom-like single photon source, an incoming laser pulse

[1] In the photonic context of the word.

is converted into a single photon stream whose Fock state can be described as

$$|\gamma_{SPS}\rangle = |1\rangle \tag{2.3}$$

One commonly studied on-demand source of single photons are atoms, both natural and artifical atom-like configurations. While the first demonstrations of single photon emission was from sodium atoms[20], researchers had been searching for more tunable alternatives where the intrinsic properties of atoms wouldn't be a limiting factor in SPS device design. First shown at the turn of the millenium[21], epitaxial self-assembled semiconductors quantum dots (QDs) have been a popular alternative due to their tunability.

SPS quality criteria

There are certain criteria which are important for an acceptable SPS to meet for use in quantum information technology. The most obvious one is that only a single photon is emitted, decribed by a property called anti bunching. This is verified with a photon intensity autocorrelation measurement, labeled $g^{(2)}(\tau)$. This metric, which is the second order correlation function, describes the probability of detecting a photon in one channel after detecting a photon in another, with a time delay τ between the first and second detection. For $\tau = 0$, it describes the probability of detecting a photon in both channels at the same time. For a coherent source (for instance, a laser operating far above threshold) $g^{(2)}(0) = 1$, whereas it can be shown that for a single-mode thermal field $g^{(2)}(0) = 2$. In strong contrast to this, we expect for a true single photon source, $g^{(2)}(0) = 0$; this can be understood as there being zero probability of a simultaneous detection in both channels due to there existing only one photon. As such, $g^{(2)}$ is the most important metric in demonstrating anti bunching in a veritable SPS[22].

It is impossible to build a lossless single photon source, at the very least due to the finite resolution of manufacturing methods. Therefore, each photon created in a single photon source is either emitted and collected by some optical system, or is not successfuly extracted and is therefore lost. The brightness of a single photon source can be thought of as the proportion of excitations that lead to a single photon emited[2] by the system. For quantum computation, it is sufficient to have a combined efficiency (product) of the source and detector which is $> \frac{2}{3}$ [23]. The optimisation of brightness in SPS devices is therefore an active research field of interest to the development of quantum computers. This thesis is among the works which deal with the maximisation

[2]Emited here is taken to mean "into channels resulting in the extraction of the photon"; a created photon which couples into a loss channel is not thought to be "emited" in this context.

of SPS device efficiency.

It is also necessary that the photons emitted are completely indistinguishable. It was discovered in the late 1980s that photons cannot give rise to a fully distructive interference unless they're in the exact same mode. This was first noticed when two photons incident on a 50%/50% beam splitter at the same time display "bunching" - both photons exit through the same port every time., due to the Bose-Einstein statistics of the photons [24][25]. This effect is avoided if the photons are truly indistinguishable, making indistinguishability of particular importance for linear quantum computing applications. What's more, indistinguishable photons are needed for the operation of quantum repeaters, making long distance quantum information heavily reliant on single photon sources with a high degree of indistinguishability. While in theory a SPS can have perfect indistinguishability of emitted photons, dephasing and further unwanted changes originating in the system could cause photons to beome less indistinguishable, and as such this is an important factor in SPS device design.

Quantum information theory relies on testing the states of photons. There is a non-zero probability that a photon in one state can successfully identify as another when probed, depending on the closeness of the states in Hilbert space. This unwanted effect is quantified by the system's fidelity, a metric which quantifies how close two states are first defined in 1993 [26]. Another important factor in QIT is the measure of the purity of a normalised quantum state, a measure of how "mixed" a state is. It is defined as $\gamma \equiv \mathrm{tr}(\rho^2)$, where ρ is the density matrix of the state, and can be thought of as the degree to which the density operator can be described with only one term [27].

With the methods used in this thesis, it is only possible to accurately model the device brightness, and as such the other metrics while important to the field, are not of relevance to this text.

2.1.2 Quantum Dots

Quantum dots are devices comprised of two types of slightly different semiconductor. By suspending a small volume[3] of a low band gap semiconductor in a high band gap semiconductor, a quantum well with discrete atom-like transition levels is created. Common dielectrics used in quantum dots are InAs and GaAs, where the dots can be epitaxially self-assembled under Stranski-Krastanov growth[28].

It can be shown that the Hamiltonian of the quantum dot system can be expressed as

[3] On the order of $\approx$ few nm across

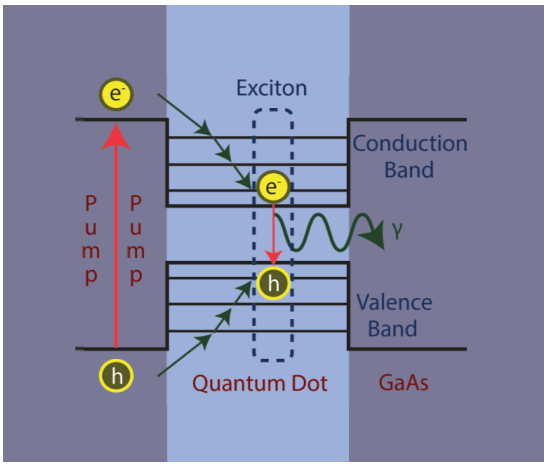

Figure 2.1: *An illustration of the single photon emission process within a quantum dot. The wetting layer (see end of section 2.1) is not shown.*

$$H = H_e + H_h + H_c \tag{2.4}$$

$$H_e = -\frac{\hbar^2}{2}\nabla\left(\frac{1}{m_{eff,e}}\nabla\right) + V_e(\vec{r}) \tag{2.5}$$

$$H_h = -\frac{\hbar^2}{2}\nabla\left(\frac{1}{m_{eff,h}}\nabla\right) + V_h(\vec{r}) \tag{2.6}$$

$$H_c = -\frac{e^2}{4\pi\varepsilon}\frac{1}{|r_e - r_h|} \tag{2.7}$$

where e stands for electron, h for hole, and c for the Coulomb interaction[29]. Because there are many quantum dots within the wetting layer, we model $V(\vec{r})$ as harmonic in the x-z plane, and an infinite potential well in the y direction such that we can define it as

$$V(x,y,z) = \begin{cases} \frac{m_{eff}\omega_0^2}{2}(x^2+z^2) & \text{for } y \le L \\ \infty & \text{for } y > L \end{cases} \tag{2.8}$$

where m_{eff} corresponds to $m_{eff,e}$ in V_e and to $m_{eff,h}$ in V_h. The Hamiltonian therefore has energy levels

$$E = (n_x + n_z + 1)\hbar\omega_0 + \frac{1}{2m_{eff}}\left[\frac{\pi\hbar n_y}{L}\right]^2 \tag{2.9}$$

with envelope wavefunctions

$$\psi_{envelope}(x,y,z) \propto H_{n_x}(x)H_{n_z}(z)e^{-\frac{V(x,y,z)}{\hbar\omega_0}}\sin\left(\frac{\pi n_y y}{L}\right) \tag{2.10}$$

where $V(x, y, z)$ is represented in Eq.(2.8), and n_x, $n_z \in \mathbb{N}^0$ while $n_y \in \mathbb{Z}^+$.

In Eq.(2.9), the first term corresponds to harmonic oscillators in the x and z directions; the second describes the infinite potential well in the y direction. To include the Coulomb interaction to this expression, we use pertubation theory[30] to obtain

$$\Delta E_0 = \langle 0| H_c |0\rangle + \sum_i \frac{|\langle 0| H_c |i\rangle|^2}{E_i - E_0} \tag{2.11}$$

where $|i\rangle$ denotes the excited non-pertubated eigenstates, with corresponding eigenenergies E_i.

As such, upon an external excitation, which can be electrical or optical, an electron is excited from the valence to the conduction band of the dielectric in which the quantum dot exists. The Coulomb interaction can be sufficiently high such that the electron and hole pair form the bound exciton state. The potential well in the QD is deeper than the surrounding volume, and the exciton is localised to this well as it non-radiatively degenerates, before a photon is emitted as the result of the s-, p-, or higher transitions [29].

In epitaxial quantum dots grown with the Stranski-Krastanov process, differences in the crystal lattices of InAs and GaAs cause strain i.e. elastic energy at the boundary. As atoms get layered onto the structure, there's an increase in the elastic energy which eventually results in the formation of separated clusters (the quantum dots themselves) linked only by a thin layer of atoms near the base of the InAs islands. This thin film which connects the quantum dots is the wetting layer, which emits photons at a wavelength distinct from the dots and, due to an increase in the confining potential width, reduces the energy gap between the hole state and confined electron state [31].

2.2 Cavity Quantum Electrodynamics (QED)

While quantum dots are very attractive single photon sources, extracting emitted photons requires some form of resonant cavity to enchance emission a desired direction while supression emission into loss channels. However, by placing the emitter in an optical resonant cavity, we expose it to the surrounding E field within the structue; the changes brought on by the interaction between the emitter and field need to be taken into consideration as it affects both the directionality and rate of emission[4].

[4]The speed of an emitter is also an important feature; however, it's not within the relevance of this thesis.

2.2.1 Emitter-Cavity Coupling

By treating the emitter as a two level system (with ground and excited states $|g\rangle$ and $|e\rangle$) which is close to resonance with a fundamental optical cavity it's located in, we can expressed the Hamiltonian of the coupled source-cavity system as

$$H = H_E + H_F + H_{Int} \tag{2.12}$$

where H_E and H_F are the emitter and field Hamiltonians, while H_{Int} represents the interaction between the emitter and cavity field. While a full treatment of this Hamiltonian, called the Jaynes-Cummings Hamiltonian, is outside of the scope of this thesis (See Appendix A), it is enough to understand that H_{Int} depends on the *emitter-field coupling parameter* g($\vec{r}_E$) (where $\vec{r}_E$ is the position vector of the emitter), which can be described by

$$g(\vec{r}_E) = g_0\psi(\vec{r}_E)\cos(\zeta) \tag{2.13}$$

The coupling parameter $g(\vec{r}_E)$ consists of the Rabi frequency $g_0 \propto \sqrt{\hbar\omega/V_{Mode}}$, meaning that higher-order transitions and more spatially confined fields result in stronger coupling. There's also the position dependent parameter $\psi(\vec{r}_E) = E(\vec{r}_E)/E(\vec{r}_M)$ (where $\vec{r}_M$ is the position where $|E|$ is at maximum) which shows that for optimal coupling, the source should be placed at the peak of the E-field. Finally, the polarization dependent part $\cos(\zeta)$ depends on the angle between the dipole moment of a transition and the direction of the E-field at the source, showing that in the optimal case the two vectors are aligned. These conclusions are relevant to the placement and orientation of the dipole source used in this thesis as described in section 3.3.2.

It can be shown that the eigenfrequencies of the coupled emitter-field system have eigenenergies

$$E_\pm = \hbar\omega(n+1) \pm \sqrt{\left(\frac{\hbar\delta}{2}\right)^2 + \hbar^2|g|^2(n+1)} \tag{2.14}$$

where the atom-cavity detuning is represented by $\delta = \nu - \omega$, and ν is the atom mode-, whereas ω is the cavity mode frequency. Setting the ground state for the field and atoms at zero, we get the energy eigenvalues

$$\frac{E_\pm}{\hbar} = \frac{(\omega+\nu)}{2} \pm \sqrt{\left(\frac{\delta}{2}\right)^2 + |g|^2} \tag{2.15}$$

An inevitability in optical resonators is the existence of loss channels. This is usu-

ally spontaneous emission into non-emissive modes[5] or decay without radiation, such as absorption due to the presence of a metallic material. Emission into lossy channels is labeled γ, and the cavity field decay rate is κ.

The conventional way to represent losses is to introduce a complex component to the mode frequencies such that

$$\begin{aligned} \nu' &= \nu - i\gamma \\ \omega' &= \omega - i\kappa \end{aligned} \tag{2.16}$$

It can be shown that the eigenfrequencies $\omega_\pm$ of a strongly coupled system can be expressed by

$$\omega_\pm = \frac{\omega+\nu}{2} - i\frac{\kappa+\gamma}{2} \pm \sqrt{\left(\frac{\delta - i(\kappa-\gamma)}{2}\right)^2 + |g|^2} \tag{2.17}$$

such that $\mathrm{Re}(\omega_\pm)$ is the eigenmode frequencies, while $\mathrm{Im}(\omega_\pm)$ represents the damping, i.e. loss [32]. At this point, we recognise two regimes:

- **Strong coupling:** also known as the high Q-factor regime, this corresponds to a coupling strengh g comparatively larger than losses such that $g > \frac{\kappa}{2}$ and $\kappa >> \gamma$. Such devices are not of particular relevance to this text.
- **Weak coupling:** also known as the low Q-factor regime, reflects conditions resulting in domination of the cavity field decay such that $\frac{\kappa}{2} >> g >> \gamma$. This has been further expanded on below.

Weak coupling and Purcell enchancement

We begin by considering a weak interaction between the emitter and the cavity field in a system with little detuning, meaning $\delta = 0$. Remembering that in the weakly coupled regime, $\frac{\kappa}{2} >> g >> \gamma$, we note that Eq.(2.17) ends up with a square root of a negative expression. This can be interpreted as both eigenstates being at the same frequency ω due to having the same real part, but experiencing different damping. To understand this further, we observe that the damping can be represented as

$$\frac{\kappa}{2} \mp \sqrt{\frac{\kappa^2}{4} - |g|^2} \approx \frac{\kappa}{2}\left(1 \mp \left(1 - \frac{1}{2}\frac{4|g|^2}{\kappa^2}\right)\right) \approx \begin{cases} |g|^2/\kappa \\ \kappa \end{cases} \tag{2.18}$$

What Eq.(2.18) tells us is that in the weak coupling regime we observe two eigenstates, both at the same frequency ω; however, each experiences a different decay rate. The mode which experiences changes due to the cavity as seen by the presence of the

[5] Either into non-cavity modes, or non-emissive directions within the cavity mode

coupling parameter g is called the *cavity mode*. The other mode is uncoupled to the cavity, and is called the *vacuum mode*, as the emission is neither enhanced nor easily extractable. We observe the emitter damping to have a corresponding decay rate $\Gamma_{Cavity} = \frac{2|g|^2}{\kappa}$, and the vacuum decay $\Gamma_{Vacuum} = 2\kappa$. This is effectively the result of the emitter "seeing" the cavity and having its spontaneous emission rate increased by the cavity presence; this is called the Purcell effect, named after Edward Mills Purcell who first explained the effect in his 1946 seminal paper[33].

The Purcell enchancement of the emission rate can be represented as

$$F = \frac{\Gamma_{Cavity}}{\Gamma_n} = \frac{2|g|^2/\kappa}{n\Gamma_0} \tag{2.19}$$

We are interested in the maximum value of F. Refering to the expression for g in Eq.(2.13), we recognise the maxima in F happens when the emitter is spatially located at the cavity field maximum, and spectrally on resonance with the cavity. With some rearranging we obtain the maximum value of F, called the Purcell factor, to be

$$F_P = \frac{3}{4\pi^2}\left(\frac{\lambda}{n}\right)^3 \frac{Q}{V_{mode}} \tag{2.20}$$

Here, V_{Mode} expresses the spatial volume of the resonator cavity and shows that the more spatially confined around the source the cavity is, the stronger the Purcell enhancement is. The Q in the expression stands for the quality factor, or Q-factor, which is defined as the ratio of stored energy in the resonator to the energy dissipated per field oscillation period; essentially, how quickly the resonator energy leaves the system. Equivalently, the Q-factor can be defined spectrally as

$$Q \equiv \frac{\lambda}{\Delta\lambda} \tag{2.21}$$

where $\Delta\lambda$ is the resonance full with at half maximum. The dependence of F_P on the Q-factor suggests that the longer a field is confined around the source, the stronger the resulting emission enhancement.

2.2.2 Cavity Quantum Electrodynamics

Because only one of the decay channels experiences an increased decay rate, the Purcell effect results in dominance of the cavity mode. This, as well as providing an increased spotaneous emission rate into the cavity, also results in a preferred decay direction, depending on the geometry of the cavity and emitter system; a visual aid with some helpful symbols has been presented in Fig. 2.2.

The spontaneous emission into a vaccum mode with a decay rate Γ_{Vacuum} corre-

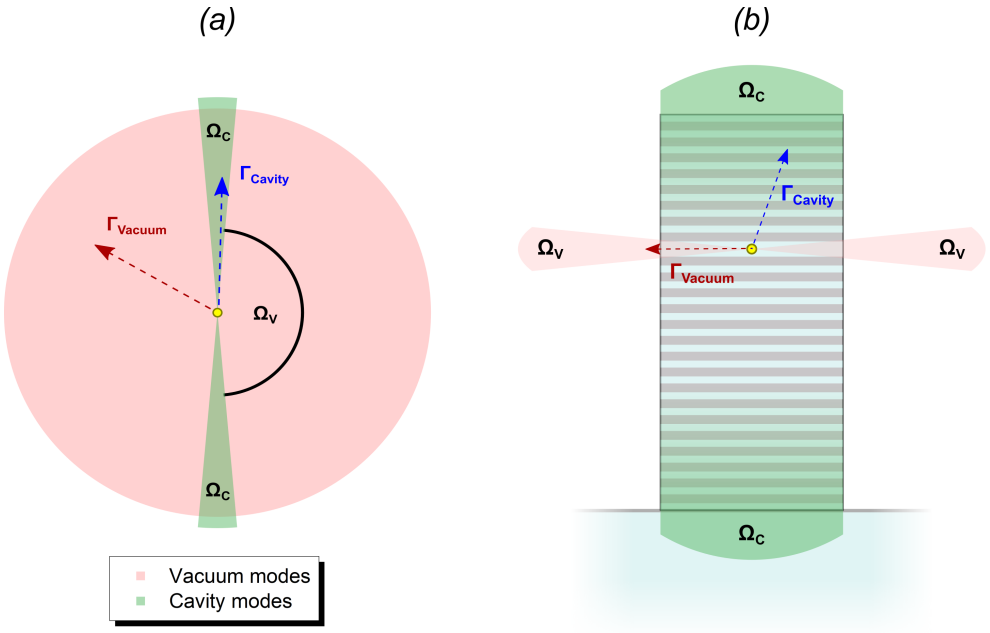

Figure 2.2: *The cavity and emission geometry of (a) an atomic single photon source; (b) an optical micropillar.*

sponds to emission within a solid angle Ω_V. Similarly, the Purcell-enhanced decay into the cavity mode occurs within a solid angle Ω_C, which an effect of the spatial confinement/distribution of the cavity mode [34]. The preferential decay into the vacuum mode therefore also results in a preferred direction of the emission and is a further reason[6] why quantum dots are coupled to optical resonators. This preference in emission is quantified by the *active coupling* to the cavity, also called the β-factor, which is defined as

$$\beta = \frac{\Gamma_{Cavity}}{\Gamma_{Cavity} + \Gamma_{Vacuum}} \tag{2.22}$$

It is important to note that while β correlates to the likelihood of decaying into the cavity mode, the ratio at which increased enhancement translates to increased active coupling to the cavity (essentially $\frac{dF_P}{d\beta}$) depends on the relative sizes of the cavity and vacuum solid angles, Ω_C and Ω_V respectively. The reason for this is subtle and lies in what the Q-factor represents, which is the total decay rate of the field regardless of direction. Therefore, increasing the Q-factor results in a decrease of the energy decay κ which affects both Γ_{Cavity} and Γ_{Vacuum} as seen in Eq.(2.18); however, these changes are not equal and the difference between $\Delta\Gamma_{Cavity}/\Delta\kappa$ and $\Delta\Gamma_{Vacuum}/\Delta\kappa$ depends on the relative size of Ω_C. This suggests that not all cavities have the same "Purcell factor to active coupling" efficiency and that for different values of Ω_C/Ω_V, the $\frac{dF_P}{d\beta}$ rate can vary.

[6]The other being the increased single photon generation rate, or emitter speed.

This also implies that models which may be applicable to one type of cavity might not be accurate to another one with a significantly different Ω_C/Ω_V ratio. Cavities based on atomic emitters, as shown in Fig. 2.2(a) have very small cavity solid angles, such that $\Omega_C \gg \Omega_V$. This leads to the estimation that $\Omega_V \approx 4\pi$, so the active coupling defined in Eq.(2.22) can be estimated as

$$\beta^* = \frac{F_P}{F_P + 1} \tag{2.23}$$

For clarity, in this thesis I use a * symbol to differentiate between the β-factor as calculated by Eq.(2.22) and the Purcell-factor based estimation provided by Eq.(2.23). This is because the accuracy of β^* relies on the assumption that $\Omega_V \approx 4\pi$, and as I show later in Chapter 6, this is not the case for micropillars cavities. This is because micropillars have significantly larger cavity solid angles Ω_C due to the lateral confinement provided by the radial interface of the high refractive index dielectrics and low refractive index air/vacuum. Unlike atoms, the vacuum solid angle cannot be approximated as 4π and as such, the β^* approximation is not an appropriate model of the active coupling parameter β.

What this suggests is that a larger Ω_C results in a lower F_P required to get the same β-factor, meaning that because micropillars have a large cavity solid angle (larger emission angle), less enhancement is required to achieve emission in the desired direction. One way to think about this is that the micropillar cavity is a "larger target" than an atomic one, and therefore it takes less "effort" to hit the target. This is of importance because unlike the expression for β^* (Eq.(2.23)) suggests, high β-factors can be achieved in miicropillars with low Purcell factors F_P, meaning that high brightness low-Q micropillars could potentially be plausible.

2.3 Optical Tamm states

2.3.1 Surface Plasmon Polaritons (SPPs)

To understand the differences between Tamm plasmons and other similar surface-bound states, we must first discuss a type of electromagnetic wave called surface plasmon polaritons (SPPs). We start by picturing a boundary between a semi-infinite conductor and dielectric. An incoming electromagnetic field could couple to the conductor's electron plasma (under certain conditions discussed below), resulting in an electromagnetic wave propagating along this interface, confined in the boundary plane such that the field decays evanescently into both dielectric and conductive materials (pictured below in Fig. 2.3(b)).

We begin by considering the wave equation

$$\boldsymbol{\nabla} \times \boldsymbol{\nabla} \times \vec{E} = -\mu_0 \frac{\partial^2 \vec{D}}{\partial t^2} \tag{2.24}$$

which can be rewritten, due to the lack of external field such that $\boldsymbol{\nabla} \cdot \mathbf{D} = 0$, in the form

$$\nabla \left(-\frac{1}{\varepsilon} \vec{E} \cdot \boldsymbol{\nabla} \varepsilon \right) - \nabla^2 \vec{E} = -\mu_0 \varepsilon_0 \varepsilon \frac{\partial^2 \vec{E}}{\partial t^2} \tag{2.25}$$

One trick that we can use is to solve this equation for each material of constant ε; what's more, we assume a harmonic solution[7] such that $\vec{E}(\vec{r}, t) = \vec{E}(\vec{r}) e^{-i\omega t}$. This has brought us to the Heimholtz equation for a wave propagating in vacuum with wave vector $k_0 = \omega c^{-1}$, which is

$$\nabla^2 \vec{E} + k_0^2 \varepsilon \vec{E} = 0 \tag{2.26}$$

It is convenient to the remainder of this thesis that we label the direction of propagation as the y axis; in other words, planar boundaries between media lie in the X-Z plane, and are perpendicular to the y axis. We can therefore apply Eq.(2.26) to the geometry of our system to get

$$\frac{\partial^2 \vec{E}(z)}{\partial z^2} + \left(k_0^2 \varepsilon - \beta^2 \right) \vec{E} = 0 \tag{2.27}$$

where the propagation constant is $\beta = k_y$.

It can be shown that for a wave which is harmonic in the time domain, provided that the media are homogenous in the x direction, only two sets of solutions emerge [35]. The first of these corresponds to a transverse electric (TE) mode, also known as an s-mode, such that the only component of E is E_x while H is made up of H_y and H_z; the second is a transverse magnetic (TM) mode, also known as a p-mode, where the only component of H is H_x, while E is composed of E_y, E_z. The wave equations for these modes are

$$\frac{\partial^2 E_x}{\partial z^2} + \left(k_0^2 \varepsilon - \beta^2 \right) E_x = 0 \qquad \text{(TE-wave)} \tag{2.28}$$

$$\frac{\partial^2 H_x}{\partial z^2} + \left(k_0^2 \varepsilon - \beta^2 \right) H_x = 0 \qquad \text{(TM-vave)} \tag{2.29}$$

We can then define $k_{eff} \equiv \sqrt{k_0^2 \varepsilon - \beta^2}$. To understand the propagation completely, we must also consider the propagation of the energy in the medium, given by the

[7] Harmonic in time, that is.

Poynting vector $\vec{S} = \vec{E} \times \vec{H}$. More accurately, we look at the time-averaged Poynting vector component in the direction of propagation (normal to the medium X-Z planar boundaries) given by the following expression[36]

$$\langle \vec{S} \rangle = \frac{1}{2} \left(\vec{E} \times \frac{k_{eff}}{2\omega} \vec{E}^* \right) = \frac{k_{eff}}{2\omega} \left| \vec{E} \right|^2 \tag{2.30}$$

These are:

- **Positive** ($\beta^2 < k_0^2 \varepsilon$): A real solution exists to the wave, resulting in a positive real part of Eq.(2.30);
- **Zero** ($\beta^2 = k_0^2 \varepsilon$): There is no propagation of the field in the medium. This case usually corresponds to total internal reflection at a boundary between two media, with no solutions corresponding to no transmission at the edge;
- **Negative** ($\beta^2 > k_0^2 \varepsilon$) : This results in an imaginary wavevector for the wave, resulting in an evanescent wave. It's important to note that $\mathrm{Re}(\langle \vec{S} \rangle) = 0$, implying no propagation of energy within the medium.

In this thesis we will be dealing with the case where β is high enough such that only evanescent solutions persist in the medium. If we imagine a boundary between two such media where the field decays in both directions normal to the boundary, then we have pictured an electromagnetic wave that can propagate only along the interface[8].

Surface plasmon polaritons are this type of a surface wave excitation arising at the boundary between a dielectric and a metal. We define a metal such that $\mathrm{Re}(\varepsilon_{metal}) < 1$, meaning that the dielectric function $\varepsilon_{metal}(\omega)$ has a non-zero imaginary part. The mode is therefore "bound" to the surface by the negative electric permittivity in the metal, and total internal reflection in the dielectric layer. Next, we examine the dispersion relation at this boundary in the case of TE and TM waves.

TE waves

Applying s-wave conditions to Eq.(2.27), we obtain that for a TE solution, we get the equations

$$E_z(y) = A_1 e^{i\beta x} e^{-k_1 y} \tag{2.31}$$

$$H_x(y) = -iA_1 \frac{1}{\omega \mu_0} k_1 e^{i\beta x} e^{-k_1 y} \tag{2.32}$$

$$H_y(y) = A_1 \frac{\beta}{\omega} \mu_0 e^{i\beta x} e^{-k_1 y} \tag{2.33}$$

[8]The Poynting vector components normal to the surface have no real part.

for the metal region, defined by $y > 0$, and

$$E_z(y) = A_2 e^{i\beta x} e^{k_2 y} \tag{2.34}$$

$$H_x(y) = iA_2 \frac{1}{\omega\mu_0} k_2 e^{i\beta x} e^{k_2 y} \tag{2.35}$$

$$H_y(y) = A_2 \frac{\beta}{\omega\mu_0} e^{i\beta x} e^{k_2 y} \tag{2.36}$$

for the dielectric corresponding to $y < 0$. Applying boundary continuity conditions on E_y and H_x results in the condition

$$A_2(k_1 + k_2) = 0 \tag{2.37}$$

It is important to note that in the coordinate system defined here, surface confinement requires the real parts of the wavevectors to be positive. Therefore, the only solution to this condition is given by $A_2 = 0 = A_1$. As such, we can conclude that conventional[9] SPPs cannot exist for TE polarization.

TM waves

We apply the same process for p-waves, arriving at the equations for the metal region,

$$H_z(y) = A_1 e^{i\beta x} e^{-k_1 y} \tag{2.38}$$

$$E_x(y) = iA_1 \frac{1}{\omega\varepsilon_0\varepsilon_1} k_1 e^{i\beta x} e^{-k_1 y} \tag{2.39}$$

$$E_y(y) = -A_1 \frac{\beta}{\omega\varepsilon_0\varepsilon_1} e^{i\beta x} e^{-k_1 y} \tag{2.40}$$

and the ones corresponding to the dielectric region are

$$H_z(y) = A_2 e^{i\beta x} e^{k_2 y} \tag{2.41}$$

$$E_x(y) = -iA_2 \frac{1}{\omega\varepsilon_0\varepsilon_2} k_2 e^{i\beta x} e^{k_2 y} \tag{2.42}$$

$$E_y(y) = -A_2 \frac{\beta}{\omega\varepsilon_0\varepsilon_2} e^{i\beta x} e^{k_2 y} \tag{2.43}$$

This time, we apply boundary continuity of H_z and $\epsilon_i E_y$ at the interface, which results in $A_1 = A_2$, implying

[9] It is discussed later in this text that Tamm plasmon surface states can in fact be excited with both TE and TM radiation.

$$\frac{k_1}{k_2} = -\frac{\varepsilon_1}{\varepsilon_2} \tag{2.44}$$

We then substitute the values of $k_{1,2}$ in this relationship by remembering that $k_i^2 = \beta^2 - k_0^2\varepsilon_i$ to get the SPP dispersion relation at the interface, given by

$$\beta = k_0\sqrt{\frac{\varepsilon_d\varepsilon_m}{\varepsilon_d + \varepsilon_m}} \tag{2.45}$$

where the dielectric permittivity is ε_d, and the metal one ε_m. It is the latter one which is of interest to us at the moment; to examine the dispersion relation closer, we can use the Drude dielectric function

$$\varepsilon_m(\omega) = 1 - \frac{\omega_p^2}{\omega^2 + i\gamma\omega} \tag{2.46}$$

Since we're interested in only $\mathrm{Re}(\beta)$, we get the real part of ε_m as

$$\mathrm{Re}\left(\varepsilon_m(\omega)\right) = 1 - \frac{\omega_p^2}{\omega^2} \tag{2.47}$$

The dispersion relation of a SPP for several situations has been shown in Fig. 2.3(a). It's important to observe that without the aid of coupling techniques, it is impossible for a propagating field to couple into the surface plasmon mode, since the dispersion curve of the SPP mode lies outside the light cone. While real solutions do exist for $\omega > \omega_p$, this is not the surface mode, but rather the region of transparency for the metal. This makes sense if we think of it in the following way: the SPP is a non-radiating mode, since $\mathrm{Re}(\langle\vec{S}\rangle) = 0$, and therefore it cannot be excited by a radiating mode; this includes by a propagating field since the propagating field has $\mathrm{Re}(\langle\vec{S}\rangle) \neq 0$. As such, the only mode that can be excited within the light cone are radiating modes at $\omega > \omega_p$, but these are not confined to the surface and as such are of no interest to us.

One way to do this is to match the momentum of the incoming p-wave to the one of the SPP with the use of a transmissive medium such that $\varepsilon_2 > \varepsilon_1$. The result is an increase in the wavenumber of the incoming light such that coupling can be achieved at the appropriate angle and frequency. This can be done in either the Otto configuration, where a prism is placed near a metal film such that the evanescent wave resulting from TIR can excite the SPP, or the much more common Kretschmann configuration, where the metal film is deposited on the prism such that the SPP forms on the outer edge of the metal [37], which has been illustrated in Fig. 2.3(c). Another possible method is to use a diffraction grating to increase the momentum of incident light in order to couple to the higher momentum SPPs [38]; however, examining any of these past the point of mention is out of the scope of this thesis.

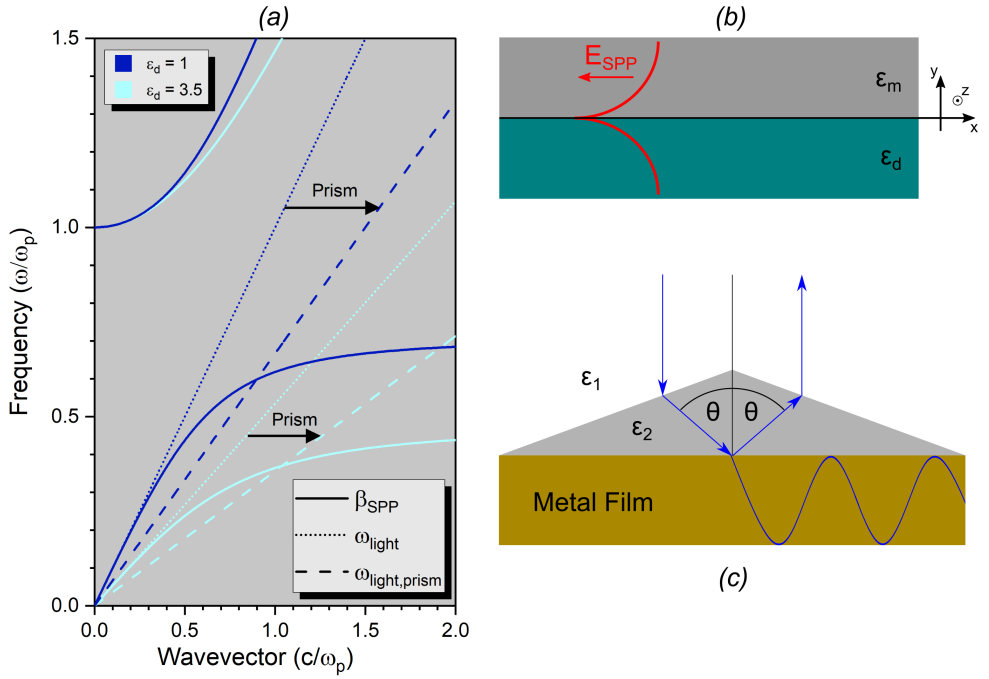

Figure 2.3: *(a) The dispersion of a surface plasmon polariton between a Drude metal with negligible collision frequency and a material with $\varepsilon_d = 1$ (navy blue), or $\varepsilon_d = 3.5$ (cyan). The light lines are presented as well, showing the impossibility of exciting SPP modes without the use of a coupling mechanism, such as the Kretschmann configuration in this figure; (b) The propagation of a SPP, with evanescent decay in each direction normal to the surface; (c) An illustration of the Kretschmann configuration, where a metal film is deposited on a dielectric prism. The incoming wave is refracted in the prism due to $\varepsilon_2 > \varepsilon_1$, giving it momentum in the surface plane. The evanescent component of the TIR wave is coupled to the SPP, shown as a sinusoid in the metal film.*

2.3.2 Bloch Surface Waves (BSWs)

Before I discuss Tamm plasmons, we must first understand why how the properties of TPs differ from the properties of SPPs established in the previous section. To do so, we must talk about Bloch waves in periodic layered media and why the stop band of 1-dimensional photonic crystals is of importance to us.

We begin by considering a one dimensional periodic medium made up of 2 alternating dielectric layers. Defining d_1 and d_2 as the thicknesses of each dielectric such that the period is given by $L = d_1 + d_2$, we can describe the refractive index of the structure as

$$n(y) = \begin{cases} n_1 & \text{for } 0 < y < d_1 \\ n_2 & \text{for } d_1 < y < L \end{cases} \tag{2.48}$$

with a periodicity of the structure described by

$$n(y + L) = n(y) \tag{2.49}$$

where n_1 and n_2 are the refractive indices of each layer. A visual representation of the structure can be seen in Fig. 2.4.

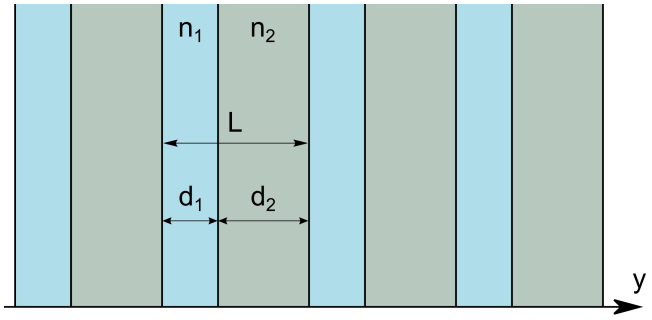

Figure 2.4: *A periodic layered structure formed by alternating layers of thickness d_1 and d_2, infinite in the y direction. The period of the structure is labeled as L.*

The motion of electrons in crystal solids can be used to model the propagation of electromagnetic waves in such layered media; in fact, the Kronig-Penney formulation used is mathematically identical to the one applicable to our case [39]. We can therefore describe $E(y, z)$ by applying the Floquet theorem, leaving us with wave equation solutions

$$E_K(y, z) = E_K(y)e^{-i\beta z}e^{-iKy} \tag{2.50}$$

where the periodicity of E mirrors that of n such that

$$E_K(y + L) = E_K(y) \tag{2.51}$$

The Bloch waves resulting in the media depend on the Bloch wave number K. Considering the E field within each layer to be a sum of incident and reflected plane waves, the transfer matrix method described in Chapter 3 can be used to determine K and $E_K(y)$[36]. In the context of this thesis, we are interested primarily in the dispersion relation for the Bloch wavefunction, given by

$$\cos(L \times K(\beta, \omega)) = \frac{T_{11} + T_{22}}{2} \tag{2.52}$$

where T_{11} and T_{22} correspond to elements in the transfer matrix of the system. For transverse electric waves, these are given by

$$T_{11} = e^{ik_1 d_1}\left(\cos(k_2 d_2) + \frac{i}{2}\left(\frac{k_2}{k_1} + \frac{k_1}{k_2}\right)\sin(k_2 d_2)\right) \tag{2.53}$$

$$T_{22} = e^{-ik_1 d_1}\left(\cos(k_2 d_2) - \frac{i}{2}\left(\frac{k_2}{k_1} + \frac{k_1}{k_2}\right)\sin(k_2 d_2)\right) \tag{2.54}$$

whereas for transverse magnetic waves, they are of the slightly different form

$$T_{11} = e^{ik_1 d_1}\left(\cos(k_2 d_2) + \frac{i}{2}\left(\frac{n_1^2 k_2}{n_2^2 k_1} + \frac{n_2^2 k_1}{n_1^2 k_2}\right)\sin(k_2 d_2)\right) \tag{2.55}$$

$$T_{22} = e^{-ik_1 d_1}\left(\cos(k_2 d_2) - \frac{i}{2}\left(\frac{n_1^2 k_2}{n_2^2 k_1} + \frac{n_2^2 k_1}{n_1^2 k_2}\right)\sin(k_2 d_2)\right) \tag{2.56}$$

The component of the wave vector in the z-direction is given by β, such that the k_y component (labeled for simplicity as k) is given by

$$k_i - \sqrt{\left(\frac{n_i \omega}{c}\right)^2 - \beta^2} \tag{2.57}$$

where $i = 1, 2$. Using these expressions, we can work out the dispersion relation for TE and TM waves for a periodic structure similar to the one used in this thesis; therefore, the dispersion relation for a GaAs ($n_1 \approx 3.4$) and AlAs ($n_2 \approx 2.9$) of respective thicknesses $d_1 = 95$ nm and $d_2 = 110$ nm has been presented in Fig. 2.5. It can be noted in Fig. 2.5(b) that the forbidden bands disappear at $\beta = \frac{\omega}{c} n_1 \sin(\theta_B)$, where θ_B is the Brewster angle at which the incident and reflected waves are uncoupled.

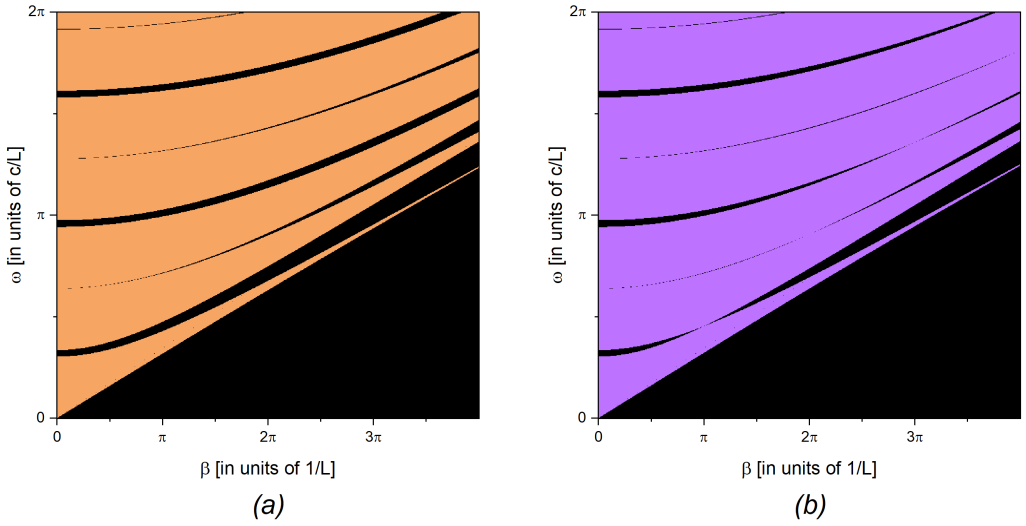

Figure 2.5: *The dispersion relation for (a) TE, and (b) TM waves for a GaAs/AlAs periodic structure. The black regions corresponding to $|T_{11} + T_{22}| > 2$ result in disallowed bands with evanescent solutions for E, while the coloured regions correspond to $|T_{11} + T_{22}| < 2$ result in real solutions.*

It is the existence of the forbidden bands which is the property of most interest to us. An incident plane wave within the forbidden band generates a Bloch wave in the medium; as such, the wave cannot propagate in the dielectric structure as the Poynting vector component normal to the surfaces is 0. This means that a high reflectivity value is expected for waves within the forbidden bands. It can be shown [36] that the reflectivity of a structure with N pairs is

$$|r_n|^2 = \frac{|R_1|^2}{|R_1|^2 + \left(\frac{\sinh K_i L}{\sinh N K_i L}\right)^2} \tag{2.58}$$

where KL is a complex number, in that

$$KL = m\pi + iK_iL \tag{2.59}$$

We see that for large N, $R \to 1$, which makes this type of one dimensional photonic crystal, called a distributed Bragg reflector (DBR), a tunable reflective element without limits on material properties. The use of DBRs as lossless waveguides in photonic structures is particularly popular due to the tunability of the band gap, determined by the choice of each layer thickness and refractive index (material). It can be shown that the band gap properties (for normal incidence, for simplicity) are determined by

$$\lambda_{gap} = 2n_{average}L \tag{2.60}$$

$$\Delta\lambda_{gap} = \frac{4}{\pi}\sin^{-1}\left(\frac{n_2 - n_1}{n_2 + n_1}\right) \tag{2.61}$$

where λ_{gap} is the centre wavelength, and $\Delta\lambda_{gap}$ the bandwidth of the "stop band". For GaAs and AlAs, the reflectivity at normal incidence as a function of wavelength has been presented in Fig. 2.6 for various structures with different numbers of DBR pairs.

Semi-infinite DBR

The Bloch waves in this structure have imaginary wavevectors, cannot propagate, and are evanescent. Up until this point, we have considered the periodic lattice to be infinite along the y axis; we must now consider the case where the DBR is terminated by a boundary. We therefore assume that the structure is terminated by a dielectric layer such that the refractive index structure can be described by

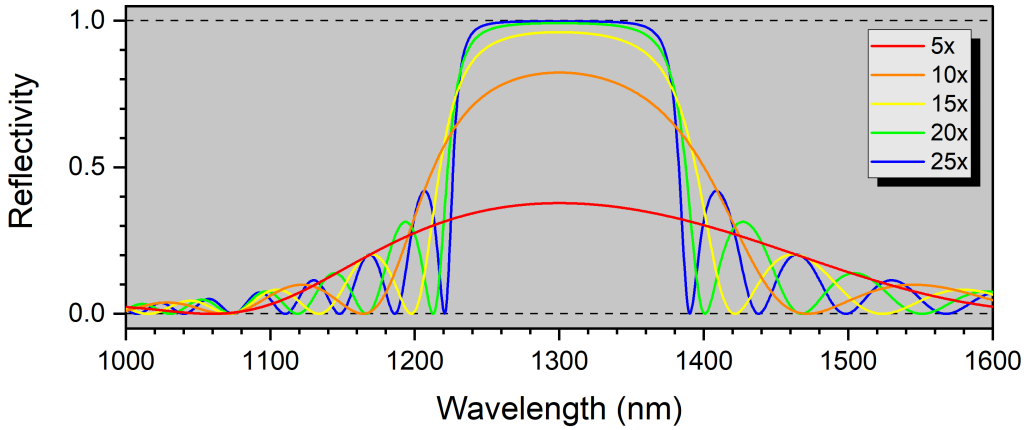

Figure 2.6: *The reflectivity of the GaAs/AlAs distributed Bragg reflector used in the design of the optical cavities examined in this thesis. Each colour represents a different amount of DBR pairs, with the total number of layers is double the number in the figure legend. This has been calculated with the Transfer Matrix Method (TMM) discussed in Chapter 3.*

$$n(y) = \begin{cases} n_0 & y \leq 0 \\ n_1 & 0 < 0 \leq d_1 \\ n_2 & d_1 < y \leq L \end{cases} \tag{2.62}$$

with a periodicity described by

$$n(y + L) = n(y) \tag{2.63}$$

for $y \geq 0$. This can be seen in Fig. 2.7.

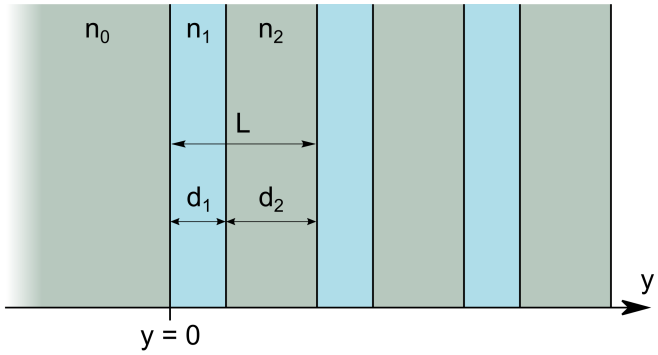

Figure 2.7: *A representation of the termination of the (previously) infinite DBR with a dielectric of refractive index n_0 (as opposed to the n_1 and n_2 that form the periodic part of the structure).*

The previous assumption that the DBR is infinite meant that waves with complex K are not allowed due to the boundary condition that the wave must decay fully as $|y| \to \infty$. The existence of a dielectric boundary to the semi-infinite DBR removes this

requirement, allowing K to take complex values. This results in exponentially damped solutions which now can exist within the forbidden energy bands [40].

We know the E field in the DBR part of the structure can be described as a Bloch wave, and solving the wave equation Eq.(2.27) gives the E field in the structure,

$$E(y) = \begin{cases} Ae^{-iky} + Be^{iky} & \text{for } y \leq 0 \\ E_K(y)e^{iKy} & \text{for } y \geq 0 \end{cases} \tag{2.64}$$

where $k = \sqrt{\left(n_0 \frac{\omega}{c}\right)^2 - \beta^2}$.

In discussing boundary conditions, we observe that the Bloch wave dispersion relation in Eq.(2.52) originates from the Bloch wave eigenvalue function [40]

$$T\vec{E} = e^{-iKL}\vec{E} \tag{2.65}$$

where T is the transfer matrix of the DBR. It can be shown [36] that the eigenvector and eigenvalues that satisfy this equation are

$$\vec{u}_0 = \begin{pmatrix} v_0 \\ w_0 \end{pmatrix} E_K(y) = \begin{pmatrix} T_{12} \\ e^{-iKL} - T_{11} \end{pmatrix} \tag{2.66}$$

The reason we must consider this is that while applying the boundary condition that a surface state must be a decaying solution results in $B = 0$, applying the continuity equations on the tangential components of E and H leaves us with a set of equations

$$A = v_0 + w_0 \tag{2.67}$$

$$-ikA = -ik_1(v_0 + w_0) \tag{2.68}$$

The dispersion relation can therefore be shown to be

$$k = -k_1 \frac{e^{-iKL} - T_{11} - T_{12}}{e^{-iKL} - T_{11} + T_{12}} \tag{2.69}$$

This is a description of Bloch surface waves [41]. The BSW modes are non-radiating, meaning that they transmit no power normal to the surface of the interface; the necessity of matching with an explonentially decaying Bloch envelope means that the wave within the terminating (n_0) medium must also be evanescent. Strong parallelism exists between BSWs and localised electronic surface states at crystaline solid boundaries, with the first optical version proposed in the 60s by Kossel [42], and experimental confirmation in DBRs in the late 70s [43].

Similarly to SPPs, BSWs are confined to the interface between the dielectric and the DBR because the tangential wavevector is greater than the light line, resulting in no coupling to propagating modes. As such, BSW excitation requires coupling techniques. An important distinction exists between SPPs and BSWs, in that SPPs can only be exctied with TM waves, whereas BSWs can arise with either TE or TM polarised light. To understand why this is, we remember the boundary conditions on the tangential magnetic and electric fields such that

$$H_z = H'_z \tag{2.70}$$

$$E_x = \frac{1}{\varepsilon}\frac{\partial H_z}{\partial y} = \frac{1}{\varepsilon`}\frac{\partial H'_z}{\partial y} \tag{2.71}$$

This forces a change in the electric permittivity in order to satisfy the derivative swap change imposed by the BCs for TM waves, whereas a change in magnetic permeability is needed for TE waves. However, it can be shown that for an oscillating solution within a decaying envelope, BSWs can have a positive derivative within each DBR pair while still experiencing exponential decay within the overall structure [44]. As such, under certain conditions the BCs sign change can be met without the need for a sign change in either permittivity or permeability. Effectively, the DBR structure can fulfil the role of a negative permittivity (NP) or negative magnetic permeability (NMP) material [45] such that both TE and TM polarisations of BSW can be excited, without the actual use of any materials other than dielectrics where $\varepsilon_i, \mu_i > 0$.

When the first layer in the lattice (the n_1 layer sharing a boundary with the n_0 one) is no longer the same size as the other periodic layers, but has a thickness $d'_1 < d_1$, the field is changed such that the BSW wavelength changes. The most reliable method to determine the eigenfrequencies is impedance matching. Impedance is defined as the ratio of the tangential components of the E and H field such that $\zeta = \frac{E_t}{H_t}$, with the surface states bound by the condition [46][47]

$$\zeta_L + \zeta_R = 0 \tag{2.72}$$

where L and R label regions left and right of the y=0 boundary between the terminating layer and the DBR. This is a particularly helpful technique as it allows us to match two separate impedances rather than have to work out and match the fields themselves.

It should be noted that Bloch waves have a changing impedance, periodically cycling between $\pm i\infty$ with zeros/infinities occuring at extrema of the E and H fields within the

Bloch wave amplitude (as opposed to envelope)[44]. The impedance in the DBR of waves at TIR must be purely imaginary as the material is of a positive ε and μ. It can therefore be concluded that there must be some wavelength within the stop band where the impedances will match and produce a Bloch surface wave. The impedance of the semi-infinite DBR can be varied by changing the d_1' parameter, effectively allowing for a precise choice of BSW frequency within the stop band.

The appearance and photonic properties of Bloch surface waves between a non-infinite terminating layer and a Bragg reflector, including the impedance matching method, are of interest to us; particularly we want to consider the plasmonic effects of introducing a metallic surface to terminate the DBR, as has been done in the following section.

2.3.3 Confined Tamm Plasmons (CTPs)

We have shown that while surface plasmon polaritons are bound by TIR within the metal-dielectric boundary, they require coupling devices such as gratings or the introduction of dielectric prisms to match the momentum of the incident waves to the SPP mode and can only be excited by TM waves. Periodically layered media terminated by a dielectric results in Bloch surface waves which can be excited by both TE and TM waves, but still require coupling devices due to having dispersion curves outside the light cone. In this section, I build on the existing discussion to address one of the core concept in this thesis, which is the existence of optical Tamm states, called Tamm Plasmons, at the boundary between a metal and a DBR.

These states are analogous to electronic states within crystals forbidden bands, provided that the crystal is terminated by a boundary, first proposed by Igor Tamm in 1933 [48]. The same method has been used to propose the existence of optical states in the stop band at the surface of photonic crystals. Analogously to the electronic Tamm States, a nomenclature of "Tamm plasmon-polaritons" has been proposed [4], with the shorter Tamm plasmons (TPs) also used.

In this text, I will use "Tamm plasmons[10]" as nomenclature when discussing the optical surface states excited between a metal and a DBR. These states, much like SPPs, excite the metal below the plasma frequency, meaning that the modes are non propagating in directions normal to the metal surface. Furthermore, confinement in the metal arises due to the negative permittivity, resulting in evanescent solutions with no Poynting vector component normal to the surface. The crucial difference comes in the confinement in the dielectric layer; while the wave is confined to the metal-dielectric

[10]The term "Tamm modes" might appear with the same meaning.

surface due to TIR in SPPs, Tamm plasmons are confined due to the photonic stop band of the DBR. As deliberated further below, this means that no additional coupling methods are needed to excite the mode as the dispersion curve lies within the light cone [4](See Fig. 2.8(c) [49]). Furthermore, Tamm plasmons can be TM or TE polarised, as they can be excited by the TE or TM polarised Bloch surface waves.

To explain the properties of Tamm plasmons, we follow the process outlined in [4] by considering a 1-dimensional structure along the y axis where a metallic layer of thickness d_m and complex refractive index n_m is deposited on a DBR such that the higher refractive index dielectric forms the metal-dielectric boundary; this layer is of importance because it plays a role in determining the eigenfrequencies of the BSW as discussed in the previous section. From this point on I will refer to this as the spacer layer, to agree with labeling used in preceeding research on Tamm plasmons[50]. A diagram of such a dielectric DBR-metal structure, reffered to as "Tamm plasmon structures"[11] for convenience, has been shown in Fig. 2.8(d); not pictured in the figure is the n_1 substrate on which the DBR is built.

The layers in the DBR have been chosen such that $d_i = \frac{\lambda_B}{4n_i}$ where $i = 1, 2$, and λ_B is the centre of the photonic stop band, the Bragg wavelength. The eigenfrequencies of the system are obtained with the impedance matching method, which can be re-written in the case for a boundary between a DBR an an NM (or NMP) material, imagined as another DBR, as

$$r_L r_R = 1 \tag{2.73}$$

where r_L,r_R are the reflectivities of each DBR. This is worked out from Eq.(2.72) as

$$\zeta_L = \frac{1 + r_L}{1 - r_L}\sqrt{\frac{\varepsilon_0}{\mu_0}} \tag{2.74}$$

$$\zeta_R = \frac{1 + r_R}{1 - r_R}\sqrt{\frac{\varepsilon_0}{\mu_0}} \tag{2.75}$$

Applying this to the TP structure, we get the Tamm plasmon condition

$$r_m r_{DBR} = 1 \tag{2.76}$$

Where r_{DBR} has been labeled as "DBR" for convenience, but in reality means the reflection coefficient of the photonic crystal made up of the spacer layer and the DBR

[11] Meaning structures, like the one described here, which support Tamm plasmon excitation

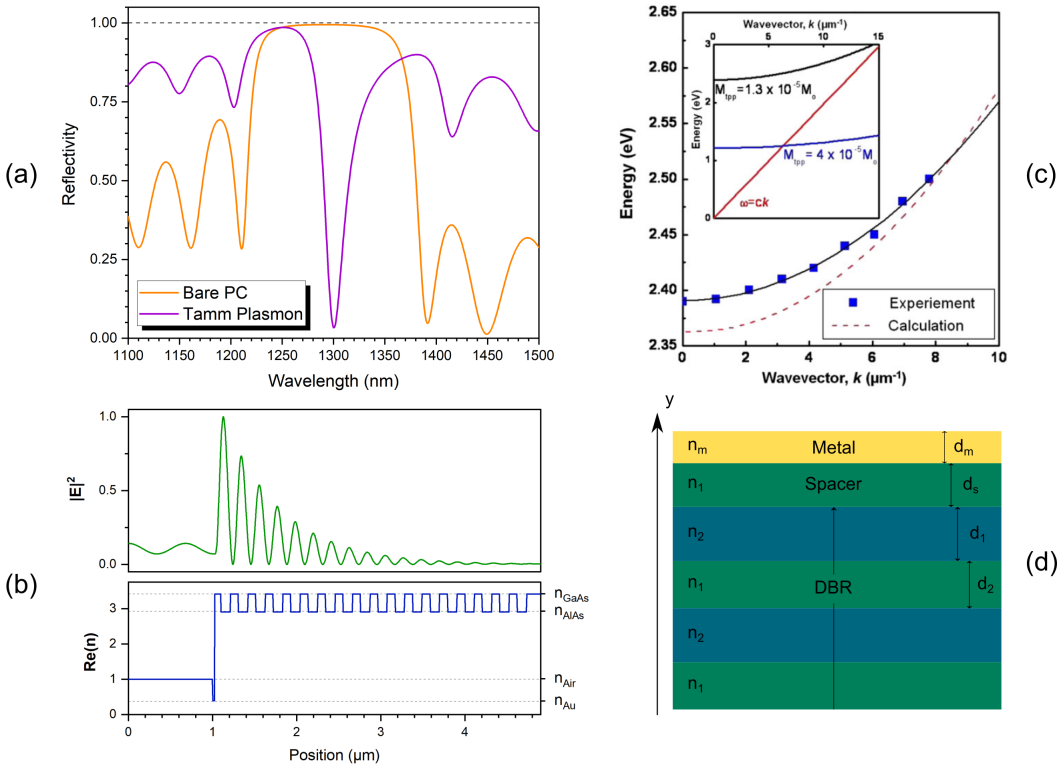

Figure 2.8: *(a) The reflectivity for a bare photonic crystal (without metal deposited on the spacer), and one for the Tamm mode (with metal deposited). Calculated using the transfer matrix method for a structure of 19.5x pairs GaAs/AlAs DBR, $d_s = 65nm$, and $d_m = 16nm$. It can be seen that the incident wave is reflected strongly for frequencies within the stop band without the metal layer, and couples into the optical Tamm state where the reflectivity dips to near 0; (b) The refractive index structure and E,H fields within the Tamm structure (n.b. semi-infinite metallic layer) reveal the oscillating Bloch wave within a larger decay envelope, obtained with the transfer matrix method. The source is positioned at the largest peak in E, at the boundary between the GaAs spacer layer and the first AlAs layer of the DBR, near the 1.1 μm mark ; (c) Figure from [49] - Measured and calculated dispersion relations for Tamm modes excited at the interface between Ag and ZnO/Al_2O_3 DBR. The parabolic dispersion curve with real solutions within the light cone below the metal plasma frequency are why Tamm plasmons require no additional coupling elements; (d) An illustration of a one dimensional Tamm plasmon structure. The layers, along with their refractive indices and respective depths, have been labeled.*

underneath. The eigenfrequency can then be controlled by varying the reflection coefficients of the metal and spacer, as long as this results in a frequency within the DBR stop band - this is important as the negative permittivity emulated by the stopband is needed.

The metal reflection coefficient can be estimated using the Drude model, which assumes classically kinetic behaviour of electrons within the metal, with electrons bouncing from the larger ions in series of collisions. Assuming a small collision rate and $\omega^2 << \omega_p^2$, we can estimate the refractive index of metal such that

$$r_m \approx -e^{\frac{2in_1\omega}{\omega_p}} \tag{2.77}$$

While the Drude model fails to account for long range interactions between charged particles, and makes a classical ideal gas assumption for the movement of free electrons, it's accurate enough to be used to show that for a sufficient number of DBR pairs, we can use the transfer matrix method to obtain values of r_{DBR} [36] depending on whether $n_1 > n_2$ or not; these values are

$$r_{n_1>n_2} = -\exp\left(i\pi\left(\frac{n_1}{n_1-n_2}\frac{\omega-\omega_0}{\omega}\right)\right) \tag{2.78}$$

$$r_{n_1<n_2} = \exp\left(i\pi\left(\frac{n_2}{n_2-n_1}\frac{\omega-\omega_0}{\omega}\right)\right) \tag{2.79}$$

Comparing these, it can be seen that r_m has a negative sign, corresponding with a negative phase change. In order to match this on the other side of the boundary, r_{DBM} must also cause a negative phase change, which is why the metal-spacer interface must be formed by the dielectric with the higher refractive index (of the two dielectrics that form the DBR). Conversely, for excitation above the metal plasma frequency, i.e. the transparency regime, it is necessary for $n_2 > n_1$, as r_m takes on a positive sign, corresponding to a phase shift of 0 for reflected waves.

The condition laid out in Eq.(2.76) is central to this thesis; it can be seen that variations in either metal or spacer layer can be used to change the eigenfrequency of the TP mode [51][49]. Changes in d_s[12] have a larger effect on r_{DBR} than changes in d_m have on r_m; nevertheless, as two parameters play a role in λ_{TP} (which represents the central wavelength of the Tamm plasmon mode), there are many different combinations of d_s and d_m which will result in the same λ_{TP}. This is of importance and is further explained in Chapter 4.

Confined Tamm Plasmons (CTPs)

To translate this into a three-dimensional model, we must introduce confinement along the surface boundaries. In reality, the materials will not be infinite in the x,z directions, which is particularly of interest for the metal layer, where changing the geometry from a semi-infinite planar layer to one that terminates laterally; this is usually in the form of a disc of some radius r_m such that a cylindrical symmetry in the physical makeup of the Tamm structure exist around a central axis, which has been labeled as the y axis in this thesis.

[12]The labelling convenience in this thesis is that d_s represents the spacer layer thickness, while d_m is the metal layer thickness.

The introduction of a radial boundary within the metal layer creates confinement of the Tamm mode due to the inability for the mode to couple onto the non-metalic boundary between the spacer layer; Bloch surface waves on the non-metallic boundary require coupling methods and as such cannot be excited. Therefore, the Tamm mode can propagate only along the circular metal-spacer boundary, i.e. is confined. As such, these modes are called confined Tamm plasmons (CTPs). A note on nomenclature: in this text, I use the term Tamm plasmon (TP) to discuss the 1-D semi-infinite case, whereas the term confined Tamm plasmon (CTP) is used to denote the Tamm mode in a laterally confined metal layer. It is important to make this distinction because as can be seen in Fig. 2.9(a)(c), significant changes to the eigenmodes of the Tamm mode are observed when the disc diameter is below 2.5 μm.

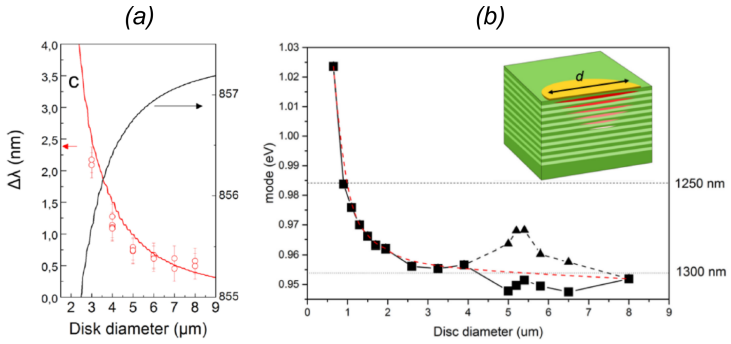

Figure 2.9: *(a) Recreated from [52] - Spectral detuning between the first and fundamental modes as a function of disc diameter, where open circles are experimental data and lines are calculations. The black line corresponds to the right axis, labelling the calculated spectral position of the CTP mode. (b) Figure from [50] - The fundamental CTP modes as a function of diameter for a $d_{Au} = 25nm$,$d_s = 75nm$. Overlapping with higher-order modes, particularly between 5 and 7 μm, result in more than one possible mode to be identified. Therefore, square and triangle symbols show the two lowest-energy modes identified for disc diameters between 5 and 7 μm. The dashed red line is an exponential fit to only the data points outside these diameters. A diagram of the laterally confined E-field has been inserted as well.*

In this thesis the effects of changing the diameter (and therefore confinement) are not of relevance; The exact parameters of the CTP structures examined, including the disc diameter, are based on previous research on GaAs/AlAs CTP structures at O band telecomms wavelengths and have been elaborated further on in Chapter 3.

Changes in temperature would affect the emitter by slightly changing the size of the components (notably the DBR layers), as well as the refractive index of materials. For the purpose of this thesis, the temperature has been assumed to be room temperature (300 K), as the exact refractive index or thickness values are not what's examined, but rather how their change affects the device performance.

Methods

3.1 Overview

Computer modelling is an extremely useful tool for researching the behaviour of EM waves through various photonic structures. Research involving the investigation of changes in EM behaviour over some structural parameter particularly relies on numerical modelling techniques to save a considerable amount of material and human resources in physical sample fabrication and subsequent experiments. Simulations are particularly necessary if certain structural parameters are unknown and/or difficult to analytically model, possibly rendering sample fabrication impossible.

For the purposes of this thesis, two methods are used to model the behaviour of EM waves: a one dimensional approximation of the Fresnel coefficients of the system using the transfer matrix method (TMM), and a three-dimensional solution of Maxwell's equations through the volume of the structure for a given time and frequency domain using the finite-difference time-domain (FDTD) method.

This chapter begins with a derivation of the fundamentals of the transfer matrix method. After an initial formulation for a single dielectric layer between two semi-infinite media for both transverse electric (s-) and transverse magnetic (p-) waves, the method is expanded for a general case of N layers, each of varying thickness and refractive index.

My explanation of the FDTD method starts with a brief discussion of the origins of the FDTD method, as well as some of its strengths and weaknesses as an accurate numerical analysis technique. This is followed by a presentation on the main principles behind the central finite difference approximation, as well as the space- and time-staggered cells first proposed by Kane Yee in 1966 [53]. I have made an argument that the simulations in this thesis have been appropriately set up to accurately reflect real EM waves (within reasonable error) by explaining some of the additional techniques in the commercial FDTD suite used; this includes a discussion on the dipole source,

advanced meshing and gridding techniques, the use of perfectly matched layers (PMLs), as well as symetrical boundary conditions.

The chapter ends with a brief explanation of the way data is gathered from the computational domain by either power monitors or time monitors, and on the calculations of the quality factor of the cavity mode.

3.2 Transfer Matrix Method (TMM)

F The calculation of reflection and transmission coefficients of structures containing layered media using matrices first emerged in the decades following World War II [54]. While the calculation of the Fresnel transmission and reflection coefficients without matrix formulation is possible, it is unadvisable as the algebraic expressions involved become significantly more complicated with each additional material introduced [36]. As computers are efficient at multiplying matrices [55], TMM resolves the issue of long algebraic expressions to a computationally low-cost probe into the R,T values of a stack of various materials by formulating the changes in the propagating wave at each interface and through each layer as 2x2 matrices such that the Fresnel coefficients can be calculated as a product of 2x2 matrices; however, it can only be applied to 1-dimensional esimations, limiting it's ability to accurately model the behaviour of real electromagnetic fields.

To understand how the transfer matrix method works, we begin by considering a single layer placed within two semi-infinite media on each side, such that each medium is isotropic and homogenous (Fig. 3.1). If the thickness of the middle layer is said to be d, then the refractive index can be expressed as

$$n(y) = \begin{cases} n_1 & \text{if } y < 0 \\ n_2 & \text{if } 0 < y < d \\ n_3 & \text{if } d < y \end{cases} \tag{3.1}$$

such that n_1, n_2, n_3 correspond to each dielectric refractive index. Assuming that the electromagnetic wave propagates along the xy plane, the electric field satisfying Maxwell's equations is

$$E = E(y)e^{i(\omega t - \beta x)} \tag{3.2}$$

This is because the whole medium is homogenous in the x direction, and therefore $\delta n/\delta x = 0$. As such, the electric field is a TE wave when $\mathbf{E} \,||\, x$, or a TM wave if $\mathbf{H} \,||\, x$.

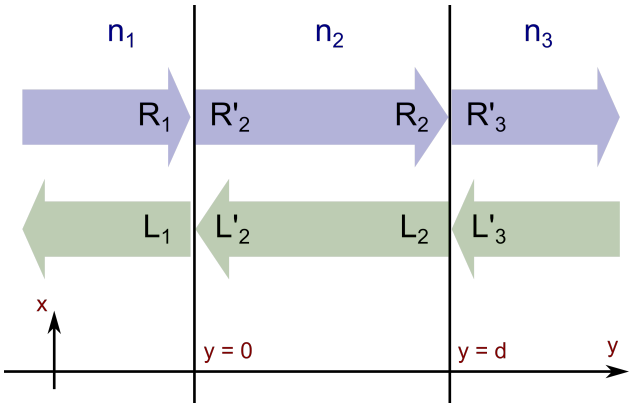

Figure 3.1: *A diagram of the dielectric structure and propagating electric fields in a dielectric layer.*

The electric field $E(y)$ can further be expressed as a superposition of right- and left- travelling components (represented by the blue and green arrows in Fig. 3.1, respectively) as

$$E(y) \;=\; C_r e^{-ik_y y} + C_l e^{-ik_y y} \;\equiv\; R(y) + L(y) \tag{3.3}$$

such that the constrains C_r and C_l correspond to each homogenous layer, and the y components of the wave vector are given by $\pm\, k_y$. This can be written as a column vector in the form

$$\mathbf{E} = \begin{pmatrix} R \\ L \end{pmatrix} \tag{3.4}$$

We can further define

$$\begin{array}{cccccccc} R_1 & = & R(0^-) & R_2' & = & R(0^+) & R_2 & = & R(d^-) & R_3' & = & R(d^+) \\ L_1 & = & L(0^-) & L_2' & = & L(0^+) & L_2 & = & L(d^-) & L_3' & = & L(d^+) \end{array} \tag{3.5}$$

where the left side of the boundary at y = 0 is labeled as 0^-, and the right side as 0^+. The definition of d^- and d^+ is analogous for the interface at y = d.

There are changes in the E field as the wave propagates through the middle layer, and at each interface. First, we consider the E field in the middle layer, where a phase change ϕ will be applied to each component of $E(y)$ such that

$$\begin{aligned} R_2' &= e^{i\phi} R_2 \\ L_2' &= e^{-i\phi} L_2 \end{aligned} \tag{3.6}$$

where the phase has the same magnitude $\phi = k_{2y} d$ for each wave, but opposite sign due to the opposite wavevectors. This can be expressed in column vector and matrix

form as

$$\begin{pmatrix} R_2' \\ L_2' \end{pmatrix} = P_2 \begin{pmatrix} R_2 \\ L_2 \end{pmatrix} = \begin{pmatrix} e^{i\phi} & 0 \\ 0 & e^{-i\phi} \end{pmatrix} \begin{pmatrix} R_2 \\ L_2 \end{pmatrix} \tag{3.7}$$

where P_2 is the *propagation matrix*.

To work out the relationship between R_1, L_1 and R_2', L_2' (and a similar relationship for the other boundary), we have to consider the reflection and trasnmission of TE and TM polarised waves at a dielectric boundary. Some relevant labels and definitions can be found in Fig. 3.2. Each coloured region represents a dielectric with permittivity ϵ_j and μ_j where $j = 1, 2$. A plane wave (wave vector $\mathbf{k_1}$) of frequency ω gets either transmitted (wave vector $\mathbf{k_2}$) or reflected ($\mathbf{k_1'}$).

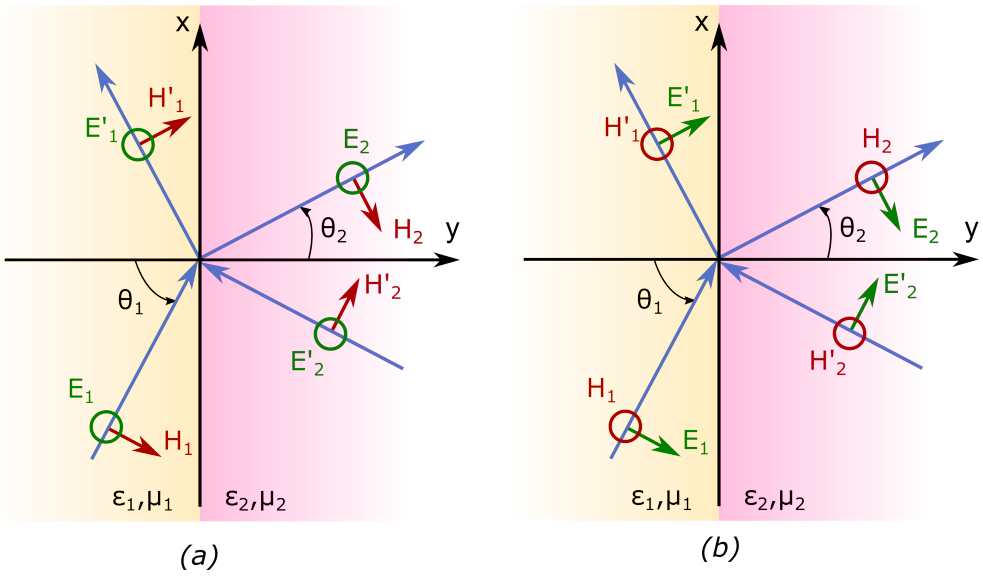

Figure 3.2: *The reflection and refraction of a TE (a) and TM (b) wave. The wave propagation is shown in blue, with the* ***E*** *and* ***H*** *fields in green and red respectively. The dielectric boundary lies on y=0.*

To obtain the boundary conditions, we construct a thin cylinder such that its flat sides are parallel to the dielectric boundary and said boundary bisects the cylinder. We then apply the Gauss divergence theorem

$$\int \boldsymbol{\nabla} \cdot \mathbf{F} \, dV = \int \mathbf{F} \cdot d\mathbf{S} \tag{3.8}$$

to both sides of Maxwell's equations

$$\boldsymbol{\nabla} \cdot \mathbf{D} = \sigma \tag{3.9}$$

$$\boldsymbol{\nabla} \cdot \mathbf{B} = 0 \tag{3.10}$$

To simplify, we take the limit where the height of the cylinder reaches zero such that the surface integral reduces to an integral over the flat faces of the cylinder. Therefore,

$$\mathbf{n} \cdot (\mathbf{B_2} - \mathbf{B_1}) = 0 \tag{3.11}$$

$$\mathbf{n} \cdot (\mathbf{D_2} - \mathbf{D_1}) = \sigma \tag{3.12}$$

This can be rewritten into the more convenient boundary condition form

$$B_{2n} = B_{1n} \qquad\qquad D_{2n} - D_{1n} = \sigma \tag{3.13}$$

such that $X_{jn} = \mathbf{n} \cdot \mathbf{X_j}$, where $j = 1, 2$ and X represents B or D. The general solutions of the standard electromagnetic wave equations

$$\boldsymbol{\nabla}^2 \mathbf{E} - \mu\varepsilon \frac{\partial^2 \mathbf{E}}{\partial t^2} = 0 \qquad\qquad \boldsymbol{\nabla}^2 \mathbf{H} - \mu\varepsilon \frac{\partial^2 \mathbf{H}}{\partial t^2} = 0 \tag{3.14}$$

for the incident plane wave in Fig. 3.2 can be expressed as a sum of the incident and reflected waves such that

$$\mathbf{E} = \begin{cases} (\mathbf{E}_1 e^{-i\mathbf{k}_1 \cdot \mathbf{r}} + \mathbf{E}'_1 e^{-i\mathbf{k}'_1 \cdot \mathbf{r}}) e^{i\omega t}, & x < 0 \\ (\mathbf{E}_2 e^{-i\mathbf{k}_2 \cdot \mathbf{r}} + \mathbf{E}'_2 e^{-i\mathbf{k}'_2 \cdot \mathbf{r}}) e^{i\omega t}, & x > 0 \end{cases} \tag{3.15}$$

and the magnetic field vector can be calculated as

$$\mathbf{H} = \frac{i}{\omega\mu} \boldsymbol{\nabla} \times \mathbf{E} \tag{3.16}$$

It should be noted that in Eq.(3.15), $\mathbf{E}_{1,2}$, $\mathbf{E}'_{1,2}$ are complex vectors; $\mathbf{k}_{1,2}$ is the wave vector of the incoming and transmitted wave, whereas $\mathbf{k}'_{1,2}$ serve as x-z plane mirror images of their respective counterpart.

For a TE polarised wave (s wave), $\mathbf{E}$ is transverse to the plane of incidence and is as such perpendicular to the plane of incident at every point. Applying the boundary conditions from Eq.(3.13) to $\mathbf{E}_z$ and $\mathbf{H}_x$ results in

$$\begin{aligned} E_{1z} + E'_{1z} &= E_{2z} + E'_{2z} \\ \sqrt{\frac{\epsilon_1}{\mu_1}}(E_{1z} - E'_{1z})\cos(\theta_1) &= \sqrt{\frac{\epsilon_2}{\mu_2}}(E_{2z} - E'_{2z})\cos(\theta_2) \end{aligned} \tag{3.17}$$

This can be written in matrix form:

$$D_s(1)\begin{pmatrix} E_{1s} \\ E'_{1s} \end{pmatrix} = d_s(2)\begin{pmatrix} E_{2s} \\ E'_{2s} \end{pmatrix} \tag{3.18}$$

where the dynamical matrix of the s wave for medium i is

$$D_s(i) = \begin{pmatrix} 1 & 1 \\ \sqrt{\epsilon_i/\mu_i}\cos(\theta_i) & -\sqrt{\epsilon_i/\mu_i}\cos(\theta_i) \end{pmatrix} \tag{3.19}$$

for $i = 1, 2$. Presuming incidence from $i = 1$, we obtain the reflection and transmission coefficients as

$$r_s = \left(\frac{E'_{1s}}{E_{1s}}\right) \qquad t_s = \left(\frac{E_{2s}}{E_{1s}}\right) \quad \text{, where } E'_{2s} = 0. \tag{3.20}$$

Assuming that $\mu_2 = \mu_1$, which holds for most dielectric materials at optical wavelengths, we apply the boundary conditions from Eq.(3.17) to get

$$r_s = \frac{n_1\cos\theta_1 - n_2\cos\theta_2}{n_1\cos\theta_1 + n_2\cos\theta_2} = \frac{k_{1y} - k_{2y}}{k_{1y} + k_{2y}} \tag{3.21}$$

$$t_s = \frac{2n_1\cos\theta_1}{n_1\cos\theta_1 + n_2\cos\theta_2} = \frac{2k_{1y}}{k_{1y} + k_{2y}} \tag{3.22}$$

where n_1, n_2 are the refractive indices of each respective medium (for a more general form); $k_{\kappa y} = n_\kappa \frac{\omega}{c}\cos\theta_\kappa$ and $\kappa = 1, 2, 3$ (specific case in Fig. 3.1).

A TM polarised wave (p wave) is categorised by a magnetic field vector **H** perpendicular to the plane of incidence. We examine the reflection and refraction of a TM wave (Fig. 3.2(b)) such that we apply the boundary conditions from Eq.(3.13) to obtain

$$\begin{aligned} (E_{1p} + E'_{1p})\cos\theta_1 &= (E_{2p} + E'_{2p})\cos\theta_2 \\ \sqrt{\frac{\epsilon_1}{\mu_1}}(E_{1p} - E'_{1p}) &= \sqrt{\frac{\epsilon_2}{\mu_2}}(E_{2p} - E'_{2p}) \end{aligned} \tag{3.23}$$

Similarly to Eq.(3.18), we can express this as the dymanical matrix of the p wave

$$D_p(1)\begin{pmatrix} E_{1p} \\ E'_{1p} \end{pmatrix} = D_p(2)\begin{pmatrix} E_{2sp} \\ E'_{2p} \end{pmatrix} \tag{3.24}$$

such that

$$D_p(i) = \begin{pmatrix} \cos\theta_i & \cos\theta_i \\ \sqrt{\epsilon_i/\mu_i} & -\sqrt{\epsilon_i/\mu_i} \end{pmatrix} \tag{3.25}$$

for $i = 1, 2$. Defining r_p, t_p similarly to Eq.(3.20) such that

$$r_p = \left(\frac{E'_{1p}}{E_{1p}}\right) \quad t_p = \left(\frac{E_{2p}}{E_{1p}}\right) \quad \text{, where } E'_{2p} = 0. \tag{3.26}$$

we get[1]

$$r_p = \frac{n_1\cos\theta_2 - n_2\cos\theta_1}{n_1\cos\theta_2 + n_2\cos\theta_1} = \frac{n_1^2 k_{2y} - n_2^2 k_{1y}}{n_1^2 k_{2y} + n_2^2 k_{1y}} \tag{3.27}$$

$$t_p = \frac{2n_1\cos\theta_1}{n_1\cos\theta_2 + n_2\cos\theta_1} = \frac{2n_1^2 k_{2y}}{n_1^2 k_{2y} + n_2^2 k_{1y}} \tag{3.28}$$

By rearranging Eq.(3.18) and Eq.(3.24), we can express the changes in the propagating wave in Fig. 3.1 due to effects at the interface as

$$\begin{pmatrix} R_1 \\ L_1 \end{pmatrix} = D_1^{-1} D_2 \begin{pmatrix} R'_2 \\ L'_2 \end{pmatrix} \equiv D_{12} \begin{pmatrix} R'_2 \\ L'_2 \end{pmatrix} \tag{3.29}$$

$$\begin{pmatrix} R_2 \\ L_2 \end{pmatrix} = D_2^{-1} D_3 \begin{pmatrix} R'_3 \\ L'_3 \end{pmatrix} \equiv D_{23} \begin{pmatrix} R'_3 \\ L'_3 \end{pmatrix} \tag{3.30}$$

where D_1,D_2,D_3 are the matrices defined in Eq.(3.19) for s, and Eq.(3.25) for p waves.

The matrices $D_{12} \equiv D_1^{-1}D_2$ and $D_{23} \equiv D_2^{-1}D_3$ could then be thought of as *transmission* matrices, which describe the changes in the field as it's transmitted across a boundary. The transmission matrices are different for TE and TM waves such that

$$D_{12} = \begin{pmatrix} \frac{1}{2}\left(1 + \frac{k_{2y}}{k_{1y}}\right) & \frac{1}{2}\left(1 - \frac{k_{2y}}{k_{1y}}\right) \\ \frac{1}{2}\left(1 - \frac{k_{2y}}{k_{1y}}\right) & \frac{1}{2}\left(1 + \frac{k_{2y}}{k_{1y}}\right) \end{pmatrix} \quad \text{for a TE wave,} \tag{3.31}$$

[1]Making the same assumptions and definitions as those in Eq.(3.22)

and

$$D_{12} = \begin{pmatrix} \frac{1}{2}\left(1+\frac{n_2^2 k_{1y}}{n_1^2 k_{2y}}\right) & \frac{1}{2}\left(1-\frac{n_2^2 k_{1y}}{n_1^2 k_{2y}}\right) \\ \frac{1}{2}\left(1-\frac{n_2^2 k_{1y}}{n_1^2 k_{2y}}\right) & \frac{1}{2}\left(1+\frac{n_2^2 k_{1y}}{n_1^2 k_{2y}}\right) \end{pmatrix} \quad \text{for a TM wave,} \tag{3.32}$$

The transmission matrices D_{23} are similarly expressed. By using the Fresnel transmission and reflection coefficients r_s, t_s, r_p, t_p defined in Eq.(3.22),3.28, the transmission matrices for both s and p waves can be defined as

$$D_{12} = \frac{1}{t_{12}} \begin{pmatrix} 1 & r_{12} \\ r_{12} & 1 \end{pmatrix} \tag{3.33}$$

This, along with Eq.(3.7), provides a complete way to relate the amplitudes R_1, L_1 to R_3', L_3' by

$$\begin{pmatrix} R_1 \\ L_1 \end{pmatrix} = D_1^{-1} D_2 P_2 D_2^{-1} D_3 \begin{pmatrix} R_3' \\ L_3' \end{pmatrix} \tag{3.34}$$

This is the formulation of the transfer matrix method for a single layer. We can then extend this to a structure containing multiple homogenous isotropic media placed between two semi-infinite media. An illustration with some useful definitions can be seen in Fig. 3.3

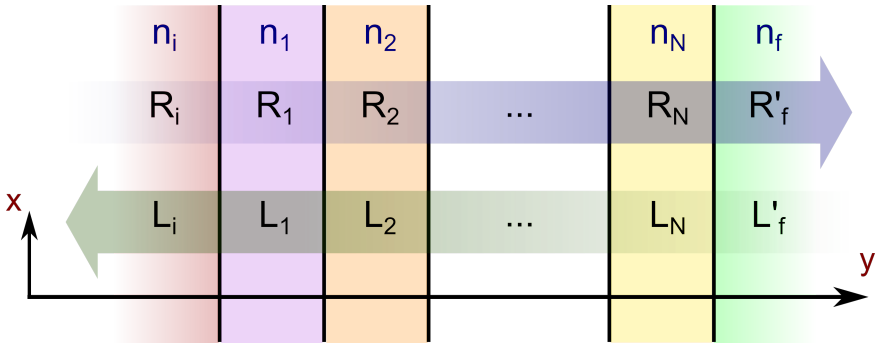

Figure 3.3: *An arrangement of dielectric layers. The amplitudes of the E fields has been labeled, with R_i and L_i corresponding to the wave at the boundary between the n_i and n_1 dielectrics; R_f' and L_f' are similarly labeled for the boundary between the n_N and n_f layers.*

By applying the same methodology as the single layer case in Fig. 3.1, we observe that

$$\begin{pmatrix} R_i \\ L_i \end{pmatrix} = D_i^{-1} D_1 \begin{pmatrix} R_1 \\ L_1 \end{pmatrix} \tag{3.35}$$

$$\begin{pmatrix} R_j \\ L_j \end{pmatrix} = P_j D_j^{-1} D_{j+1} \begin{pmatrix} R_{j+1} \\ L_{j+1} \end{pmatrix} \tag{3.36}$$

where $j = 1, 2, \ldots, N$. The propagation matrices P_j, as well as the transmission matrices D_j, D_i, and D_f, are defined accordingly with Eq.(3.7) and Eq.(3.33) respectively. We can then formalise the relationship between R_i, L_i and R'_f, L'_f as

$$\begin{aligned} \begin{pmatrix} R_i \\ L_i \end{pmatrix} &= D_i^{-1} \left(\prod_{j=1}^{N} D_j P_j D_j^{-1} \right) D_f \begin{pmatrix} R'_f \\ L'_f \end{pmatrix} \\ &= \begin{pmatrix} M_{11} & M_{12} \\ M_{21} & M_{22} \end{pmatrix} \begin{pmatrix} R'_f \\ L'_f \end{pmatrix} \end{aligned} \tag{3.37}$$

This is the formulation of the transfer matrix method for any $N + 2$ layers. As this allows us to calculate the amplitudes of the reflected and transmitted waves, we can further see that as the coefficients of reflectance r and transmittance t are defined as

$$r = \left(\frac{L_i}{R_i} \right) \quad t = \left(\frac{R_f}{R_i} \right) \quad \text{, where } L_f = 0 \tag{3.38}$$

By then applying the transfer matrix method (Eq.(3.37)), we obtain

$$r = \left(\frac{M_{21}}{M_{11}} \right) \quad t = \left(\frac{1}{M_{11}} \right) \tag{3.39}$$

Assuming that the dielectric layer i is lossless, we can obtain the reflectance R by

$$R = |r|^2 = \left| \frac{M_{21}}{M_{11}} \right|^2 \tag{3.40}$$

Provided the edge dielectrics refractive indices (n_i, n_f) are both real, and if the incident and transmitted waves have real[2] wavevector $\mathbf{k}$ then we can calculate the transmisstance T by

$$T = \frac{n_f \cos\theta_f}{n_i \cos\theta_i} |t|^2 = \frac{n_f \cos\theta_f}{n_i \cos\theta_i} \left| \frac{1}{M_{11}} \right|^2 \tag{3.41}$$

[2]Such that θ_i, θ_f are real

3.3 Finite-Difference Time-Domain (FDTD) Method

The FDTD method is a powerful modelling tool which solves for E and H through the spatial, frequency, and temporal domains [56]. While finite difference methods had been used for modelling previously, it was Kane Yee in 1966 who first formalised a method of using a central finite difference for Maxwell's curl equations to calculate **E**,**B** on a grid of staggered cuboid cells, later called Yee cells [53]. The term "FDTD" was first used by Taflove in 1980 [57].

Because it is an explicit method for solving Maxwell's equations, FDTD is a growingly popular tool among computational electromagnetics researchers. A particular strength arises from the discretisation of the simulation volume into voxels, or rather the ability to specify a material for each Yee cell such that complex structures could be simulated without the need for complicated reformulation of integrals; limits in the complexity of simulated structures arise from the finesse of the meshing grid. What's more, because it's a time domain technique, the use of a broadband source means we can record the time-evolution of EM waves across the whole frequency domain in one simulation.

To understand the approximations and mechanism behind the FDTD method, we start by representing Maxwell's curl equations[3]

$$\frac{\partial \mathbf{B}}{\partial t} + \boldsymbol{\nabla} \times \mathbf{E} = 0 \tag{3.42}$$

$$\frac{\partial \mathbf{D}}{\partial t} + \boldsymbol{\nabla} \times \mathbf{H} = \mathbf{J} \tag{3.43}$$

in a Cartesian coordinate system such that

[3] In an isotropic medium

$$-\frac{\partial H_x}{\partial t} = \frac{1}{\mu_0}\left(\frac{\partial E_z}{\partial y} - \frac{\partial E_y}{\partial z}\right) \tag{3.44}$$

$$-\frac{\partial H_y}{\partial t} = \frac{1}{\mu_0}\left(\frac{\partial E_x}{\partial z} - \frac{\partial E_z}{\partial x}\right) \tag{3.45}$$

$$-\frac{\partial H_z}{\partial t} = \frac{1}{\mu_0}\left(\frac{\partial E_y}{\partial x} - \frac{\partial E_x}{\partial y}\right) \tag{3.46}$$

$$\frac{\partial E_x}{\partial t} = \frac{1}{\epsilon_0}\left(\frac{\partial H_z}{\partial y} - \frac{\partial H_y}{\partial z} - J_x\right) \tag{3.47}$$

$$\frac{\partial E_y}{\partial t} = \frac{1}{\epsilon_0}\left(\frac{\partial H_x}{\partial z} - \frac{\partial H_z}{\partial x} - J_y\right) \tag{3.48}$$

$$\frac{\partial E_z}{\partial t} = \frac{1}{\epsilon_0}\left(\frac{\partial H_y}{\partial x} - \frac{\partial H_x}{\partial y} - J_z\right) \tag{3.49}$$

These equations relate the changes in $\mathbf{E}$ with time, to changes in $\mathbf{H}$ across space. A discrete spatial and temporal domain is necessary to obtain numerical solutions; as such, a voxel mesh of Yee cells is used to approximate the FDTD computational domain. An illustration of a Yee cell is shown in Fig. 3.4a, along with some definitions of the electric and magnetic field components.

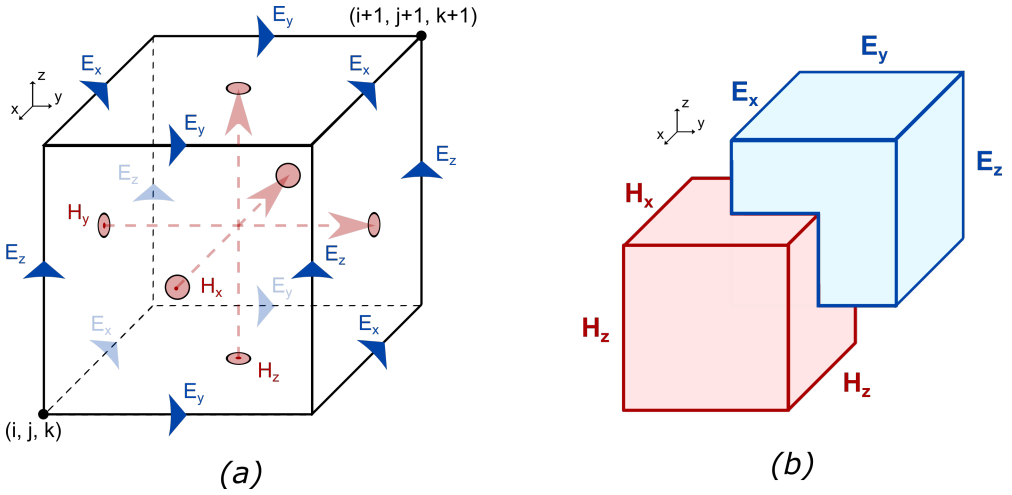

Figure 3.4: *(a) The E and H fields in a Yee cell, such that $E_{x,y,z}$ form the edges and $H_{x,y,z}$ face normals; (b) E and H components within a Yee lattice.*

We perform an estimation of Maxwell's curl equations by discretising the intergral with a central difference approximation. To formulate this, we define i, j, k as the position indices along the spatial axes such that Δx, Δy, Δz are the dimensions of the Yee cell, and observe that

$$-\left(\frac{H_z^{t+\frac{1}{2}\Delta t}(i+\frac{1}{2},j+\frac{1}{2},k+1)-H_z^{t-\frac{1}{2}\Delta t}(i+\frac{1}{2},j+\frac{1}{2},k+1)}{\Delta t}\right)=$$
$$\frac{1}{\mu_0}\left(\frac{E_y^t(i+1,j+\frac{1}{2},k+1)-E_y^t(i,j+\frac{1}{2},k+1)}{\Delta x}-\right.$$
$$\left.\frac{E_x^t(i+\frac{1}{2},j+1,k+1)-E_x^t(i+\frac{1}{2},j,k+1)}{\Delta y}\right)$$

corresponds to Eq.(3.46) (with similar expressions for Eq.(3.44) and Eq.(3.45)), and

$$\frac{E_x^t(i+\frac{1}{2},j,k)-E_x^{t-1}(i+\frac{1}{2},j,k)}{\Delta t}=$$
$$\frac{1}{\epsilon_0}\left(\frac{H_z^{t-\frac{1}{2}\Delta t}(i+\frac{1}{2},j+\frac{1}{2},k)-H_z^{t-\frac{1}{2}\Delta t}(i+\frac{1}{2},j-\frac{1}{2},k)}{\Delta y}\right.$$
$$-\frac{H_y^{t-\frac{1}{2}\Delta t}(i+\frac{1}{2},j,k+\frac{1}{2})-H_y^{t-\frac{1}{2}\Delta t}(i+\frac{1}{2},j,k-\frac{1}{2})}{\Delta z}$$
$$\left.+J_x^{t-\frac{1}{2}\Delta t}(i+\frac{1}{2},j,k)\right)$$

corresponds to Eq.(3.47) (with similar expressions for Eqns.(3.48, 3.49))[4].

The FDTD method uses these equations to calculate the instantaneous values for one of the fields at $t=\tau$ by using values of the other one at the previous time interval $t=\tau-\frac{1}{2}\Delta t$. The coordinates and construction of the Yee cells is such that for a sufficiently small voxel, the electromagnetic field does not vary considerably. This is expressed[5] as the stability criterion

$$\sqrt{(\Delta x)^2+(\Delta y)^2+(\Delta z)^2}>c_{max}\Delta t \tag{3.50}$$

where c_{max} is maximum speed of light in the simulation region. It should be noted that even though this is a simple form of the stability criterion for a grid of identical Yee cells, it can be extended for non-uniform meshing as well. The specific meshing and boundary methods used in this thesis are further discussed below.

[4]In the case of lossy materials, these equations become more complicated, but the FDTD method can still be applied

[5]For constant ϵ,μ

For the purpose of this thesis, a commercially available software was used to do FDTD simulations [9].

3.3.1 Meshing

It can be seen that we need a well refined mesh in order to accurately model structures. This can pose a problem because it significantly increases the simulation time[6]. To resolve this issue, a conformal meshing technique (CMT) available in the Lumerical FDTD solver is used. Conformal meshing allows for subcell changes in pajermittivity, which allows for significant increases in the Yee cell size while retaining the same simulation accuracy by using the Yu-Mittra method [58]; the result is a decrease in the simulation time by $\approx 90\%$. Furthermore, the mesh is graded such that the cell dimensions are a function of position; the result is a smaller mesh near interfaces such that they're better approximated Fig. 3.5.

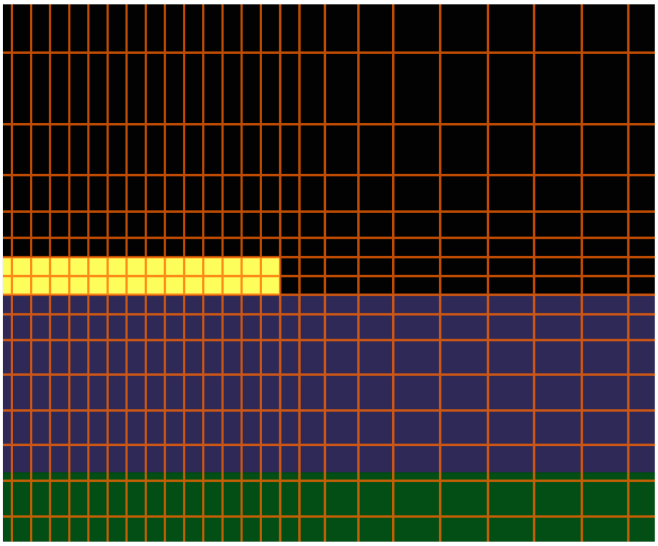

Figure 3.5: *A not-to-scale X-Y illustration of the conformal mesh around the metal edges. The metal disc (yellow) serves as an anchor to the mesh, with GaAs and AlAs represented in dark blue and green respectively. The black background serves only to contrast the orange mesh lines, it does not mark a component in the CTP structure.*

3.3.2 Dipole Source

A point-like electric dipole object is used as a source in the simulations in this thesis. The dipole is placed either 8nm above the lower boundary of the spacer layer (for CTP),

[6]The time it will take for the computer to run the calculations, not to be confused with the time domain to be simulated

or in the middle of the cavity layer (for micropillars). This is because the application of conformal meshing to metals[7] can modify the local density of states, and it is therefore unwise to place the source closer than ≈ few 10s of nm; furthermore, as can be seen in Eq.(18) the emitter-cavity coupling is strongest when the source is placed at the peak of the E-field, which is in the middle of the micropillar cavity layer (Fig. 1.1(a)).

To simulate quantum dot emission, the dipole moment needs to be oriented perpendicular to the growth direction [59]. Defining the y-axis as the growth direction in this thesis, we point the dipole along the x-axis for simplicity. As such, the dipole moment is oriented such that the z-axis is the structure-parallel dipole-perpendicular direction, the x-axis is the structure-parallel dipole-parallel direction, and the y-axis is the structure-perpendicular dipole-perpendicular (cavity) direction. The dipole position and orientation have been illustrated in Fig. 3.8. In the first moments of the simulation, the point-like charge is oscillated, producing a toroidal radiation pattern with the polarisation axis directed in a direction normal to the vertical (emission) direction.

In this thesis, we want to observe the effects over a wide range of frequencies rather than try to accurately emulate a narrow-emission quantum dot; therefore, a broadband Gaussian is produced by an oscillating point charge acting as an electric dipole Fig. 3.6.

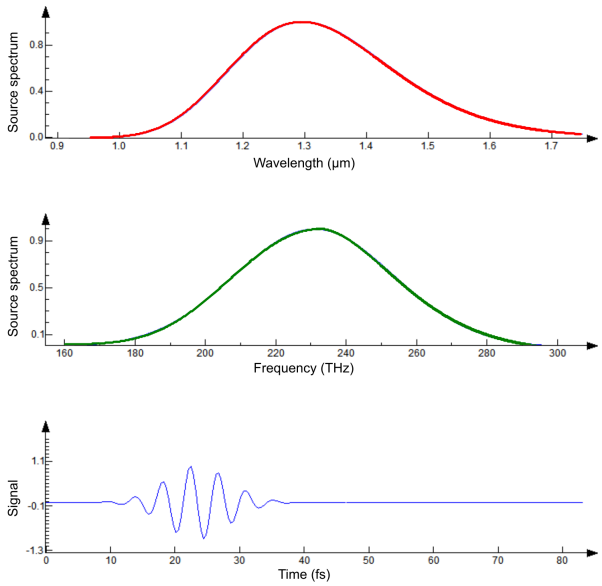

Figure 3.6: *The normalised spectrum (as a function of wavelegnth, frequency) of the dipole used in this thesis. Also displayed is the time signature of the signal i.e. normalised point charge oscillations.*

[7]More accurately, to materials with $\mathrm{Re}(\epsilon) < 1$

3.3.3 PML Boundary

The computational domain must have some boundary as it cannot be infinite. Reflections at these surfaces could iterfere and introduce significant errors to the accuracy of the simulation. The one most widely used is the perfectly matched layer (PML) boundaries [56]. Since their initial proposal by Berenger in 1994, PML boundaries have been used due to their function to absorb incoming electromagnetic waves with minimal reflection [60]. The commercial solver used in this thesis uses a more advanced boundary, known as a convolutional PML (CPML), which can better attenuate evanescent waves [61][62]. The fundamental property of the PML is that the wave equation is formulated in stretched coordinate space; specifically, the derivative $\partial/\partial x_i$ becomes

$$\frac{1}{1+\frac{i\sigma(x_i)}{\omega}}\frac{\partial}{\partial x_i} \tag{3.51}$$

where x_i represents one of the three spatial coordinates x, y, z. This causes attenuation in propagating plane waves because the solution to the wave equation $e^{i(k_i x_i - \omega t)}$ becomes

$$\frac{e^{i(k_i x_i-\omega t)}}{e^{\frac{k_i}{\omega}\int^{x_i}\sigma(x_i')dx'}} \tag{3.52}$$

An artificial $\sigma(x_i)$, which increases with the respective depth within the PML, is introduced to absorb waves emitted by the structure with minimal reflection.

3.3.4 Symmetry

A further tool for reducing the computational domain significantly is the use of symmetry. A symmetrical boundary is a 2-D plane through the coordinate system origin which serves as a plane of symmetry for the (bisected) simulation region such that only half of it needs to be simulated. There are two types of symmetrical boundaries, the properties of which have been presented in Fig. 3.7, such that the symmetrical boundary is shown in orange, and each shaded region is "removed" from the computational domain.

The presence of a symmetric BC through the middle of the computational domain effectively reduces the volume to be simulated by a factor of $\frac{1}{2}$. As the CTP structure to be simulated is a gold disc on top of a semi-infinite DBR and substrate, we reduce the volume of the simulation region by $\frac{1}{4}$ by placing two symmetrical boundaries through the centre of the structure (and consequentially, the dipole). Due to the dipole orientation along the x axis, we select an antisymmetric boundary normal to the X axis, and a symmetric boundary normal to the Z axis[8]. This allows for higher accuracy while

[8]To confirm that the appropriate symmetric BCs were chosen, a simulation of an identical structure

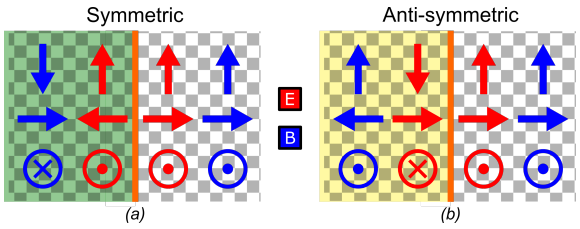

Figure 3.7: *An illustration of symmetric (a) or antisymmetric (b) boundary conditions. The E and B fields are marked red and blue, respectively. The coloured regions are within the simulation region, but not in the computational domain.*

keeping computing times reasonable.

An illustration showing the symmetrical boundaries used in this thesis, as well as the PML layers and dipole orientation, is presented in Fig. 3.8.

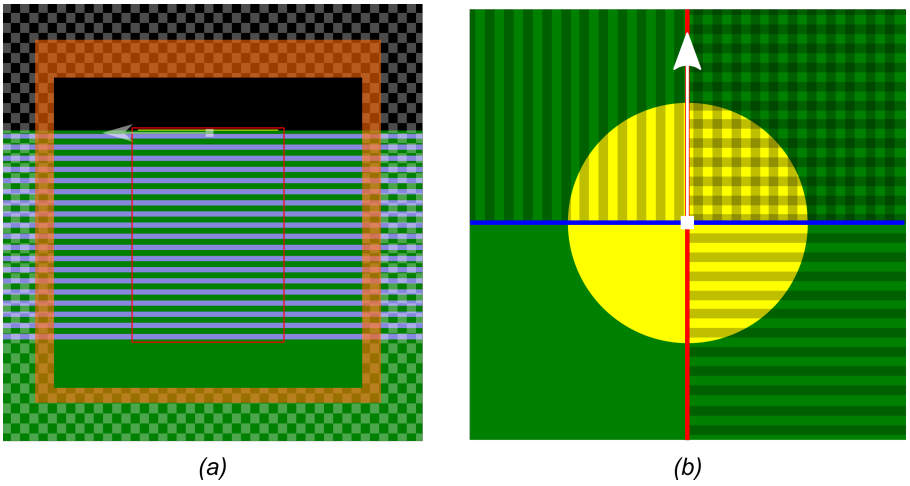

Figure 3.8: *(a) A not-to-scale illustration of the X-Y cross section of the CTP structure used. Several simulation objects are depicted: the 17.5x DBR pairs of GaAs and AlAs layers in green and blue respectively; the gold disc in yellow; the PML region in orange; the dipole source and direction with a white square and arrow, oversized for clarity; and the boundaries of the transmission box in red. The shaded region is out of the computational domain. (b) An X-Z plane (bird's view) of the structure, showing the top GaAs (spacer) layer in green, gold disc in yellow, and dipole in white. The blue and red lines show the antisymmetric and symmetric boundaries respectively such that only the non-shaded region is simulated.*

3.3.5 Materials

In this thesis we simulate emission in a GaAs/AlAs distributed Bragg reflector on a GaAs substrate; additionally, a disc made of gold is present when examining Tamm Plasmons; as such, fitted values for n_{GaAs} [63], n_{AlAs} [64], and n_{Au} [65] are used to accurately represent the materials used. Because we simulate the InAs QD as an os-

but without symmetry BCs present was used for comparison and was found to give the same results.

cillating point charge, that material is not used. The completely real n_{GaAs}, n_{AlAs} are shown in Fig. 3.9(a), whereas the real and imaginary components of n_{Au} in (b).

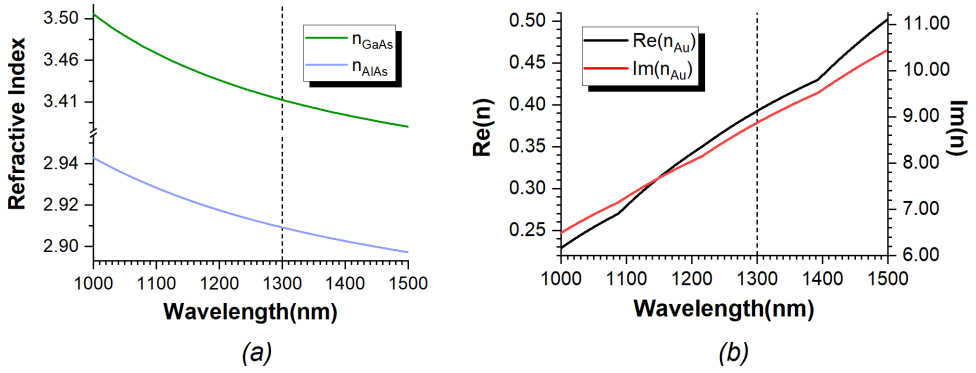

Figure 3.9: *(a) Refractive indices of the DBR materials as a function of wavelength. (b) The real and imaginary parts of n_{Au} where the real part in black corresponds to the left y-axis, and the imaginary in red to the right y-axis.*

3.3.6 Data Monitors

The FDTD method calculates the field components throughout the simulation spatial and temporal domains. To record all that information would require unreasonable amounts of memory, seriously increasing the computing resources required. In the commercial FDTD solver used this is solved with data monitors, one- (point/line) or two- (surface)[9] dimensional objects which collect data to be saved. Two types of data monitors are used to collect measurements: field power monitors, which measure the field components (and Poynting vector) in the frequency domain; and field time monitors, which record the field components in the time domain.

To measure the power transmission though the metal disc Tamm structures simulated in this thesis, a transmission box is formed by 6 plane power monitors. For clarity, we define the edges of the structure such that the top is the metal-air boundary in the y (growth) direction, the sides as the metal-air tangential edges of the disc along the x and z axes, and the bottom as the boundary between the bottom layer of the DBR and the GaAs substrate. While performing initial simulations to ensure that the simualtion is correctly constructed, I found that placing the transmission box plane monitor on the structure edges produced artifacts and results inconsistent with either theory or other published work on FDTD GaAs Tamm Plasmon emitters. This issue was resolved by introducing a 100nm margin between the edges of the structure, and the faces of the

[9] 3D information can be obtained through periodic 2D plane monitors.

transmission box.

The utilisation of time monitors is expanded on further in section 3.4.3.

3.4 Brightness Calculations

In this section I explain the ways in which the raw information from the data monitors is used to work out the brightness (and associated values such as the β- and η-factor), as well as how values relating to the cavity QED, such as the Purcell factor F_P or the Q-factor are calculated.

3.4.1 Power Transmission

The transmission into the cavity and vacuum modes is measured by circumscribing the simualted structure with a 3D transmission box (Fig. 4.2), the six faces of which are frequency domain power monitors at a 100nm margin away from the outer edges of the structure. Each of the monitors records the un-normalised power transmission through each face such that we observe 3 transmission channels[10]:

1. The top transmission, corresponding to the E-field which couples out of the CTP and out of the structure, i.e. 'is emitted'.

2. The bottom transmission, corresponding to the E-field which has coupled into the vertical modes, but is emitted through the DBR and into the substrate rather than the desired direction.

3. The side transmission, corresponding to the E-field coupling into the side loss channels, and is emitted into the DBR and effectively lost. In this thesis, the sum of the power through the 4 side faces is calculated as the total side transmission.

In order to work out the Purcell factor, we consider

$$F_P = \frac{\Gamma}{\Gamma_0} \tag{3.53}$$

where Γ is the spontanious emission rate enchanced by coupling into the cavity resonance modes, and Γ_0 is the spontaneous emission rate in bulk. Values for Γ and Γ_0 are provided by internal functions of the FDTD software used. The Purcell factor can be used to normalise the power transmission values such that

$$T_{Top/Sides/Bottom} = \frac{T_{top/sides/bottom}}{F_P} \tag{3.54}$$

[10]In the case of CTP emitters, there is an additional lossy channel which has been discussed further in Sec. 4.3

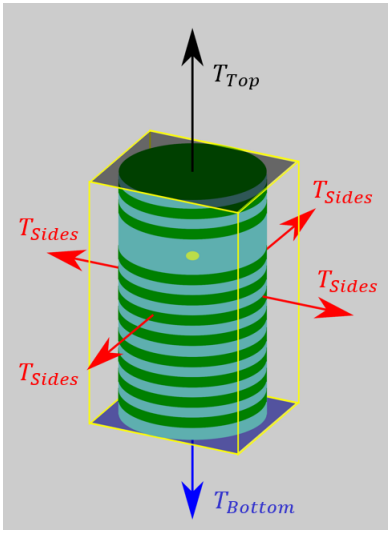

Figure 3.10: *The transmission box which encloses the micropillar, formed by 6 plane power transmission monitors.*

where the lowercase labels correspond to the raw power reading from the monitors.

Active Coupling, Passive and Internal Efficiency

The spontaneous emission coupling factor β is calculated[11] as

$$\beta = \frac{\Gamma_{Cavity}}{\Gamma_{Cavity} + \Gamma_{Loss}} = \frac{T_{top} + T_{bottom}}{F_P} = T_{Top} + T_{Bottom} \tag{3.55}$$

What the β-factor represents is the likelihood of a photon coupling to the cavity mode and being emitted in a vertical direction, which is why it works out as simply the normalised top and bottom transmissions. However, not every photon in the cavity mode can be extracted, as some might decay into the GaAs substrate. How much of the light within the cavity will exit through the top is given by the *passive efficiency* of the cavity, labeled as the η-factor, which we calculate as

$$\eta = \frac{T_{Top}}{T_{Top} + T_{Bottom}} \tag{3.56}$$

We can then observe that the interal efficiency of the emitter, defined as the proportion of excitations which result in a photon emitted out of the structure (in the Top emission channel), labeled as ξ, can be worked out as

[11] This way of working out the β-factor is only appropriate when there is no absorption; as such, the method for working out the active coupling of Tamm plasmon devices is slightly different and has been expanded on in Chapter 5.

$$\xi = \beta\,\eta \tag{3.57}$$

$$= (T_{Top} + T_{Bottom})\,\frac{T_{Top}}{T_{Top} + T_{Bottom}} \tag{3.58}$$

$$\xi = T_{Top} \tag{3.59}$$

3.4.2 Farfield Projection and Collection Efficiency

To inspect the effects of both varying the metal thickness and detuning on the device brightness, measurements of the far-field projection of the E-field transmitted into the top channel is necessary. A field-domain power monitor placed above the structure collects the E-field profile, and projects the far field angular distribution of $|E|$ for $90 \geq \theta \geq -90$. In this chapter, this information is analysed such that we calculate a collection efficiency as a function of NA such that the collection efficiency within an NA corresponding to a solid angle 2Θ

$$\text{Col.Eff. } (\Theta) = \frac{\int_0^{\Theta} |E(\theta)|^2}{\int_0^{\pi} |E(\theta)|^2} \tag{3.60}$$

$$\text{Col.Eff. (NA)} = \frac{E_{\text{Within } 2\Theta}}{E_{\text{Total}}} \tag{3.61}$$

where $\text{NA} = \sin\Theta$ for air (n=1). This further informs of the device's performance as it tells us how much of the emitted light can be feasibly collected within some benchmark NA. To further calculate the % of photons that can be sucessfully extracted, we define a total efficiency, i.e. extraction efficiency such that

$$\text{Tot.Eff (NA)} = \xi \times \text{Col.Eff (NA)} \tag{3.62}$$

$$\text{Tot.Eff (NA)} = T_{Top} \tag{3.63}$$

$$\text{Col.Eff (NA)} \tag{3.64}$$

3.4.3 Q-factor Calculations

The use of time domain monitors in this text is twofold. Three separate line monitors are used to visualise the time evolution of the electric fi

eld magnitude along the axes, such that each line passes through the dipole source. These record E at every Yee cell along the line for every discrete time step in the simulation, effectively visualising the motion of the EM waves through the structure. The second use of time monitors is to measure the E-field within the cavity layer,

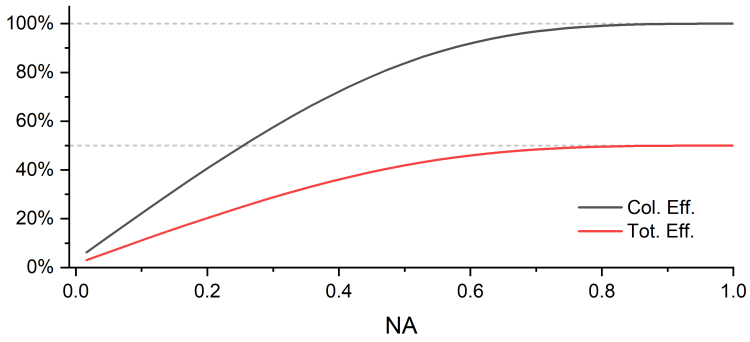

Figure 3.11: *A representative illustration of the collection and total efficiencies of a HE11 mode as functions of NA, with $\xi = 50\%$.*

which can be used to estimate the Q-factor of the structure. It is possible to obtain the Q-factor from theresonance spectrum (obtained by taking the Fourier transform of $E_{Cavity}(t)$) by simply using the spectroscopic definition of the Q-factor to get

$$Q = \frac{\lambda_{Cavity}}{\Delta\lambda} \tag{3.65}$$

where the denominator is the full width at half maximum of the resonance spectrum.

At very high Q-factors this requires a significant resolution of the fourier transform, resulting in unreasonable simulation times and data sets. This problem is solved by the fact that the Q-factor is also calculated with the slopes of the resonance decays. Observing that the time domain of the

field is

$$E_{Cavity}(t) = e^{-r(\alpha - i\omega_r)}u(t) \tag{3.66}$$

where α is the decay constant, we note that the fourier transform of $E_{Cavity}(t)$ is

$$|E(\omega)|^2 = \frac{1}{\alpha^2 + (\omega - \omega_r)^2} \tag{3.67}$$

This fourier transform reaches a maxima at $\omega = \omega_r$, with half-max at $\omega = \omega_r \pm \alpha$. With 2α as the FWHM, we observe that

$$\alpha = \frac{\omega_r}{2Q} \tag{3.68}$$

From there, we observe that as α is the decay constant of $E(t)$, we can relate Q to the slope m of the log of the time signal envelope such that

$$\log_{10}(|E(t)|) = -\frac{\omega_r t}{2Q}\log_{10}(e) = mt \tag{3.69}$$

We can then calculate the Q-factor as

$$Q = \frac{-\omega_r \log_{10}(e)}{2m} \tag{3.70}$$

Simulating Confined Tamm Plasmons

4.1 Overview

When designing single photon devices which use coupling to Tamm plasmons, one of the key parameters to consider is the thickness of metal to be deposited on top of the spacer (cavity) layer, which notably affects how strongly light emitted by the quantum dot couples into the side modes, as well as the absorption rate due to the presence of the gold. As these are by far the two most significant factors contributing to the device inefficiency, investigating how the rates of emission into these loss channels vary with the metal layer is of interest.

This chapter begins with a discussion on the Tamm plasmon resonance condition ($r_{DBR}r_M = 1$) to expand on the fact that due to the dependence of r_{DBR} on the spacer layer and r_M on the metal layer, varying one while keeping the other to a fixed value changes the wavelength of the Tamm resonance, λ_{TP}. Because of the resulting difference in the resonance wavelengths λ_{DBR} and λ_{CTP} (i.e. detuning), the resulting emission is sub-optimally bright and as such, the probability of emission into loss channels is increased.

By using the transfer matrix method to probe the reflectivity of 1-D Tamm plasmon structures, a set of metal and spacer depths resulting in a mode centered at 1300nm is established in this chapter, and labeled as the metal-spacer relationship (MSR) for convenience. Using the finite-difference time-domain method, the effects of variations along the MSR on the internal efficiency are compared with detuned devices where the spacer is kept fixed at 75nm, showing significantly smaller emission spectral shift, as well as a brighter emission at all metal thickness values.

Considering the far field projection of the emitted E field, visible effects of the metal on the angular distribution are discussed. Three regions within the metal variations range are identified, with significant deformation of the HE11 mode observed if the metal is too thin or thick. Peak values of $|E|$ are visibly larger in MSR- as opposed to

fixed spacer variations. To provide a quantitative analysis of the changes in the far field, the collection efficiency as a function of numerical aperture is calculated. Observations reveal an optimum/maximum at $d_m = 16.5$ nm of metal in both the MSR and fixed spacer variations. While the behaviour of the collection efficiency is similar in both cases, MSR variations result in better collection efficiency at relevant NA values when the $d_m \geq 15$ nm (thick enough for proper Tamm plasmon formation). The combined effects on the internal and collection efficiency are also presented in the form of total efficiency. By observing total efficiency as a function of NA, it can be observed that a maximum occurs at 16nm metal thickness, and further concluded that devices with metal and spacer values along the MSR show significant improvements over detuned devices.

Finally, investigations into a 2-D slice of a spatially resolved frequency domain of the E-field in the 16nm metal (optimal extraction efficiency) reveal visible effects of the improved coupling to the cavity modes in the devices where the spacer depth is determined by the metal depth via the established metal-spacer relationship. By measuring $|E|$ as a function of time within the cavity, the resonance spectrum is shown to be $\lambda_{CTP} \approx 1289.5$ nm, revealing de-tuning in the MSR device due to the differences in the TMM method used for probing the MSR, and the more accurate 3-dimensional FDTD simulations. The time evolution of the E-field along the cartesian axes (centered on the quantum dot) is also discussed.

4.2 Introduction

When designing confined Tamm plasmon emitters, it can be said that there are three primary components which either emit, transmit, or reflect light of a certain wavelength within the structure, such that they contribute to the wavelength and brightness of the Tamm plasmon coupled emission:

1. **The quantum dot:** the wavelength at which the QD emitts light into the cavity (λ_{QD}) is determined by the size of the InAs islands within the spacer layer. Ideally, λ_{QD} would be as near to the cavity resonance peak as possible, though this is not a factor that can be controlled within the fabrication stage.

2. **The DBR:** the thickness of the alternating GaAs and AlAs layers determine the reflectivity and transmissivity of the DBR. The thicknesses are determined by $\frac{\lambda_{DBR}}{4n}$ where n is the refractive index of GaAs or AlAs respectively at λ_{DBR}.

3. **The Tamm plasmon:** the Tamm plasmon wavelength ($\lambda_{TP/CTP}$)[1], is dependent on the metal and spacer thickness.

[1]Throughout this chapter, λ_{TP} signifies a TMM (one dimentional) Tamm plasmon wavelength es-

Each of these elements is optimised for a certain wavelength (λ_{QD}, λ_{DBR}, λ_{TP}). Within a small range around $\lambda \pm \delta\lambda$ each component will function at a reduced efficiency, filtering part of the light out; outside of that range, it will result in negligible brightness of the component. As such, for optimal efficiency, it is necessary not only to optimise each element individually, but ensure that spectrally, the Tamm plasmon and the DBR are optimised for the same wavelength. Devices where $\lambda_{TP} \neq \lambda_{DBR}$ are labeled as detuned in this thesis.

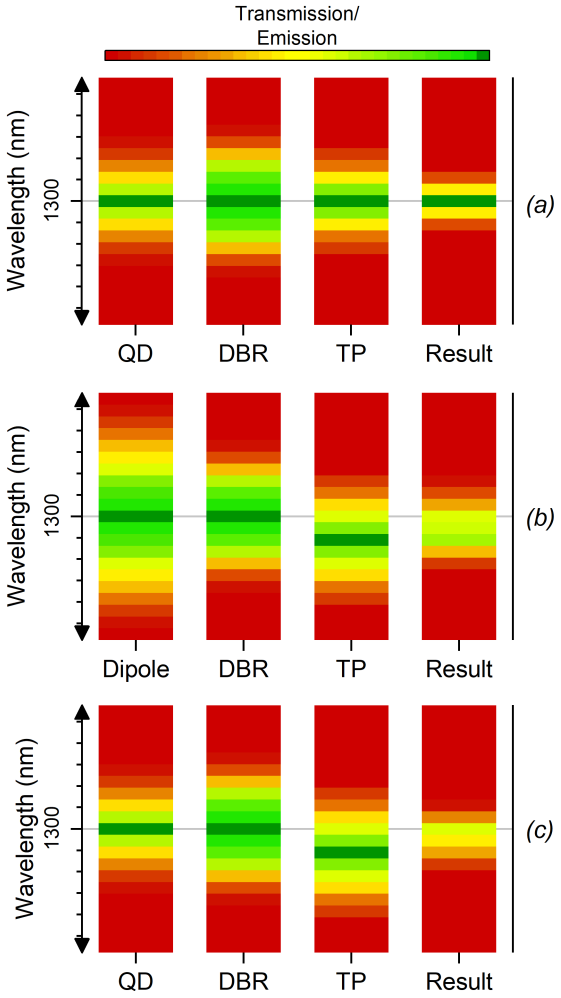

Figure 4.1: *(a) A well tuned CTP device, i.e. one where $\lambda_{QD} = \lambda_{DBR} = \lambda_{TP}$, resulting in bright and spectrally centered emission as the device brightness is not affected by detuning. (b) A detuned device where the source is a broad Gaussian, such as the one used in these simulations. Due to $\lambda_{TP} \neq 1300$ nm, the resulting emission is spectrally shifted and dimmed. (c) A detuned device where the source is a narrow quantum dot emission, i.e. realistic. The observed effect is a dimmer emission, but no change in the peak wavelength λ_{Result}.*

timation, whereas λ_{CTP} denotes a three dimensional confined Tamm plasmon obtained by FDTD simulations.

The concept of matching the wavelength is illustrated in Fig. 4.1, with green colour representing peak emission/transmission, yellow representing 50% of the peak brightness, and red representing almost no emission/transmission at that wavelength. Each column represents a component, while the internal efficiency resulting from the multiplication of the other three. A well tuned CTP device, such as the representation in Fig. 4.1(a), does not contain elements which filter light between elements, resulting in emission unobstructed by component detuning. As a contrast, in Fig. 4.1(b) we note that due to $\lambda_{TP} \neq \lambda_{DBR}$, we observe less bright peak emission. Furthermore, it should be noted that the wavelength at which brightness peaks is not necessarily the cavity resonance wavelength (i.e. $\lambda_{peak} \neq \lambda_{TP}$), as illustrated by the different vertical locations of the peaks in the TP and observed emission layers. While not relevant to this thesis, it should be noted that this is not an effect that might be as visible in experimental circumstances, as quantum dots have much narrower emission lines than the dipole in these simulations (Fig. 4.1(c)); regardless, the peak brightness is lower in (c) than in (a) due to filtering by the mismatched Tamm plasmon (i.e. metal-spacer) layer.

4.3 Methods

In this chapter, I examine what are the effects that the metal thickness (labeled as d_m in Fig. 2.8(d)) are on the brightness of Tamm plasmon single photon emitter structures. This parameter sweep of d_m is repeated twice: once when the spacer thickness (d_s) is modified accordingly to result in $\lambda_{CTP} = 1300$ nm, and another time then d_s is kept constant. The purpose of this is to optimise the efficiency while also showing the dimming effects of a detuned system where $\lambda_{CTP} \neq \lambda_{DBR}$.

Active Coupling

While the power transmission and efficiency factors are worked out on the same principles as outlined in Chapter 3, there are differences introduced by the existence of an additional loss channel - the absorption within the gold (metal) layer. As such, the field decays into the cavity, with decay rate Γ_{Cavity}, into vaccum modes with Γ_{Vacuum}, or absorbed with a corresponding absorption decay γ^*. Therefore, I use a slightly different version of working out the β-factor which includes this new loss channel, such that

$$\beta = \frac{\Gamma_{Cavity}}{\Gamma_{Cavity} + \Gamma_{Loss} + \gamma^*} \tag{4.1}$$

$$= \frac{\Gamma_{Cavity}}{\Gamma_{Cavity} + \Gamma_{Loss}}(1 - \alpha) \tag{4.2}$$

$$= \beta'(1 - \alpha) \tag{4.3}$$

$$\text{where } \alpha \equiv \frac{\gamma^*}{\Gamma_{Cavity} + \Gamma_{Loss} + \gamma^*} \tag{4.4}$$

The proportion of the field which is lost in the metal is given by the absorption, labeled as α, such that $T_{Top} + T_{Sides} + T_{Bot} + \alpha = 1$. By measuring the amount of power emitted by the dipole source, and comparing it to the total power through the transmission box pictured in Fig. 4.2a, we can get the un-normalised absorption rate as the difference between the two values. However, unlike the case with micropillars, this means that as not all of the emitted field passes through the transmission box, and as a result $T_{Total} \neq F_P$.

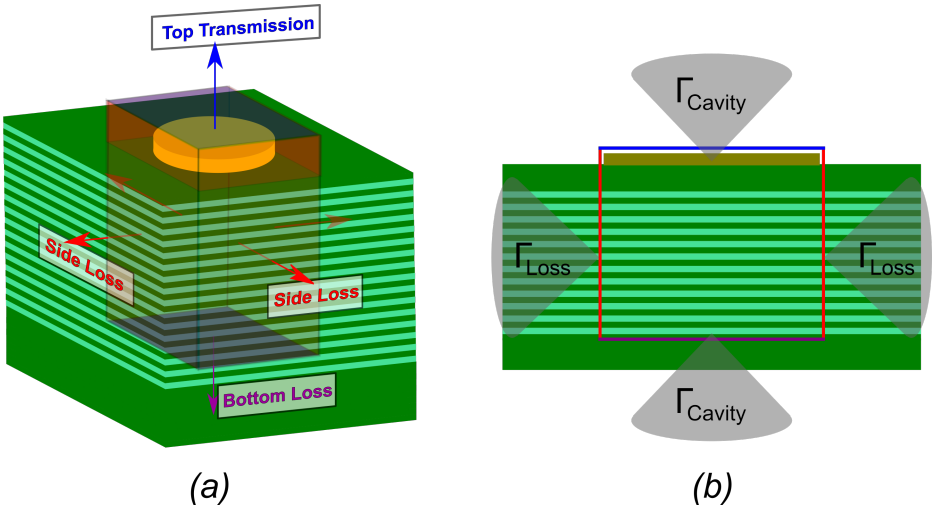

Figure 4.2: *A not-to-scale illustration of the 6 frequency domain power monitors which form the transmission box. (a) A 3D representation of the structure and transmission box, with the two "emmisive" channels labeled. (b) A 2-D cross section of the structure, more closely representing the 100 nm margin between the transmission box faces and the CTP structure.*

Tamm Disc Diameter

The results presented in this chapter are efficiency of the Tamm emitters as the thickness of the gold layer is varied. The aim is to investigate how the internal efficiency and fundamental mode wavelength are affected when the metal depth is varied within a range where $\Delta\lambda_{CTP}/\Delta d_m$ is significant. Reffering to previous computer modelling work concerning GaAs/AlAs based CTPE done by Parker et al. [50], we observe in Fig.

4.3(b) that a sensible range to select is $0 - 35$ nm gold disc thickness[2].

As the effects of the disc diameter on Tamm plasmon emitters has been previously investigated, it is a variable which is to be kept fixed for the simulation purposes of this thesis. An appropriate choice of diameter needs to be made with two effects in mind: the ability of a disc to support multiple modes as the diameter increases (Fig. 4.3(b)); and the spectral shift of the resonant frequency resulting from significant lateral confinement if the disc is too small (Fig. 4.3(a)). Initial observations might suggest that as long as the disc is above a certain diameter, lateral confinement produces a minimal spectral shift; while this is true, we have to keep in mind the issue of resolving the separate modes and isolating our observations to changes of the HE11 mode without interference from changes to the higher order modes. In Fig. 4.3(d), it can be seen that for $0 - 35$ nm gold, the 1-dimensional esimation of the Q-factor is on the order of 10^1, which would make the resolution of emission by modes difficult. It can be seen that at disc diameter $d = 2.5$ μm, at least 6 modes resonate within the $1250 - 1300$ nm wavelength range (LP01, LP11, LP21/LP02, LP31, and LP12). Even if we consider the Q-factor on the high end of the range, ≈ 75, we obtain resonance FWHM values ≈ 17 nm (and FWHM ≈ 31 nm if low Q $= 40$), making the resolution of 6 peaks within this range awkward. Therefore, to balance the effects of lateral confinement and multimodality, the discs simulated in this thesis all have the same diameter $d = 2.25$ μm - at this size, the disc supports a LP01 (HE11) mode spectrally distant from other resonant peaks without introducing significant spectral shift of said HE11 mode.

In this thesis, we also discuss and observe the effects the gold thickness d_{Au} on the far field projection, and consequentially, the fraction of power emitted captured within a solid cone; as such, it should be mentioned that while the disc diameter affects the emission far field significantly, those effects are not taken into consideration or discussed as the disc is kept a constant diameter throughout all simulations [67].

4.4 Investigating λ_{TP} using TMM

To correct for the $\delta\lambda_{TP}$ originating from changes in the metal thickness, the spacer layer has to be varied accordingly such that λ_{TP} remains at the desired wavelength of 1300 nm. Probing for the set of values which satisfy this condition requires a considerable amount of computing resourced to do with FDTD simulations, and as such using a less accurate one dimensional approximation with the transfer matrix method is a suitable alternative. The identification of λ_{TP} comes from the reflectivity of the structure; we

[2]We do, however, anticipate poor (if any) coupling to the Tamm mode when the gold thickness is on the order of 10^0 nm.

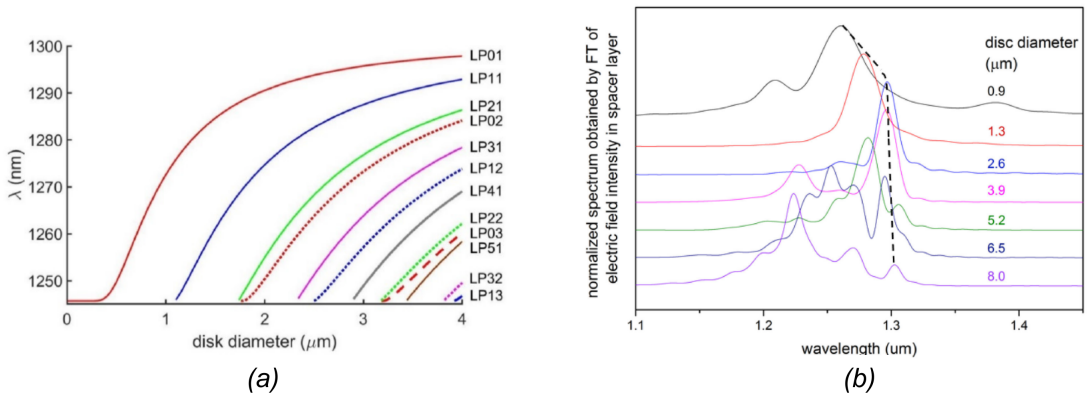

Figure 4.3: *(a) Calculated Tamm wavelength for the first twelve LP modes as a function of disc diameter (such that $d_m = 25$ nm, $d_s = 75$ nm); (b) resonant CTP frequencies for various disc diameters, with the fundamental mode marked by a dashed line; (c) The resonance position as a function of metal thickness for a fixed spacer of 75 nm; (d) Changes in the quality factor as a function of metal thickness. Part (a) of this figure has been recreated from [66], and parts (b)-(d) from [50].*

expect R $\approx$ 1 at most wavelengths within the DBR stop band, except when $\lambda \approx \lambda_{TP}$ and the light couples into the Tamm mode (i.e. $R \approx 0$). Separate variations in the spacer and metal layers, and the resulting changes in λ_{TP} have been presented in Fig. 4.4.

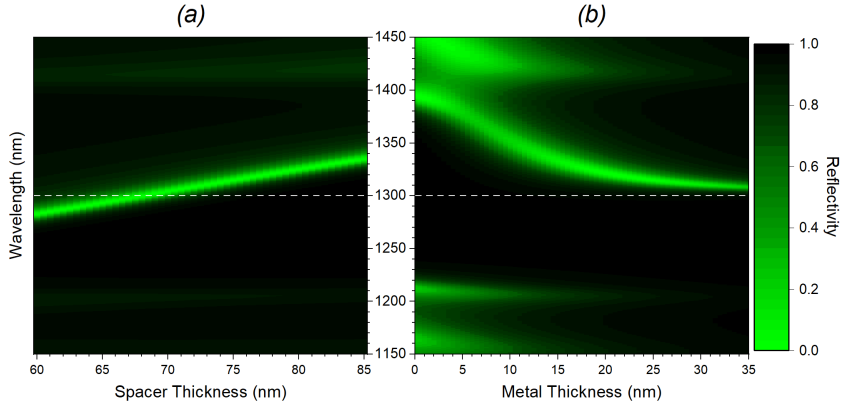

Figure 4.4: *TMM calculations of the reflectivity of TP structures. (a) Variations in the spacer thickness, with a fixed metal thickness of 25 nm; (b) variations in the metal thickness, with a fixed spacer thickness of 75 nm.*

It can be seen in Fig. 4.4(b) that when d_m is below $\approx$ 10-15 nm) there is no TP coupling within the DBR stop band; furthermore, the DBR is still visible to the incoming field, as seen by the variations in the reflected field along the Y axis (wavelength) at $d_m \leq 15$ nm. In the region where there is enough metal ($d_m \geq 15$ nm), we

can observe that despite λ_{TP} being more sensitive to changes in d_s (Fig. 4.4(a)) than it would be to the variations in d_m, there is still visible dependence on both parameters.

We can therefore conclude that there are many combinations of these values such that λ_{TP}= 1300nm. In order to find these values, the reflectivity at 1300 nm of the 1D TP structure at various values of spacer and metal is calculated, producing a plane of reflectivity values (Fig. 4.5). By recording the minima of the reflectivity at each metal thickness, we record the spacer depths which best result in the desired λ_{TP}. To make referencing this constraint of the spacer to the metal thickness, it has been labeled the metal-spacer relationship (MSR).

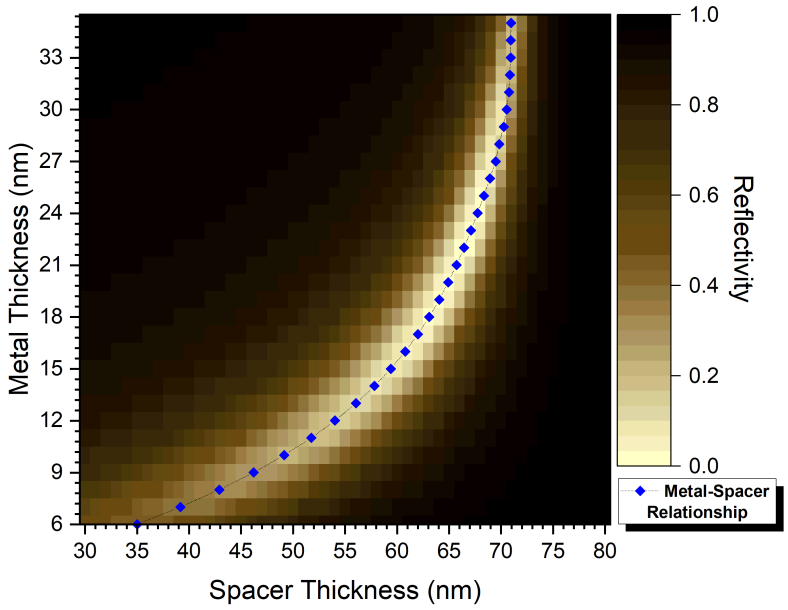

Figure 4.5: *The TMM calculated reflectivity (at $\lambda = 1300$ nm) of the TP stucture, as a function of both metal and spacer thickness. The function mapping the values of lowest reflectivity is the metal-spacer relationship (MSR), marked with blue diamonds*

4.5 Optimisation of the Internal Efficiency (ξ)

By varying the spacer accordingly to the MSR every time the metal layer is changed, is it possible to use FDTD simulations to observe the efficiency of a three dimensional confined Tamm plasmon device without detuning marring the results. We investigate any errors in the MSR by observing T_{Top}, the probability of coupling into the emission mode. Additionally, we compare an MSR-optimised device with a detuned one, such that the spacer has a fixed value of 75 nm despite the metal changing depth. This

spacer was chosen because it does not result in $\lambda_{TP} = 1300$ nm at any metal depth, and should therefore experience some emission filtering. This data is presented as a heatmap in Fig. 4.6.

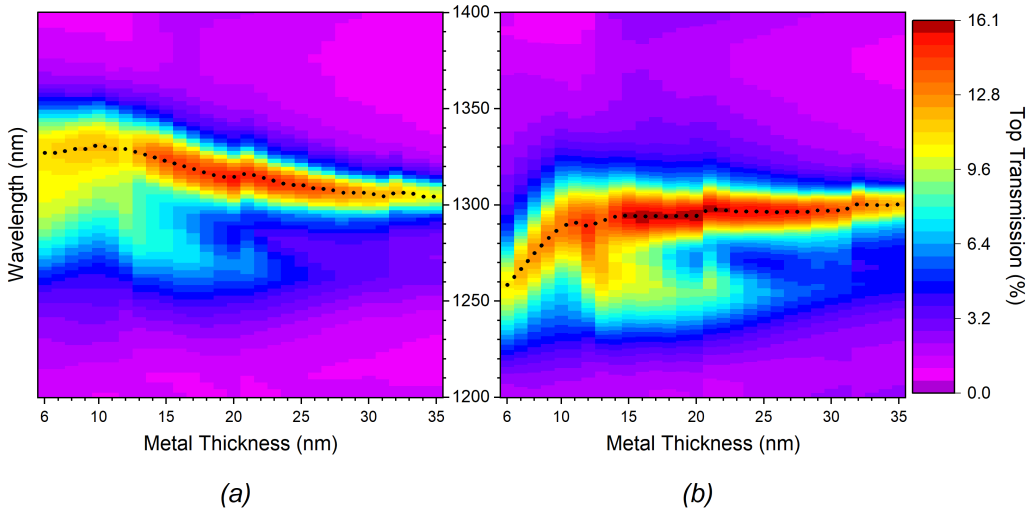

Figure 4.6: *T_{Top} $(= \xi)$ as a function of metal thickness and wavelength. The black dotted line marks the maxima for each metal thickness, showing λ_{Cavity} as a function of metal thickness: (a) when d_m is varied, but the spacer layer is fixed at $d_s = 75$ nm; (b) when both d_m and d_s are varied according to the MSR.*

By observing λ_{Cavity} (black dotted line) in Fig. 4.6(b), it can be noted that the mode remains between $\approx 1295 - 1300$ nm when the metal thickness $d_m \geq 13$ nm. When the metal is thinner than 13 nm, λ_{Cavity} changes considerably and detunes from ≈ 1295 to 1260 nm at $d_m = 6$ nm. There isn't enough metal to impedance match 1300 nm photons, as can be seen from the fact that in Fig. 4.5(f)or each d_m between 6-13 nm, *every* spacer thickness value results in a high reflectivity value (R $\geq$ 0.2) as opposed to other values along the MSR (R $\leq$ 0.05). It can be concluded that the MSR functions sufficiently to account for the spectral shift above 13 nm metal, resulting in a stable $\lambda_{Cavity} \approx 1297 \pm 2$ nm; however, $\lambda_{Cavity} \neq 1300$ nm implies some error and detuning/filtering, as illustrated in Fig. 4.1(b).

Comparing the peak T_{Top} in Fig. 4.6(a-b), we can see that not only are the detuning effects on λ_{Cavity} considerably stronger in (a), but as both figures share the same colourbar, a lower peak T_{Top} for the fixed spacer variations. This also means a lower internal efficiency ξ when there is considerable filtering due to detuning. One could observe that the brightest emission seems to occur around the same $d_m \approx 15 - 20$ nm) in both variations, suggesting the increase in metal reduces emission into some, but increases the emission in other loss channels. The competing effects result in a maxima, an optimal value along the MSR for internal efficiency.

To better investigate this effect, the rates of emission into each channel (T_{Top}, T_{Sides}, T_{Bottom}, as well as α) at λ_{TP} as functions of d_m for both the MSR and fixed spacer parameter sweeps have been displayed in Fig. 4.7(a), with the emission efficiency factors/metrics in (b).

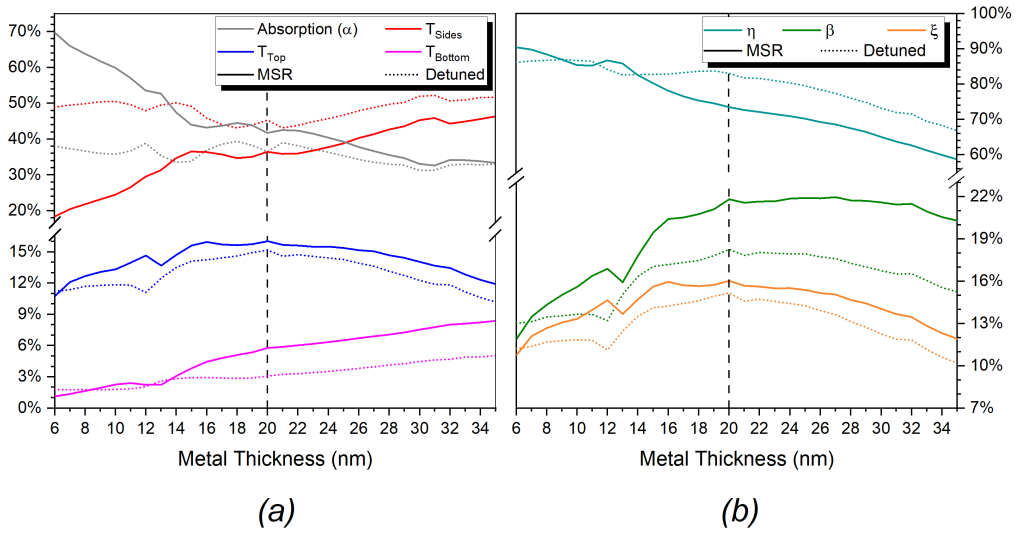

Figure 4.7: *(a) The transmission coefficients (and absorption) of λ_{TP} at each metal thickness, where the dotted lines show the trends when only the metal is varied (fixed spacer=75nm), and the full lines corresponding to variations along the MSR. (b) The emission efficiency factors as a function of metal thickness.*

It is evident that at every metal thickness, a CTP device based on the MSR has a superior internal effici ency ξ than the other (detuned) device. It could also be noted that T_{Top} behaves similarly, with the maxima occuring at $d_m = 20$ nm for both MSR and fixed spacer variations. This indicates an observation of similar changes in the photonic properties of the system, but the detuned CTP structure experiences filtering due to $\lambda_{DBR} \neq \lambda_{CTP}$, and is therefore less bright.

An explanation for the shape of T_{Top}, or ξ, can be found in the behaviour of the 2 largest loss channels; these are the absorption α and the side loss T_{Sides}, displayed as the red and grey lines in Fig. 4.7(a). Perhaps counterintuitively, α does not increase with metal thickness; it decreases as the metal thickness is increased, in both the MSR and the detuned variations. On the other hand, T_{Sides} increases notably with metal thickness, and the point at which is the maxima, at $d_m = 20$ nm.

$$\left(\frac{\Delta T_{Sides}}{T_{Sides}} + \frac{\Delta T_{Bot}}{T_{Bot}}\right) \geq \frac{\Delta\alpha}{\alpha} \tag{4.5}$$

It can further be observed that while the loss channels T_{Sides}, T_{Bot}, α behave ap-

proximately linear when the metal and spacer are varied according to the MSR, they are distorted in the detuned variations due to the design inefficiencies and spectral shift. More light sucessfully couples into the CTP rather than get reflected back into the structure when the device is better tuned, and as a result both α and T_{Top} are greater. Changes in the metal-spacer layers along the MSR result in better coupling into the cavity mode, as evidenced by the higher β-factor in Fig. 4.7(b), and this also results in a greater T_{Bottom}, or smaller η. From Eq.(4.4), Eq.(3.55), and Eq.(3.56), it follows that the maxima in ξ corresponds to the maxima in T_{Top}, i.e.

$$\left[\left(\frac{\Delta T_{Sides}}{T_{Sides}} + \frac{\Delta T_{Bot}}{T_{Bot}}\right) \geq \frac{\Delta\alpha}{\alpha}\right] \equiv \left(\frac{\Delta\eta}{\eta} \geq \frac{\Delta\beta}{\beta}\right) \tag{4.6}$$

Finally, it should be noted that in the detuned variations, α remains approximately constant, and the interesting behaviour of α decreasing with metal thickness is not apparent.

4.6 Total (Extraction) Efficiency

While ξ represents the probability that a photon emitted by the quantum dot is transmitted out of the CTP structure, it does not inform about whether the photon can be easily collected by bulk optics, or an optic fibre. In order to observe the effects on the extractability of the E field captured in T_{Top}, an analysis of the far field is necessary. By plotting the angular distribution of $|E|$ in the far field, the effects of metal thickness has on the shapes of the emission modes, and consequently, on the collection efficiency. This data, along with a comparison to a fixed $d_s = 75$ nm) sweep across the metal thickness, is presented as a heatmap in Fig. 4.8(a).

It can be observed that the metal thickness d_m has a visible effect on the shape of the emission mode. Three regions can be identified; when the metal thickness is:

- $d_m < 13$ **nm:** at insufficient metal for proper impedance matching, we can observe that light in the emission channel (T_{Top}) is distributed in a bullseye shape. An example mode (at 10nm) is represented in green;
- $13 \leq d_m < 25$ **nm:** the metal is ideally thick for the BSW to match to the rest of the CTP structure, resulting in an expected HE11 mode. The peak E-field (to which the data is normalised) is identified at 16nm, and represented in red;
- $d_m \geq 25$ **nm:** too thick, and the resulting mode is distorted and redirected under an angle, resulting in bullseye-like distortion to the mode. An example has been shown in violet.

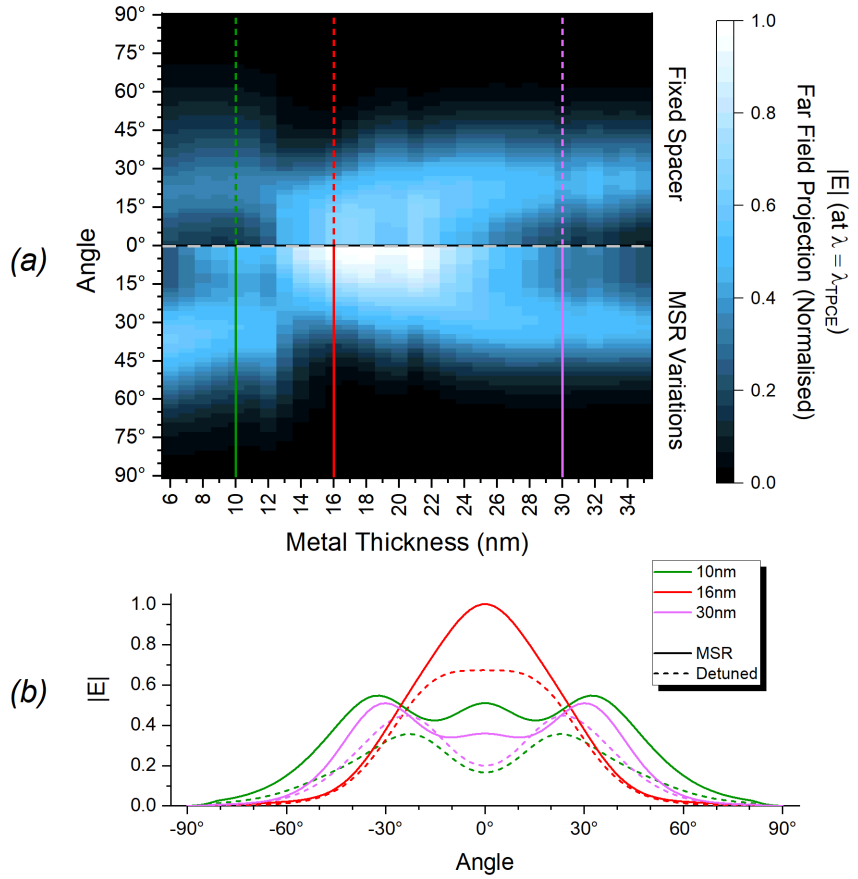

Figure 4.8: *(a) The angle resolved far field projection of E-field at λ_{Cavity} for each metal thickness. The top shows the data when only the metal is varied for a fixed $d_s = 75$ nm, and the bottom when the metal and spacer are varied according to the MSR. (b) Linear representations of $|E|$ for a value of d_m before Tamm formation (10 nm), at the peak E-field (16nm), as well as a higher than optimal value (30nm). Each line corresponds to the same coloured (and styled) lines in (a).*

The modes behave similarly when d_m is varied in both the detuned and MSR variations, with the E-field being brighter when $\lambda_{TP} \approx \lambda_{DBR}$. This suggests that we're observing the same effect in both cases, but with different degrees of filtering due to detuning with the DBR structure underneath. In Fig. 4.8(b), it is clear that the peak-E field occurs in the MSR variations, and the detuned field is dimmer i.e. less enchanced due to inefficient coupling into the Tamm mode and then into the emission mode T_{Top}.

By plotting the wavelength resolved $|E|$ we can compare changes in the far field across the frequency domain rather than just at λ_{Cavity}. This can be seen in Fig. 4.9, at the values of metal thickness marked in Fig. 4.8(a) (shown in (b)).

It can be noted that the modes behave simialrly with metal thickness in both the detuned and MSR variations; however, due to the mismatch between λ_{CTP} and λ_{DBR}

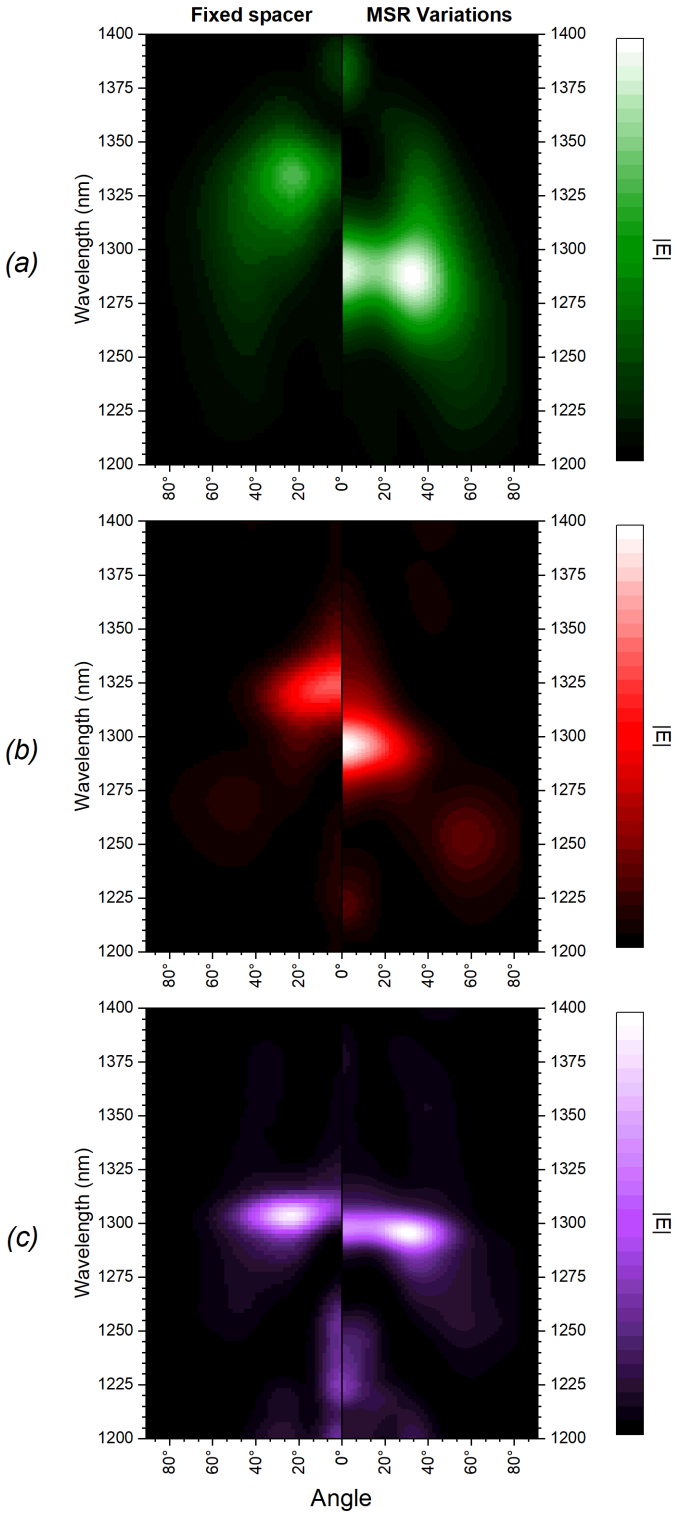

Figure 4.9: *The far field of the emission modes at d_m = (a) 10 nm, (b) 16 nm, and (c) 30 nm. The left side shows the modes for a detuned device when $d_s = 75$ nm constantly, whereas the right side shows CTP devices along the MSR; the colours are analogous to Fig. 4.8.*

when the spacer is kept constant, there is visible difference in the peak of the modes in (a) and (b); this parallels the behaviour of the mode at λ_{Cavity}. In Fig. 4.9(c), when the spacer thickness of the 2 variations is similar enough ($75 \approx 70.5$ nm), and the metal thickness is far from the T_{Top} maximum, the effects on E are mostly visible in the spectral shift of the mode, not in $|E|$.

Spotting that any differences in $|E|$ are most significant for angles $\leq 30^o$ (or NA ≤ 0.5), we identify 3 benchmark NAs to compare the collection (and total) efficiency: $\text{NA}_{smf} = 0.14$, $\text{NA}_{mmf} = 0.22$, and $\text{NA}_{bulk} = 0.5$, where $\text{NA}_{smf/mmf}$ corresponds to a single(multi) moded 1300 nm fibre NA. With that in mind, we measure the changes in the collection efficiency as a function of numerical aperture at various values of d_m to quantify the effects of the metal layer depth on the ease of extractibility of the E field. This data, along with a fixed d_s versial of the metal parameter sweep, has been presented in Fig. 4.10.

As the mode in the far field changes with metal thickness, as evidenced in Fig. 4.9, such that there is a point where the HE11 mode peaks in $|E|$ around $d_m = 16$ nm, we observe a maxima point in the collection efficiency in Fig. 4.10(b) at $d_m = 16.5 \pm 0.5$ nm. When $d_m < 13$ nm, the wide angular distribution of the E-field contributes to a collection efficiency $\leq 65\%$ even within a large NA. In the optimum range for CTP emission, when d_m is between 13-22 nm, the collection efficiency changes similarly in both detuned and MSR variations of the metal and spacer, with a notable $\approx 8\%$ increase within NA_{smf} and NA_{mmf}, despite the only difference in the physical CTP structures $\Delta d_s \approx 10 - 15$ nm . It should also be noted that due to the negligible differences between $|E_{Detuned}|$ and $|E_{MSR}|$ when NA≥ 0.5, there aren't significant differences in the collection efficiency at large collection angles.

Since the collection efficiency only informs us about the distribution of the field within the emission channel, we must consider the total/extraction efficiency of the structure, which takes into acount the probability of a photon coupling into T_{Top}. Similarly to Fig. 4.10, the total efficiency (as defined in Eq.(3.64)) has been shown as a function of NA and metal thickness in Fig. 4.11.

We note in Fig. 4.7(a), T_{Top} has a negative concavity, peaking around $d_m = 20$ nm; similarly, in Fig. 4.10(b) the collection efficiency peaks at $d_m = 16 - 17$ nm. This compounds to similar changes in the total efficiency, as can be noted in Fig. 4.11(b). Furthermore, the total efficiency is maximised at $d_m = 16$ nm in both the MSR and detuned variations of the d_m and d_s; this is approximately the peak of the collection efficiency, and the second peak of T_{Top}, which is close in value to the fist maximum. Due

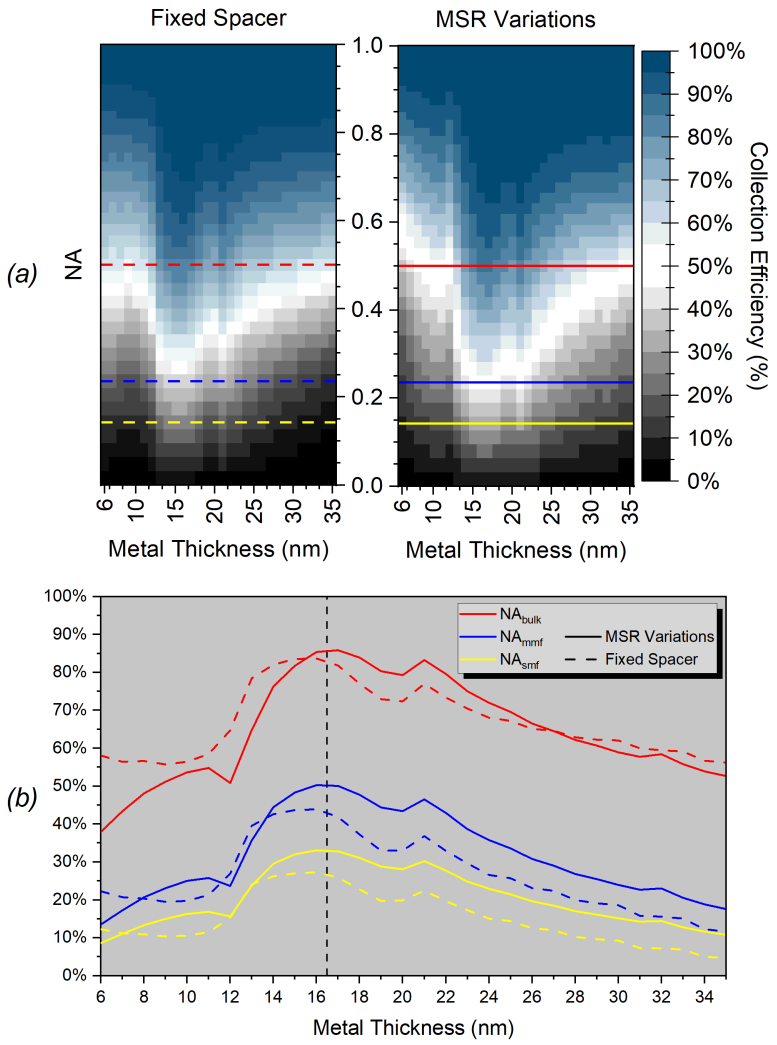

Figure 4.10: *(a) The collection efficiency as a function of NA and metal thickness, for a detuned and MSR varied CTP structure. (b) Line graphs corresponding to the analogously coloured lines in (a), representing the collection efficiency as a function of NA within a single mode and multimode fibre, as well as a bulk optic with NA=0.5.*

to the existence of a clear optimal metal thickness such that the emission into an easily extracted NA is maximised, it can be concluded that the effect of the metal thickness on the brightness of the device is considerable.

Furthermore, we note that when the spacer is fixed, the total efficiency varies with metal thickness similarly but is notably smaller. We can observe that at $d_m \geq 14$ nm, the tuned device (shown in full lines) outperforms the other device, which is detuned by $\Delta\lambda \approx 5 - 30$ nm, where $\Delta\lambda = |\lambda_{CTP} - \lambda_{DBR}|$. This further suggests that to obtain better efficiencies in CTP design, an MSR for the specific materials should be determined and used to constrain the spacer thickness to the metal thickness.

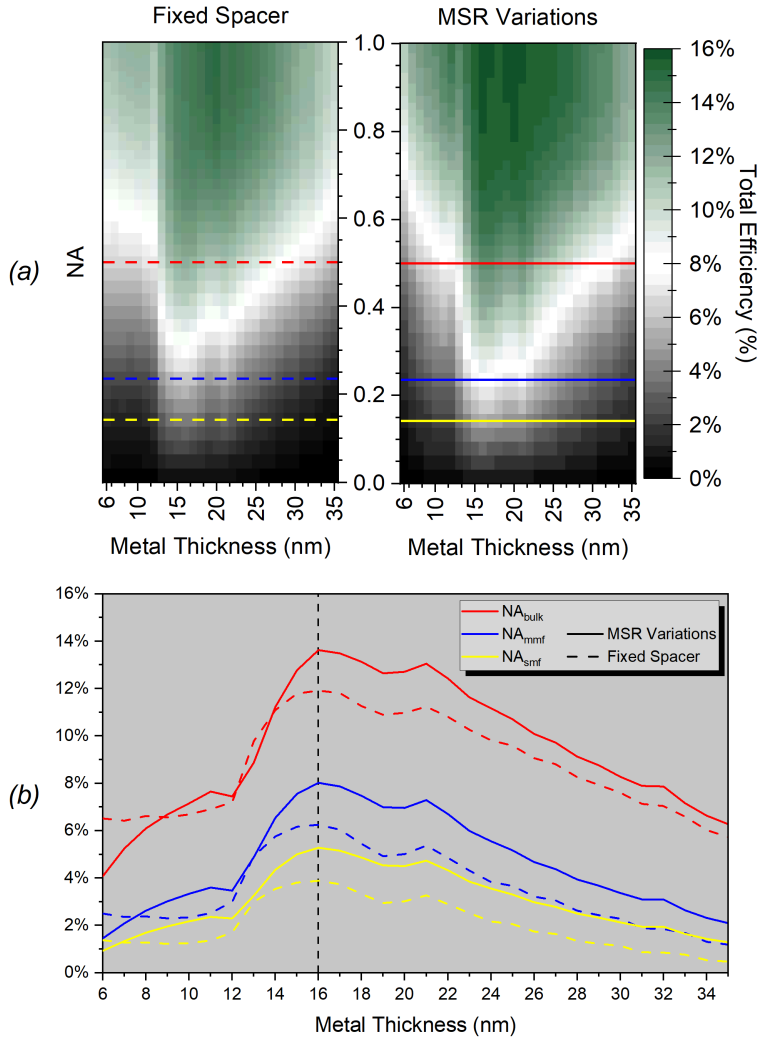

Figure 4.11: *(a) The total efficiency as a function of NA and metal thickness, for a detuned and MSR varied CTP structure. (b) Line graphs corresponding to the analogously coloured lines in (a).*

4.7 E-Field Confinement

By placing a 2-D field-domain power monitor along the X axis through the middle of the CTP structure, we can record and observe $|E|$ as a function of X (along the dipole orientation) and Y (vertical) position, of the field at λ_{Cavity}. This has been presented for the structures with optimal total efficiency ($d_m = 16$ nm) as a heatmap in Fig. 4.12; white dashed lines marking the metal disc radius, and grey horizontal ones the mark the top and bottom faces of the transmission box.

It can be seen that while the general shape of the E field is similar in both cases, better containment of the E field within the cavity mode ($x \leq 1.125\ \mu$m) can be ob-

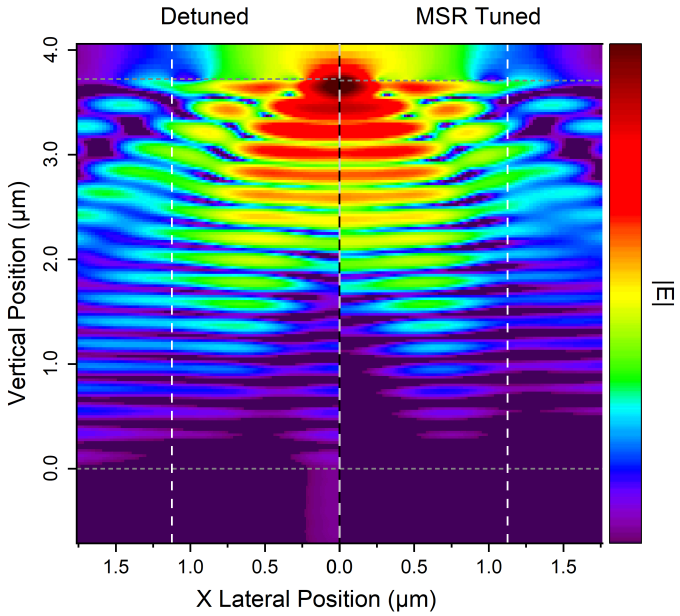

Figure 4.12: *The peak E-field magnitude as a function of depth and lateral position (radial distance) when the metal thickness is 16nm. The left hand side shows the field when the spacer is set to 75 nm (fixed value), whereas the right has a spacer thickness set by the MSR, when the metal thickness is 16 nm. The scaling of the colourbar is logarithmic.*

served around the $0.2 - 1$ μm vertical position, when the structure is well tuned. This is in agreement with Fig. 4.7(a) where the side losses are considerably smaller for the MSR variations. Furthermore, we can observe that the E-field above the disc (in the emission mode T_{Top}) varies strongly with radial distance.

The placement of point-like time-domain monitors within the spacer (cavity) layer provides measurements on the E-field vector within the cavity (the spacer layer); as such, we can observe it's evolution with time, which has been displayed in Fig. 4.13.

By analysing the Fourier transform of Fig. 4.13(a), we can calculate the spectrum of the resonance within the structure. The true wavelength of the resonance, λ_{CTP}, is identified as the maximum in the spectrum local to 1300nm. Further applying a filter to $E_{cavity}(t)$ to isolate the non-resonant frequencies, the decay of the mode can be estimated. This has been shown (for the $d_m = 16$ nm MSR device) in Fig. 4.14.

Using this data, one can estimate the quality factor of the cavity mode by analysing the decay rate, which comes out as $Q_{Decay} = 45.1 \pm 11.4$. Alternatively, as the Q-factor is low enough for the field to fully decay by the end of the simulation time, we can observe the FWHW of the 1289 nm mode in Fig. 4.14(a) and by simply measuring the quality factor as $Q = \frac{\lambda_{CTP}}{FWHM}$ we can estimate that $Q_{Spectrum} = 49.9 \pm 3.2$, which is in

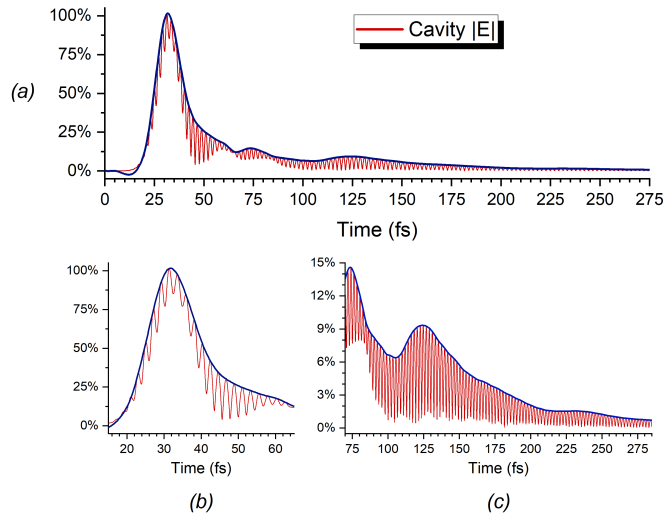

Figure 4.13: *(a) The evolution of the E field within the cavity with time, normalised. The dark blue line is an illustrated upper envelope function. (b)-(c) Recreations of the same data, but re-scaled for regions of interest.*

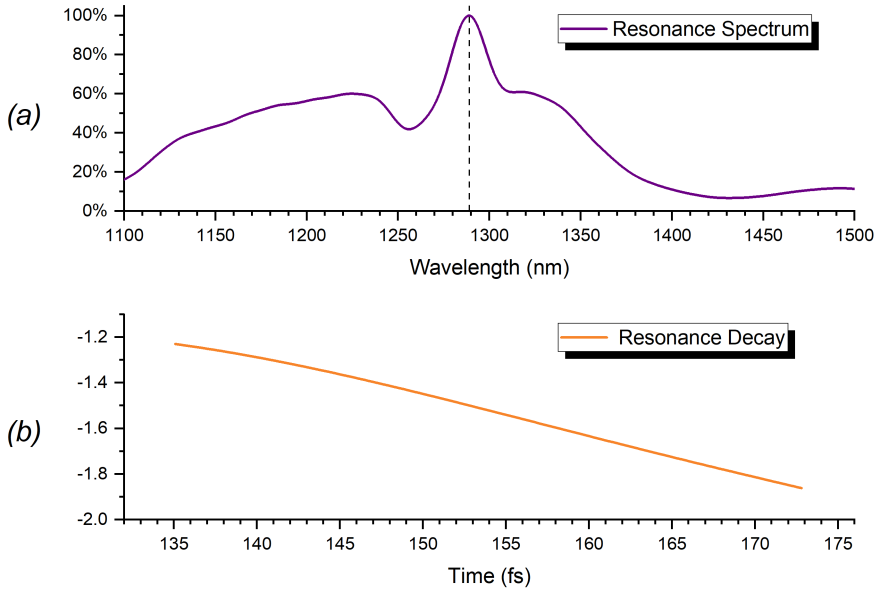

Figure 4.14: *(a) The resonance spectrum of the cavity E field, with the CTP identified at λ_{CTP}=1289.5±0.5 nm with a vertical dashed line. (b) The decay rate of the mode at λ_{CTP}*

agreement with Q_{Decay}[3].

This indicates that the MSR device also experiences detuning, and therefore partially filtering. The true cavity resonance occurs at $\lambda_{CTP} \approx$1289 nm, whereas the DBR is tuned to $\lambda_{DBR} = 1300$ nm; the resulting emission peaks approximately midway at

[3]It could also be noted that this is also in agreement with the Q-factor obtained by analysing the FWHM of λ_{CTP} of the reflectivity obtained by TMM, $Q_{TMM} = 47.68 \pm 2.6$

$\lambda_{TP} = 1295 \pm 0.3$ nm. To get perfect tuning and further increase T_{Top}, the resonance wavelength should match the DBR wavelength. As $\lambda_{Cavity} \approx 1322$ nm when the $d_s = 75$ nm, the extent of detuning and filtering is much larger, resulting in a lower total efficiency of the CTP device.

Using the Q-factor, the Purcell factor, and the resonance (true) central wavelength (Q_{Decay}, F_P, λ'_{CTP} respectively), we can estimate the mode volume to be $V = 1.7 \pm 0.4 \left(\frac{\lambda'_{TP}}{n}\right)^3$.

To visualise the time evolution of the E field along the vertical axis of the CTP structure, a line time-domain monitor was used. By placing it along the central axis through the disc and quantum dot (dipole) piercing through the top and bottom faces of the transmission box, it records $|E|$ as a function of time and position; the results of this are shown in Fig. 4.15.

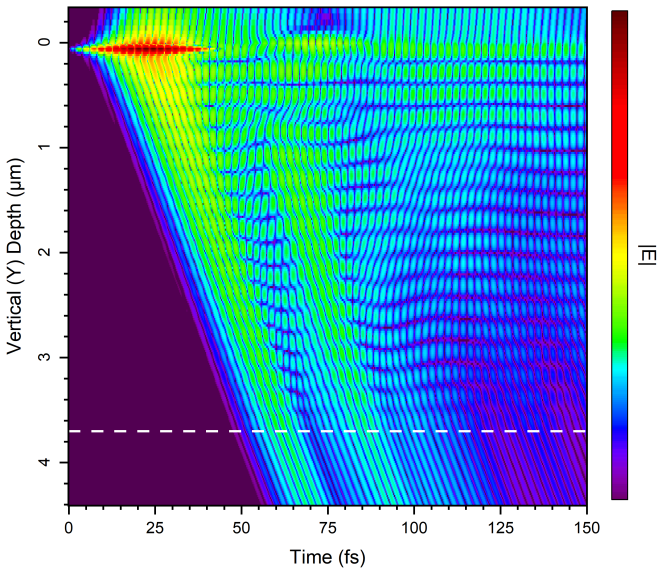

Figure 4.15: *The magnitude of the E-field vector shown on a logarithmic colour scale, as a function of time and vertical position. The zero value on the Y axis corresponds to the top face of the transmission box, whereas the white dashed line corresponds to the bottom.*

The E field peaks at the boundary between the spacer layer and the first AlAs layer of the DBR, as signified by the dark red colour. Most of the emission occurs in the top channel, with the resonant E-field decaying into the top and bottom emission modes as time passes. It can be observed that the transmission into the cavity channels T_{Top} doesn't occur smoothly with time. As expected, it mirrors the peaks and troughs of the cavity E field shown in Fig. 4.13; the transmission into T_{Bottom} happens similarly, with a delay of 50 fs.

We can similarly investigate the decay of the E-field through the side loss channels by placing 2 perpendicular line time-domain monitors through the quantum dot, along the X and Z axes respectively. Keeping in mind that the dipole is oriented along the x direction, we observe the time evolution of the E field along these monitors, displayed as a heatmap in Fig. 4.16

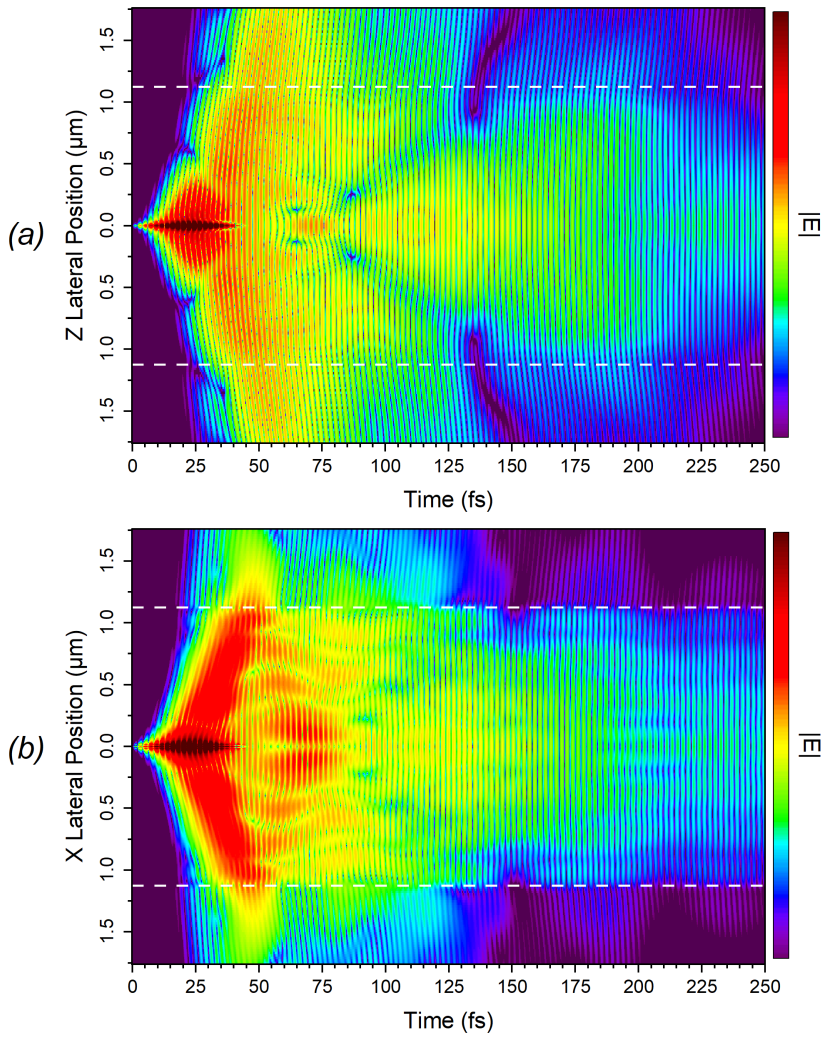

Figure 4.16: *The E field evolution along the (a) Z-axis and (b) X-axis, shown on a logarithmic colour bar.*

We observe a significant side loss in both side loss channels ($T_{Sides,Z}$ and $T_{Sides,X}$) within the first 125 fs of simulation time, resulting in the large T_{Sides} value in Fig. 4.7(a). As the line monitors are placed within the spacer layer, there is no physical boundary at 1.125 μm radial distance; despite this, we can observe the containment of the E-field within the cavity at t >125 fs. This can also be observed in Fig. 4.16(b) at

50-80 fs, where the radial distance of the E-field peaks is decreasing (i.e. the E-field is reflected radially inwards).

4.8 Conclusions

By changing the spacer layer in tandem with the thickness of the metal, the detuning effects of changing λ_{CTP} are counteracted. This allows us to observe the effects of the metal thickness on the brightness clearly, revealing significant changes in the device performance as a bright single photon source. The two main loss channels are affected in opposite ways such that thicker metal results in a lower absorption, but also in increased side losses. The competing effects result in a peak in the internal efficiency represented by the ξ-factor at $d_m \approx 20$ nm.

By looking at the collection efficiency, I've shown that the metal-spacer thickness significantly affects the far-field of the emission, which results in large changes to the proportion of the emission which can be extracted. By looking at the total efficiency, which combines the effects of d_m on both ξ and the collection efficiency, we see that while many combinations of d_m and d_s can result in the same λ_{CTP}, the choice of metal thickness is of significant importance. Furthermore, by considering the same variations in d_m but with a fixed d_s, we see that devices which are optimised according to an appropriate metal-spacer relationship perform better than similar structures with a slightly different spacer.

Designing Low-Q High-Brightness Micropillars

5.1 Overview

In this chapter I show the results of the FDTD simulations of micropilllars emitting at telecom O band wavelengths (1300 nm). The purpose of conducting these calculations is to investigate the theoretical possibility of low-Q pillars with a high brightness. My attempts at maximising ξ are composed of two parts: an investigation into how the active coupling to the cavity changes with the structural parameters discussed in the Chapter 3, and efforts to optimise the passive efficiency of the cavity modes.

Due to the way in which the β-factor changes as the diameter is varied, I begin by presenting the β-factor data for two pillars, one of which has more DBR pairs than the other. This is done to see the effects of the diameter on the β-factor at different Q-factor values. After a brief discussion about underlying cavity QED effects which present the possibility of detemining an optimal diamter before considering the remaining structural parameters, I show the dependence of the internal efficiency ξ on the pillar radius. This identifies an approximate optimal diameter, so furhter pillar simulations occur at D = 2.25 μm.

I follow this by showing how the simulated β-factor is considerably higher than the Purcell-factor estimation for pillars (β^*) with various numbers of top and bottom DBR pairs. By plotting the difference between the calculated (β) and estimated (β^*) values of the active coupling to the cavity modes as a function of the Q-facto r, I show that the Purcell estimation of β is inappropriate for low-Q pillars.

This is followed by a display of simulation results which indicate that high β-factors can be achieved by Q-factors lower by an order of magnitude than previously thought. I also show how the structural changes affect the Purcell enhancement and related values.

The final part of the chapter is focused on my attempts to optimise the cavity passive efficiency by considering the ratio between the top and bottom DBR transmissivity,

calculated with the TMM method. By considering pillars with various permutations of top and bottom DBR pairs, I show the theoretical possibility of low-Q pillars that have sufficient brightness to be used as single photon sources within an NA = 0.45.

5.2 Introduction

Optical micropillars are resonators formed by growing quantum dots in a cavity layer which is then placed between two DBR stacks, one on the "top" of the cavity, meaning between the dot and the desired emission direction, and one on the "bottom", meaning between the cavity and the substrate on which the pillar would rest. The sides are then etched away, leaving a protruding structure which forms the resonator.

This chapter is an investigation in the effects of three parameters on the efficiency[1] of the micropillar as a single photon device. These are the:

- Pillar diameter (D);
- Number of DBR pairs making up the stack above the cavity (Top DBR Pairs);
- Number of DBR pairs between the cavity and the substrate (Bottom DBR Pairs).

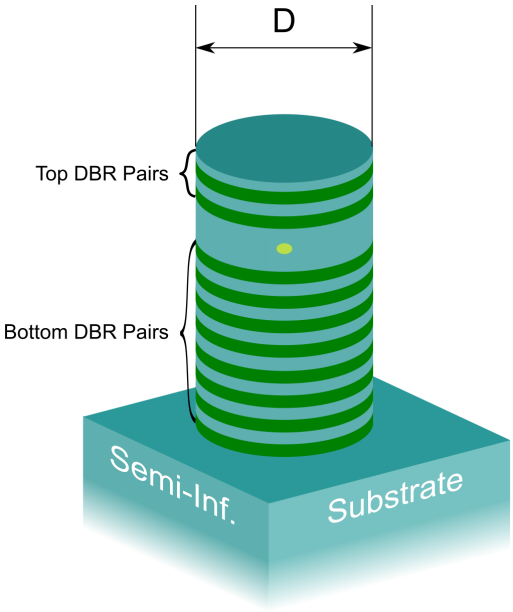

Figure 5.1: *An illustration of a micropillar with the parameters which are examined in this thesis labeled.*

[1]By efficiency I mean the percentage of excitation events that result in a photon being emitted from the top of the structure.

To quantify the device efficiency and compare the pillar performance, I considered the active coupling to the cavity (the β-factor), as calculated by Eq.(3.55), which is the probability of an emitted photon to couple into the vertical cavity modes as opposed to the lossy vacuum modes. I further worked out the η-factor by considering the proportion of the cavity emission in the up as opposed to the down direction, as shown in Eq.(3.56). Multiplying them with eachother gives the internal efficiency of the pillar, represented by the ξ-factor as orked out in Eq.(3.59). These expressions have been replicated below for convenience, with normalisation is as described in Eq.(3.54).

$$\beta = T_{Top} + T_{Bottom}$$
$$\eta = \frac{T_{Top}}{T_{Top} + T_{Bottom}}$$
$$\xi = \beta\ \eta = T_{Top}$$

5.3 Maximising the Active Coupling (β)

5.3.1 Lateral confinement and optimal diameter

By simulating pillars with various diameters, we can calculate the changes in the pillar QED and the resulting variations of the β-factor. Furthermore, by repeating the calculations for a pillar with more DBR pairs on top of the cavity I identify several effects consistent with the explanation of the micropillar cavity quantum electrodynamics in Chapter 2. I have presented these results in Fig. 5.2.

We can note several features from the β-factor dependence on the diameter of the two different pillars in Fig. 5.2:

- The diameter can very significantly affect the β-factor;
- These diameter-induced fluctuations of β occur independently of the number of top DBR pairs;
- The structurally[2] larger pillar couples better to the cavity modes at each diameter than their smaller counterpart;
- In Fig. 5.2(b) we see that the diameter doesn't really affect the Q-factor, and;
- We obtain a variety of β-factors at approximately constant Q-factors.

[2]Meaning has a larger number of DBR layers, as opposed to thicker layers.

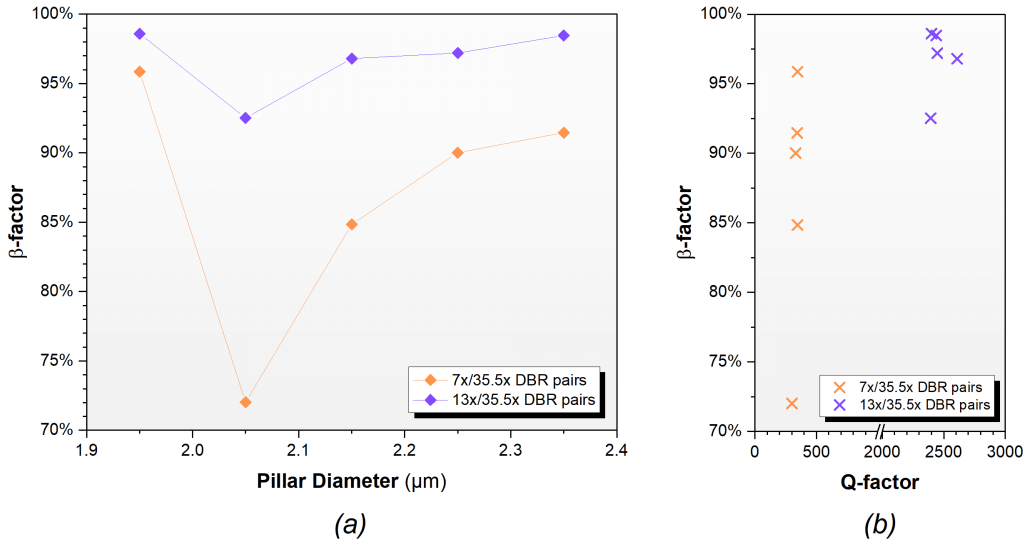

Figure 5.2: *(a) The diameter dependence of the β-factor for two pillars, one of which is has more top DBR layers. (b) Calculated Q-factors for the diameter-variations pillars and the corresponding active coupling to the cavity.*

The data in Fig. 5.2 suggests that the β-factor scaling is independent of the Q-factor; I have presented a possible explanation in section 5.5 because there's insufficient data points to make a full argument. For now it's only necessary to observe that it's possible to achieve the same β with a significantly lower associated Q-factor by selecting an optimal diameter. To do this, I take into account the full effects of the diameter on the internal effiency ξ, shown in Fig. 5.3. Results obtained with the FDTD method.

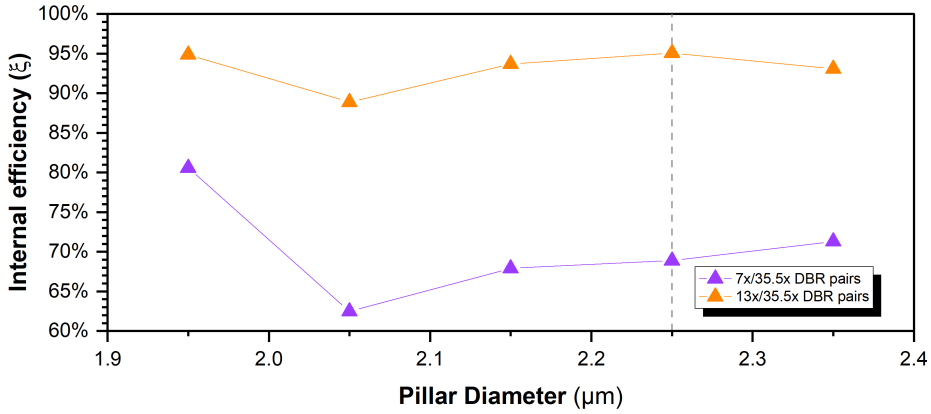

Figure 5.3: *The internal efficiency (ξ) as a function of the pillar diameter, worked out with the FDTD method.*

By considering the internal efficiency[3], I estimated an optimal diameter of approx-

[3]And also $\Delta F_P/\Delta\beta$ as described in section 5.5

imately 2.25 μm. This value sets a local maxima in β at a given (fixed) Q-factor, and is therefore optimal based on how easily we can couple into the cavity modes.

5.3.2 Purcell Enhancement in Low-Q Micropillars

In the previous section I identified an optimal diameter $d = 2.25$ μm based on how *effectively* we can couple into the cavity. The next step is to see how *strongly* we can couple to the cavity by changing the Purcell factor, while still remaining at low-Q values. By now considering structures with various DBR pairs on top and bottom of the cavity layer, we can change the transmissivity of each DBR stack, which has the effect of changing the cavity energy decay rate κ.

For convenience, we organise the pillars in sets where each set has the same amount of bottom pairs, but changing top pairs. I considered a variety of top pairs (3x - 17x), and repeated these calculations three times. I chose numbers of bottom DBR layers which would result in a small (15.5x), medium (20.5x), and large (35.5x) pillars and complements the range of the top pairs well. I have presented my calculated values of F_P, the Q-factor, and the mode volume (V_{Mode}) in Fig. 5.4

By looking at the Q-factor, we can see the effects of the reduced κ due to the added DBR layers. This is further supported by the fact that the Q-factor increases more significantly by adding more pairs on the top rather than the bottom, as the DBR between the cavity layer and the substrate is already highly reflective. This can be easily understood if we think of the total decay rate of the cavity as a combination of the decay through the top and bottom, or

$$\kappa = \kappa_{Top} + \kappa_{Bottom} \tag{5.1}$$

Therefore, for any changes in κ_{Bottom} to have a visible effect on the Q-factor, the value of κ_{Top} has to be comparable. This is why increasing the number of bottom pairs has no effect at < 9 top pairs, but going from 15.5 to 20.5 pairs on the bottom triples the Q-factor at 15 top pairs.

The Purcell enhancement depends not just on the containment in time, but also on how localized around the source the field energy is, quantified by the mode volume. Looking at the changes to V_{Mode} [4] in Fig. 5.4(b), we can see that within this range adding more top pairs increases the volume, while adding bottom pairs has an effect up until a certain point. This is because by adding each DBR layer, we increase both

[4]The mode volume is calculated with Eq.(2.20), such that the values of F_P and Q are obtained with the FDTD method, and V_{mode} is worked out algebraically from that.

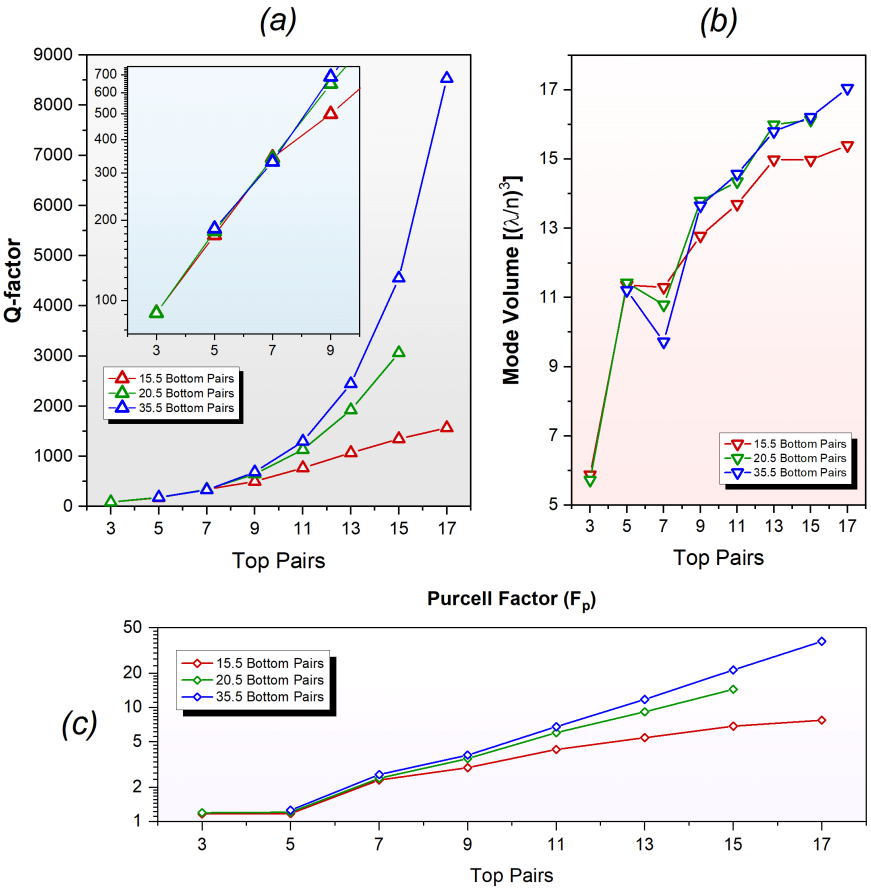

Figure 5.4: *The effects that changing the number of layers in the top and bottom DBRs has on the (a) Q-factor and (b) Mode volume, as well as the resulting (c) Purcell factor.*

the reflectivity of the stack and the physical region where the Bloch waves can exist. If there are fewer DBR layers on the top, for instance, the field is emitted through the boundary and in free space, it isn't a Bloch wave but a propagating wave. Therefore, as long as we add more DBR layers, we increase the mode volume until we're adding dielectric material in a region where the Bloch wave will be undetectably small. This is why adding more pairs on the top increases the mode volume, as the E-field can still be influenced 17x of our GaAs/AlAs pairs away from the cavity. Because of this we also see a slight increase V_{Mode} when increasing from 15.5 to 20.5 bottom DBR pairs, but no increase when going from 20.5 to 35.5 pairs - an increment three times in size with none of the same effects. I tested this observation by recording the electric field flux through a planar slice which bisecting the pillar lengthwise, and performing a Fourier transform on the results to isolate $|E|$ at 1300nm. These results are shown in Fig. 5.5.

The E-field barely penetrates past a certain distance away from the cavity, which is why adding further layers does not increase the mode volume, as the source cannot

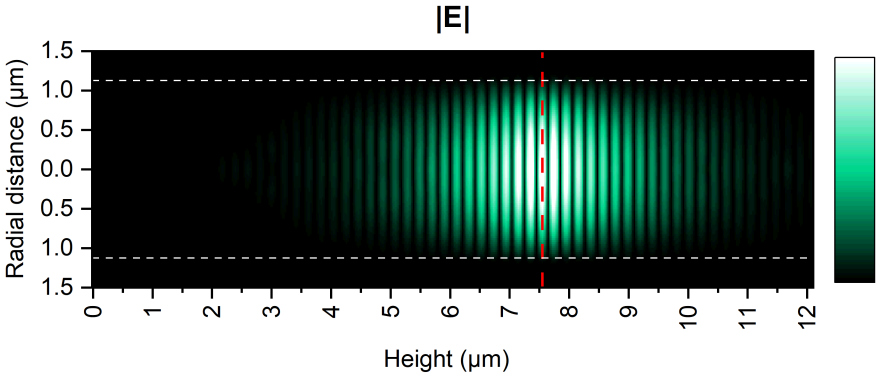

Figure 5.5: *The normalised magnitude of the E-field at 1300nm in and around a 13x/35.5x micropillar. The white dashed lines mark the lateral edges of the pillar, while the red one is located along the horizontal middle of the cavity layer.*

"see" these additional layers. Conversely to our range of bottom pairs, the top pairs remain below 17 pairs, where the E-field around the source is affected by the changes, which affects the local density of states and changes the Purcell enhancement.

It would therefore be reasonable to expect that as adding more layers increases the Q-factor exponentially, but V_{Mode} increases asymptotically, the Purcell factor would scale primarily with the Q-factor when changing the number of top and bottom DBR layers at a constant pillar diameter $d = 2.25$ μm. This is what we observe in Fig. 5.4c where differences between the Purcell factors of each coloured set of measurements are insignificant when the top DBR is made up of few pairs, but become noticable at properly formed cavities at > 9 top DBR pairs.

What this all shows is that while the diameter determines how easily we can couple to the cavity at the same Purcell factor, by changing the number of DBR layers with which the quantum dot is bound we can control how strongly we enhance the spontaneous emission through the Purcell effect, and consequently, how strongly the source-cavity coupling is. To examine this further, we record two values of the active coupling β, for reasons which become obvious further below. This includes the calculated value of the β-factor which has been used so far and is defined in Chapter 2, but also the β^* estimation discussed in the Chapter 2, which is a Purcell-factor based value of the active coupling which makes the assumption of $\Omega_V \gg \Omega_C$. These values have been shown for the DBR pair variations in Fig. 5.6 below.

The calculated β-factor shows that adding more top or bottom layers increases the active coupling to the cavity. Furthermore, changes in β are similar to the changes in the Q-factor where $\Delta\beta$ is considerably larger when increasing the top pairs than when

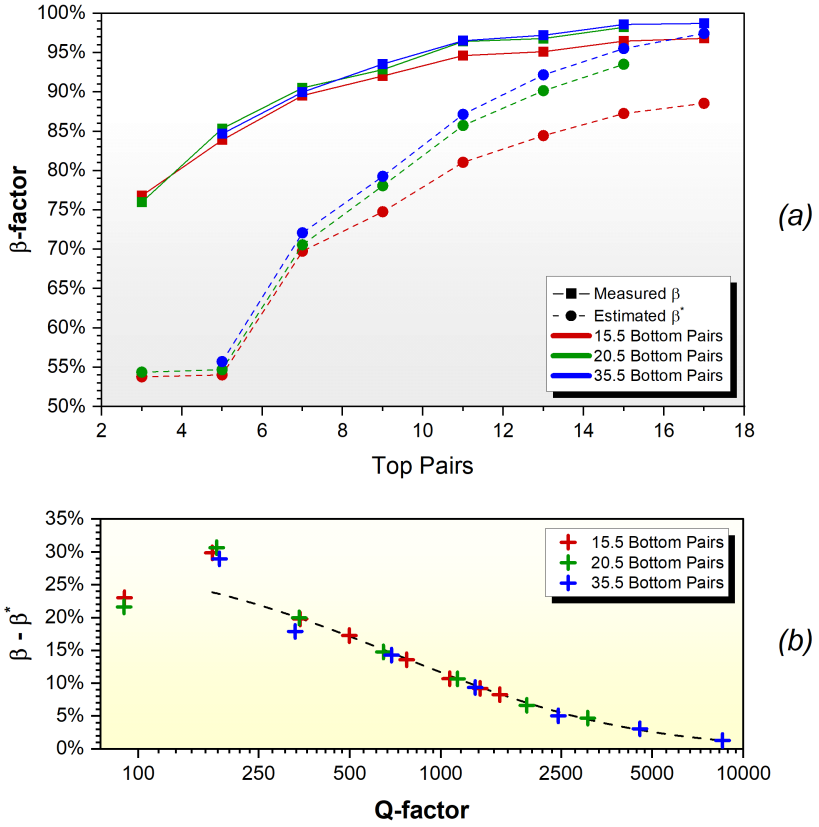

Figure 5.6: *(a) Calculated values for β using the power transmission method as opposed to the Purcell-factor based estimation β^* for various DBR pillar structures. (b) The disparity between the simulated and estimated active coupling as a function of Q-factor, where the dashed line is representative of the trend (as opposed to a fit of any mathematical significance).*

going from 20.5 to 35.5 bottom DBR pairs. This also is in agreement with previous research on the topic, as higher values of the Q-factor result in larger Γ_{Cavity}, meaning a higher F_P. This then results in a stronger β-factor, depending on how easily the Purcell enhancement translates to cavity coupling, i.e. $\Delta F_P/\Delta\beta$.

Another feature which can also be seen is that the β-factor is quite high, even for pillars where the top DBR is barely there (meaning that the system experiences barely any Purcell enhancement); for instance the 5x/35.5x pillar has a Q-factor of around 200 ($F_P \approx 2.5$) and a corresponding $\beta = 85\%$. Conversely to this, the Purcell-factor based estimation β^* predics weaker active coupling such that the difference between approximation and simulation is dependent on the size of the pillar. In other words, the smaller pillars which correspond to lower Q-values (as seen in Fig. 5.4(a)) show significantly stronger coupling to the cavity than previously estimated. In fact, by mapping the difference $\beta - \beta^*$ as a function of the Q-factor like in Fig. 5.6(b), it can be shown that the difference isn't dependent on the number of DBR layers per se, but on

the Q-factor resulting from the pillar structure.

This difference shows that some previous assumptions that the β-factor of micropillars can be estimated with β^* is incorrect, but insignificatnly so if the $Q > 5000$. At pillars with a lower Q-factor than this, the error in β is more than a few percent, and this results in the incorrect conclusion that high-β low-Q pillars cannot exist. This is because the value of Ω_C/Ω_V, which affects the cavity coupling efficiency $\Delta F_P/\Delta\beta$ is a lot better for the micropillars than for atoms, and we cannot estimate $\Omega_V \gg \Omega_C$ which leads to Eq.(2.23) being non-valid for low-Q micropillars. We can further explore this by plotting both β and β^* as functions of the Q-factor, which has been shown in Fig. 5.7.

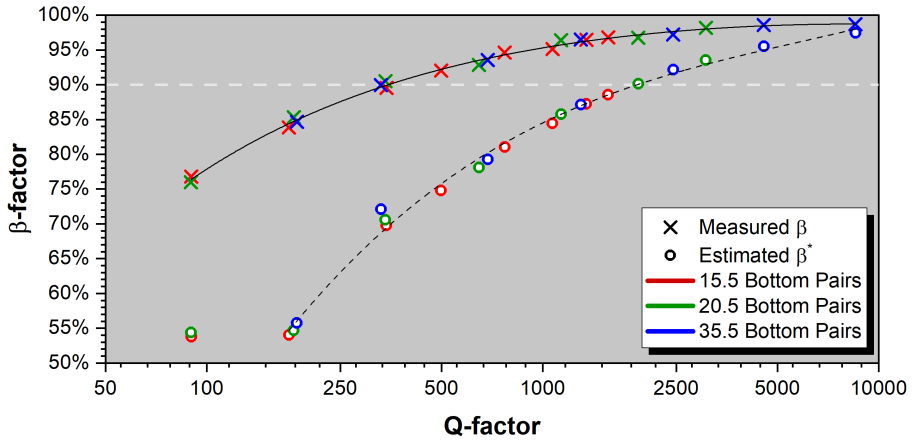

Figure 5.7: *The effects of the Q-factor on the active coupling to the cavity, where the Q-factor is shown on a logarithmically scaled axis.*

By showing the data points in separate colours, depending on the number of bottom DBR pairs, we see that the β-factor indeed depends on the Q-factor rather than on the the non-natural top/bottom pairs parameter. Furthermore, we can see that the calculated value of β is much higher than the estimated one at any given value of Q, owing to the larger[5] cavity mode Ω_C. Because the β^* estimation relies on atomic rather than pillar geomertry, we see that it inaccurately predicts that only high-Q values can result in high-β. Considering $\beta > 90\%$ to signify strong active coupling, we see that whereas β^* estimates that a Q-factor of 2000 is needed at this diameter (meaning at this value of Ω_C/Ω_V), whereas the calculated β-factor which doesn't rely on assumptions shows that strong coupling can be achieved with Q-factors on the order of 10^2 (≈ 330).

What we can conclude from Fig. 5.7 is that if we look at more accurate calculations of the β-factor, it is entirely possible to get pillars which have weak Purcell enhancement

[5]Larger here is taken to mean "with bigger cavity solid angle", not to signify the resonator volume V_{Mode}

but display strong active coupling to the cavity mode. Furthermore, by increasing the number of DBR layers, we increase the energy confinement of the cavity (Q-factor), and the larger F_P results in a bigger β-factor. However, none of this takes into account what happens to the light once it's coupled into the cavity, which I examine in the next section by looking at the passive effiency.

5.4 Passive Efficiency (η) Optimisation

So far I have shown that due to cavity QED effects, higher numbers of DBR pairs result in stronger coupling β. However, there are additional effects which aren't taken into account in the Purcell enhancement calculations, such as the changing reflectivity and transmissivity of the top and bottom DBR stacks. While we've looked at these effects partially through the decay rate κ, observed indirectly though the Q-factor, we've only looked at the total decay of the cavity energy regardless of direction. Therefore, the β-factor on it's own provides an incomplete picture, which is why the passive efficiency, or η-factor, is a metric of interest. I calculated the passive efficiency of the simulated pillars where the top and bottom DBR pairs are varied (previously used in the β-factor optimisation), and have shown the results in Fig. 5.8(a) below.

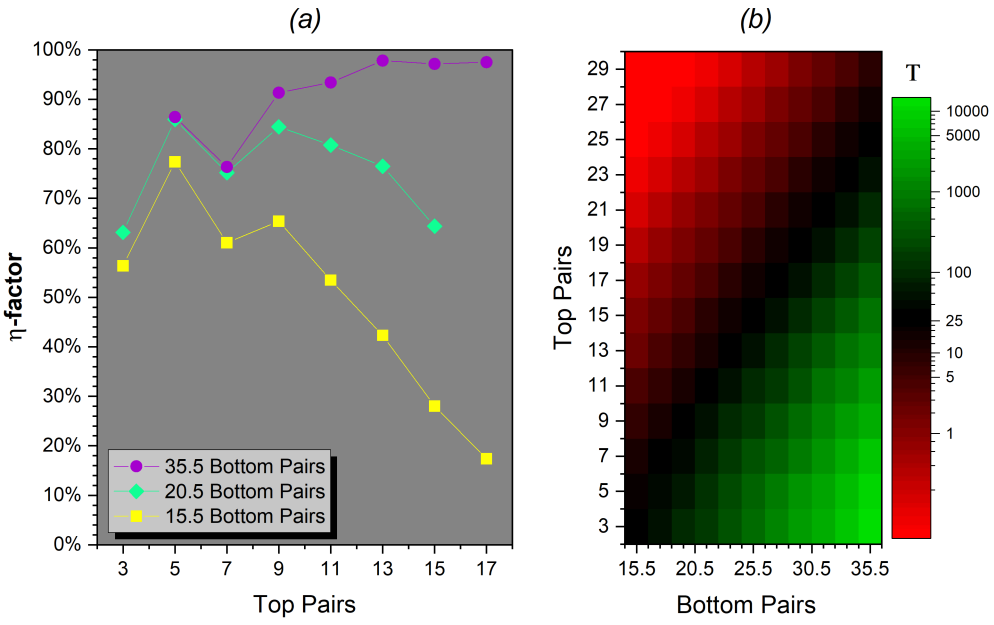

Figure 5.8: *(a) The passive efficiency for the three top DBR layer variations. Data obtained with the FDTD method; (b) The ratio of the transmissivity of the top and bottom DBR stacks that comprise the micropilars, calculated with the transfer matrix method.*

By looking at the eta values of each pillar set, organised by colour in Fig. 5.8(a), we can identify regions where adding more layers on the top DBR increases the passive

efficiency i.e. the η-factor and regions where further layers have a harmful effect on η. This presents optimal points of η depending on the amount of layers in the bottom stack, such that lower numbers of bottom DBR pairs correspond to peaks in η which occur at fewer top pairs. One strange consequence of this is that at very large bottom stacks (35.5x), we see that increasing the number of pairs on top from 9x to 15x results in a net increase in the passive efficiency, even though the reflectivity of the top stack (as calculated by TMM) is significantly increased, as shown in Fig. 5.9.

Top DBR Pairs	**Reflectivity**	**Transmissivity**
9x	76.5%	23.5%
15x	96.1%	3.9%
Δ	+19.6%	-19.6%

Figure 5.9: Reflectivity and transmissivity of GaAs/AlAs DBR stacks, as calculated by the transfer matrix method.

To explain the otherwise absurd effect of the transmission through the top DBR increasing despite the transmissivity decreasing by almost 20%, we cannot only consider the change in transmissivity of only one pillar DBR stack. As the field that's coupled to the cavity mode has to decay *somewhere*, to explain the η-factor we must consider the ratio of the transmissivity between the top and bottom DBR stacks, which I have defined (for convenience) as

$$\mathrm{T} = \frac{|t_{TopDBR}|^2}{|t_{BotDBR}|^2} \tag{5.2}$$

where t denotes the transmittance of each DBR. We can then look at T as a function of top and bottom pairs, which I have shown in Fig. 5.8(b). Approximately when T is > 20, the effect of adding more pairs is positive as the top stack remains about an order of magnitude more transmissive than the bottom. As the cavity-coupled field has to decay through either of these two directions, we still observe a high passive efficiency because the top direction remains significantly more favourable/transmissive. While an exact "turnover" point is difficult to determine with only 3 data points, I have estimated the regions where the value of T signifies that adding further pairs on top has a positive or negative effect where a black line set at $\mathrm{T} \approx 20$ estimates the turnover point for each value of bottom DBR pairs. This also makes an implicit assumption that the turnover point has a linear relationship with the amount of bottom pairs, which might not be accurate. This seems irrelevant however, as we can see that for 35.5x bottom pairs, $\mathrm{T} \approx 350$ which is still significant enough to mean that reduced values of T will not contribute to reduced values in the η-factor at 35.5x bottom pairs when the number of top pairs ≤ 17. It should be noted that the turnover point does not

occur at T $\approx$ 1, due to the fact that while the top DBR is terminated at a GaAs-air boundary (high-low refractive index), the bottom stack is made up for an extra layer of AlAs and rests on a GaAs substrate, meaning that the edge of the micropillar sits on an AlAs-GaAs boundary (low-high refractive index). The refractive properties of the dielectrics therefore create a quantum well at the bottom of the pillar (compared to the top) which means that the point at which the field decays equally through the top and bottom part of the cavity occurs at T $>$ 1.

What I have shown so far is that the adding more layers on the top DBR has the effect of increasing the β-factor by more strongly coupling to the cavity mode as a result of the increased Q-factor, and either a positive or negative effect on the η-factor depending on the relative transmissivity between the top and bottom DBR stacks. The internal efficiency, which combines the effects of the active coupling to and passive efficiency of the cavity, is therefore expected to increase as more top DBR pairs are added, until some point where T $\approx 10^1$ and ξ starts to decrease. Since the goal is to determine the theoretical possibility of low-Q pillar with large internal efficiency, it's helpful to show how ξ changes with the Q-factor, a physical value, rather than the number of top or bottom pairs, a structural parameter; this has been shown in Fig. 5.10.

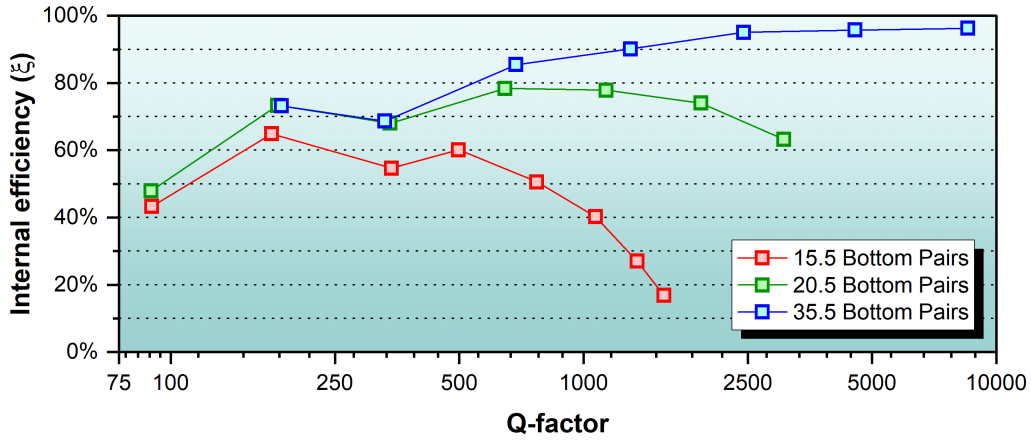

Figure 5.10: *The internal efficiency of the DBR layers variations, plotted as a function of the Q-factor.*

What Fig. 5.10 reveals is that at sufficiently large bottom DBR stacks (35.5x pairs) it is possible to obtain theoretical values of the internal efficiency ξ above 90% at Q-factors as low as 1300. The trend suggests that whether adding more DBR layers has a positive or negative effect on ξ, as well as the magnitude of this effect, depends on the relative values of the top and bottom DBR pairs. For instance, going from a 7x/15.5x to a 9x/15.5x pillar increases ξ by 5%, whereas increasing the bottom pairs to 7x/20.5x

would've increased ξ by $> 15\%$. Conversely, a 3x/15.5x pillar would benefit significantly more from adding 2 top layers than from 5 additional bottom pairs. Regardless of the ambiguity of whether adding more pairs is optimal, we can conclude that high internal efficiencies[6] can be obtained for Q-factor values on the order of 10^2.

While this shows the possibilty of low-Q pillars with strong coupling to the cavity, and therefore a high internal efficiency, as well as the possibility of minimising the Q-factor with negligiblle losses to ξ, it doesn't fully answer the question of how applicable these devices can theoretically be. The β-factor quantifies how likely a photon created in the quantum dot is to couple into the cavity mode, and the η-factor describes the probability that a photon within the cavity will decay through the top; as such, the ξ-factor represents the proportion of photons which will be emitted through the top of the pillar structure. What the internal efficiency doesn't describe is the angular distributuion of the emission, or rather, how efficiently will the emissionthrough the top be collected in the far field.

To take this into account, I calculated the collection efficiency as the proportion of the emitted field which is captured within a solid angle of 2Θ, as described in further detail in the Chapter 3, and analogous to the process used in the Tamms results chapters. By multiplying the collection with the internal efficiency, we obtain the total efficiency, which is the likelihood of a trigger resulting in a single photon emitted and collected from the system as a function of numerical aperture. The total efficiency for the only set of pillars (35.5x bottom DBR pairs) I examined which could reach high ($> 80\%$) internal efficiency ξ is presented in Fig. 5.11

Upon inspection it can be concluded that due to a low ξ, the 5x and 7x top pair pillars can be eliminated because even at NA=1, meaining a full collection over $2\theta = 2\pi$, the total efficiency $\leq 80\%$. At such small DBR stacks, despite the high transmissiveness of the top DBR, the decay rate κ is too large, meaning that even at favourable values of Ω_C/Ω_V, the overall enhancement due to the low Q-factor provides insufficient active coupling to the cavity. On the other hand, we can see that when the top DBR has > 11 pairs, significant proportions of the photons emitted by the quantum dot can be extracted.As shown by the dashed grey lines in the smaller window of Fig. 5.11, within an NA=0.45, which can reaonably be reached by bullk optics, four of the largest pillars considered (having 17x-11x top pairs and 35.5x bottom pairs) have a total efficiency $\geq 80\%$. Looking at the Q-factors of these micropillars in Fig. 5.4(a), we can see that the pillars with 11x and 13x top pairs have corresponding Q-factors of 1300 and 2450, respectively. It can be concluded that the results in Fig. 5.11 show the theoretical

[6]Here we assume a high internal efficiency to mean $\xi > 80\%$.

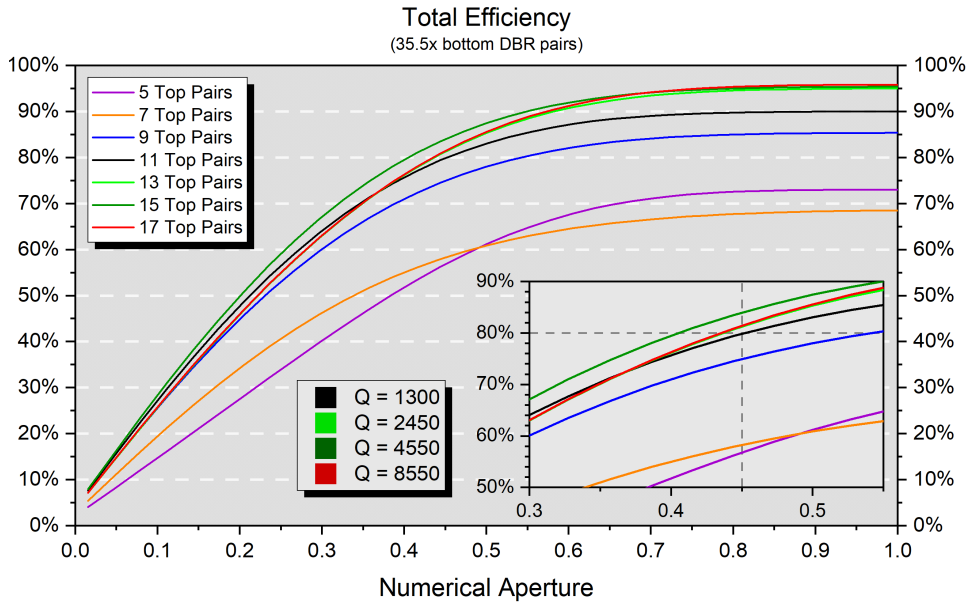

Figure 5.11: *The total extraction efficiency of the 35.5x bottom DBR pillars as a function of numerical aperture. The Q-factors of pillars which have a total efficiency* $> 80\%$ *within an NA=0.45 are also shown.*

possibility of micropillars with a high brightness at reasonable collection NAs at Q-factors in the low thousands, with better optimisations on the pillar diameters possibly yielding lower Q-factors while conserving brightness.

5.5 Obtaining high β-factor at low F_P

If we observe the effects of the pillar diameter on the β-factor shown in Fig. 5.2(a), we notice that there are notable variations in the active coupling which don't correspond to changes in the Q-factor or Purcell factor F_P, as seen in Fig. 5.2(b). This observation does not follow the conventional reasoning where "larger β-factor" is often taken to necessitate a larger Q-factor. I present a possible explanation for these observations in the cavity QED in terms of the discussion in Section 2.2.2. It is important to mention, however, that because there are data points for only a small range of radii (and only 2 different Q-factors) this is more of an observation and discussion on further work.

Changing the diameter does not affect the Q-factor significantly, only the β-factor; this is a result of the increased side losses. Previous work has shown that these fluctuations occur with a period of λ/n_{GaAs} [68], as placing the radial edge of the micropillar at nodes in a standing wave results in less of the E-field being transmitted radially out as T_{Sides}. For the pillars simulated in this thesis, this works out to be $\frac{1300\text{nm}}{n_{GaAs}} \approx 381$ nm, and the peaks relevant to Fig. 5.2(a) occur at $D = 381 \times 5 = 1905$ nm and

$381 \times 6 = 2286$ nm[7].

Because this effect seems to be independent from the Q-factor, and consequentially from the Purcell enhancement (F_P); additionally, it affects the β-factor by changing the side leakage. We can therefore think of the diameter as changing not the Q-factor, but the efficiency with which Purcell enhancement translates to active coupling in the micropillar, described by $\frac{\Delta\beta}{\Delta F_P}$. In section 2.2.2 I talked about how the larger cavity solid angle makes the β^* estimation of F_P (Eq.(2.23)) invalid because it reduces the amount of Purcell enhancement needed to achieve a certian β-factor; similarly, the choice of radius can further optimise the micropillar in this fashion, meaning that for a given increase in the Purcell enhancement ΔF_P, $\Delta\beta$ would be greater if the pillar diameter is "optimal" (i.e. at values of $k \times \frac{\lambda}{n_{GaAs}}$ where $k \in \mathbb{N}$). I show evidence of this by looking at the difference in β for the two pillars examined in Fig. 5.2 at each diameter, and compare it to the difference in the Purcell factor as a rough, linear estimation of $\Delta F_P/\Delta\beta$, which is presented in Fig. 5.12.

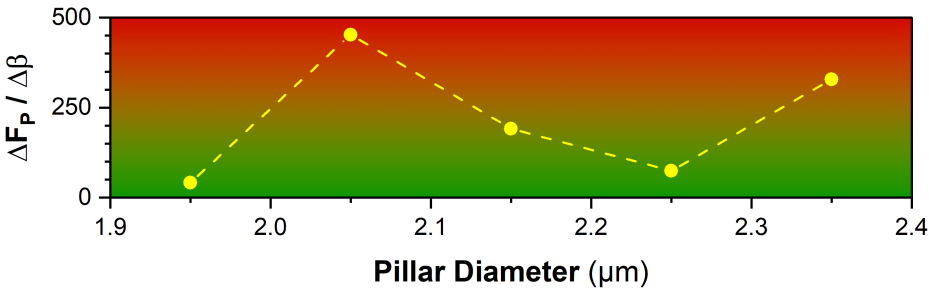

Figure 5.12: *A linear estimation of $\Delta F_P/\Delta\beta$ of the data represented in Fig. 5.2(a), where the differences in Purcell factor (F_P) and β is between the large and small pillars (i.e. the 13x/35.5x pillar data displayed in orange, and the 7x/35.5x pillar data displayed in purple. The background colour represents the optimisation, as the green area depicts diameters where a significantly smaller increase in F_P results in the same increase in β. Data obtained with FDTD.*

What we can see in Fig. 5.12 is that at pillar diameter corresponding to peaks in the β-factor (Fig. 5.2(a)) we observe significantly lower $\Delta F_P/\Delta\beta$. This is also the reason behind the fixed-Q changing-β seen in Fig. 5.2(b) - while we aren't changing the Purcell/Q-factor (or "how much enhancement is **experienced** by the emitter"), we *are* changing how effectively the Purcell enhancement couples the emitter to the cavity modes (or "how much enchancement is **required** to couple the emitter well to the cavity"). The possibility of having two pillars where one has a lower Q-factor, but a higher β-factor (shown in Fig. 5.2(b)) is explaind by this. In fact we can see one

[7]The center of the pillar, where the QD sits, would be an antinode, meaning that nodes would be (radially) half a wavelength away, making the diameters which terminate the pillar at nodes equal to $k \times \frac{\lambda}{n_{GaAs}}$ where $k \in \mathbb{N}$

instance of this in Fig. 5.13 below.

DBR Pairs	**Diameter**	**Q-factor**	β
7x/35.5x	1.95 μm	≈350	96%
13x/35.5x	2.05 μm	≈2400	92%

Figure 5.13: Selected values from Fig. 5.2(a)

It's important to keep in mind that Fig. 5.12 is a linear estimation resulting from 2 pillars (calculations at 2 different Q-factors) at 5 different pillar diameters; as such, more data points and further work would be needed to present a complete examination of how the pillar diameter affects the cavity quantum electrodynamics of the micropillar.

5.6 Conclusions

By simulating several pillars at different diameters, as well as identical simulations for a pillar with a stronger Purcell enhancement, I was able to measure the active coupling β (Fig. 5.2) and observe some of the effects anticipated by the discussion in the Chapter 2. What I found was that the pillar diameter had almost no effect on the Q-factor, but considerably affected the β-factor; this led to the conclusion that the pillar diameter can be optimised prior to changing the amount of top and bottom DBR pairs. For the materials used in these simulations (described in section **??**) and $\lambda = 1300$ nm, I chose the optimal diameter $D = 2.25$ μm.

I then continued by changing the number of DBR pairs which make up the top and bottom stacks, and discussed the effects this had on the Purcell enhancement, as well as the related values of the Q-factor and mode volume (Fig. 5.4). Simulation data showed the exponential scaling of the Q-factor due to the increased reflectivity of the DBRs, as well as an approximately linear growth of the mode volume due to the additional radial thickness of the micropillar within a range where the cavity E-field is a non-negligible value. This was followed by calculations of the passive efficiency for the pillars at the optimal diameter but various numbers of DBR pairs on top and bottom of the cavity. I found that high η-factors can be reached despite significant increases in the reflectivity of the top DBR stack, as long as the reflectivity of the bottom one is at least 1-2 orders of magnitude higher(Fig. 5.8). Since increases in either top or bottom layers result in stronger coupling to the cavity, i.e. a greater β-factor, and proportional increases in both top and bottom pairs result in a higher passive efficiency, i.e. a larger η-factor, it is entirely possible to obtain near unity brightness. However, notwithstanding the

issue that each additional layer increases the difficulty and cost of growth and fabrication, this also increases the Q-factor significantly, leading to lower device yields. It is therefore helpful to show the internal efficiency against the Q-factors of each pillar (Fig. 5.10), which showed that it is possible to get $\xi > 80\%$ at $Q < 1000$.

I also considered the angular distribution of the emission far-field, and used it to calculate the total extraction efficiency (of the devices for the pillar set with the largest number of bottom pairs, 35.5x. While it's demonstrably impossibleto obtain an adequately bright SPS with some micropillars regardless of collection efficiency due of significant losses to the vaccum modes and emission into the substrate (5x-7x pairs), I found that total efficiencies $> 80\%$ are possible within an NA ≥ 0.45 for pillars with Q-factors ≥ 1300. Alternatively, it's possible to get an equivalent brightness at NA $\approx$ 0.4, but Q = 8550; conversely, one could consider a much lower Q-factor structure (Q = 690), but at a significantly wider collection angle (NA = 0.55). It can be concluded that high brightness low-Q pillars with a variety of properites can be demonstrated. The simulation of micropillars in both a low and high Q-factor regime which have a sufficient brightness ($> 85\%$) to serve as a veritable SPS demonstrates that a scalable solution for generating single photons is plausible.

Finally, I presented a short discussion of how the pillar diameter affects the β factor while keeping the Q-factor constant. I showed how the $\Delta F_P/\Delta\beta$ ratio is minimised when the pillar diameter is set at values of λ/n_{GaAs}, corresponding to the optimal radii found in the β-factor optimisation earlier in the chapter. However, due to the low number of data points involved, I suggest that further work is needed for a more conclusive investigation into the structural effects on the quantum electrodynamics and the resulting pillar brightness.

Appendix A: Jaynes-Cummings Hamiltonian

To begin, we imagine a two level emitter with transition frequency $\nu = \frac{E}{\hbar}$ where $|x\rangle$ is the excited, and $|g\rangle$ the ground state. Ignoring excitation of other cavity modes[8], this two level system coupled to a single cavity mode has the Hamiltonian

$$H = H_e + H_f + H_i \tag{3}$$

where H_e and H_f are the emitter and field Hamiltonians respectively, while H_i describes the interaction between the emitter and the field surrounding it.

Starting with the Hamiltonian of the emitter, we remember that the states $|g\rangle, |e\rangle$ form the basis of the emitter, meaning $|e\rangle\langle e| + |g\rangle\langle g| = 1$. It can also be said that $|g\rangle, |e\rangle$ form a complete set of eigenstates for the emitter energy such that the corresponding eigenvalues are $-\frac{\hbar\nu}{2}$ and $\frac{\hbar\nu}{2}$, respectively. We can therefore write H_e as

$$H_e = \frac{\hbar\nu}{2}\sigma_z \tag{4}$$

where σ_z is the population operator $\sigma_z = |e\rangle\langle e| - |g\rangle\langle g|$.

Formulating the field Hamiltonian is fairly straightforward, as the field eigenstates are Fock states $|n\rangle$ with eigenvalues $\hbar\omega\left(n + \frac{1}{2}\right)$. By using the photon creation ($a^\dagger$) and anihilation (a) operators, we can represent the field Hamiltonian as

$$H_f = \hbar\omega\left(a^\dagger a + \frac{1}{2}\right) \tag{5}$$

We represent the interaction Hamiltonian as a semi-classical dipole approximation

$$H_i = -\vec{d}\cdot\vec{E} \tag{6}$$

where for a given position of the j-th electron $\vec{r}_j$, the classical dipole moment is given by $\vec{d} = \sum_j e\vec{r}_j$. Very similarly to how in a single electron atom $\vec{r}$ represents the relative position of the electron to the nucleus, in the quantum dot $\vec{r}$ could be thought of as the relative "distance" between the hole and electron within the exciton. To formalise this

[8] Assuming we're close to the fundamental optical mode ω

quantum-mechanically, we begin by applying the unity operator $\mathbb{1} = |e\rangle\langle e| + |g\rangle\langle g|$ to the dipole moment to obtain

$$e\vec{r} = \mathbb{1}\ e\vec{r}\ \mathbb{1} = \Big(|e\rangle\langle e| + |g\rangle\langle g|\Big)\ e\vec{r}\ \Big(|e\rangle\langle e| + |g\rangle\langle g|\Big) \tag{7}$$

This can be simplified with the introduction of atomic transition operators $\sigma_{ij} = |i\rangle\langle j|$ and the dipole moment matrix $\vec{\mu}_{ij} = \langle i|\, e\vec{r}\,|j\rangle$. By labeling the transition operators as $\sigma_+ = \sigma_{eg} = |e\rangle\langle g|$ and $\sigma_- = \sigma_{ge} = |g\rangle\langle e|$, we can write

$$e\vec{r} = \vec{\mu}_{ee}\sigma_{ee} + \vec{\mu}_{eg}\sigma_{eg} + \vec{\mu}_{ge}\sigma_{ge} + \vec{\mu}_{gg}\sigma_{gg} \tag{8}$$

The next step of making H_i quantum mechanical is to formulate $\vec{E}$ by using the electric field operator

$$\vec{E}(\vec{r}) = i\sqrt{\frac{\hbar\omega}{2V_{mode}\cdot \mathrm{Max}\left(\varepsilon(\vec{r})\left|\vec{E}(\vec{r})\right|^2\right)}}\hat{e}\left(E(\vec{r_E})a - E^*(\vec{r_E})a^\dagger\right) \tag{9}$$

In this expression, $\hat{e}$ stands for the electric field direction at point $\vec{r}_e$ of the emitter; $a, a^\dagger$ are the anihilation and creation operators for the cavity, $E(\vec{r}_e)$ is the classical field, and the mode volume V_{mode} is given by

$$V_{mode} = \frac{\iiint \varepsilon(\vec{r})\left|\vec{E}(\vec{r})\right|^2 d^3\vec{r}}{\varepsilon_M\left|\vec{E}(\vec{r}_M)\right|^2} \tag{10}$$

such that the point of maximum field density is labeled as $\vec{r}_M$, with a corresponding dielectric constant $\varepsilon_M = \varepsilon(\vec{r}_M)$.

We can now write out the quantum mechanical formulation of the interaction Hamiltonian in Eq.(13) as

$$H_i = -i\sqrt{\frac{\hbar\omega}{2V_{mode}\cdot \mathrm{Max}\left(\varepsilon(\vec{r})\left|\vec{E}(\vec{r})\right|^2\right)}}\times$$
$$(\vec{\mu}_{ee}\cdot\hat{e}\sigma_{ee} + \vec{\mu}_{eg}\cdot\hat{e}\sigma_{eg} + \vec{\mu}_{ge}\cdot\hat{e}\sigma_{ge} + \vec{\mu}_{gg}\cdot\hat{e}\sigma_{gg})\times$$
$$\left(E(\vec{r}_E)a - E^*(\vec{r}_E)a^\dagger\right) \tag{11}$$

We begin simplifying by noting that $\vec{\mu}_{eg} = \vec{\mu}^*_{ge}$ and $||=||$ follow from the parity[9] condition that for any $|i\rangle$, $\vec{\mu}_{ii} = \langle i|\, e\vec{r}\,|i\rangle = e\langle i|\,\vec{r}\,|i\rangle = 0$; As such, the second and third

[9]Position operator is an odd function

terms of H_i become

$$H_i = \dots \left(\vec{\mu}_{ee} \cdot \hat{e}E(\vec{r}_E)\sigma_+ a + \vec{\mu}^*_{eg} \cdot \hat{e}E(\vec{r}_E)\sigma_- a \; + \right. \\ \left. \vec{\mu}_{eg} \cdot \hat{e}E^*(\vec{r}_E)\sigma_+ a^\dagger - \vec{\mu}^*_{eg} \cdot \hat{e}E^*(\vec{r}_E)\sigma_- a^\dagger \right) \quad (12)$$

Due to the fact that the terms including $\sigma_- a$ and $sigma_+ a^\dagger$ are not energy conserving, we can remove them from the expression. The interaction Hamiltonian can then be expressed as

$$H_i = i\hbar \left(g^*(\vec{r}_E) a^\dagger \sigma_- - g(\vec{r}_E)\sigma_+ a \right) \quad (13)$$

where $g(\vec{r})$, called the emitter-field coupling parameter, is defined as

$$g(\vec{r}_E) = \frac{1}{\hbar} \sqrt{\frac{\hbar\omega}{2V_{mode} \cdot \mathrm{Max}\left(\varepsilon(\vec{r}) \left| \vec{E}(\vec{r}) \right|^2 \right)}} \vec{\mu}_{eg} \cdot \hat{e}E(\vec{r}_E) \quad (14)$$

This coupling parameter can be expressed in a more physically interpretable form; we re-arrange the terms in $g(\vec{r}_E)$ which have dependence on position-, polarization-, or neither in groups such that we can label the following terms:

$$g_0 = \frac{\mu_{eg}}{\hbar} \sqrt{\frac{\hbar\omega}{2\varepsilon_M V_{mode}}} \quad (15)$$

$$\psi(\vec{r}_E) = \frac{E(\vec{r}_E)}{|E(\vec{r}_M)|} \quad (16)$$

$$\cos(\zeta) = \frac{\vec{\mu}_{eg} \cdot \hat{e}}{\mu_{eg}} \quad (17)$$

where g_0 is the Rabi frequency, and $\mu_{eg} = |\vec{\mu}_{eg}|$. As such, we can then express the coupling parameter more conveniently as

$$g(\vec{r}_E) = g_0 \psi(\vec{r}_E) \cos(\zeta) \quad (18)$$

From Eq.(18) we can make several observations about the QED properties of the emitter-cavity system. Firstly, we observe that the maximum of the position dependent $\psi(\vec{r}_E)$ occurs when the emitter is located at $\vec{r}_M$, where the electric field energy density is at it's peak. We can further deduce that in order to maximise the coupling parameter, the dipole moment should be orthogonal to the electric field direction due to the $\cos(\zeta)$) term. Finally, the g_0 term shows that $g(\vec{r}_E) \propto V_{mode}^{-\frac{1}{2}}$, indicating an inverse relationship between mode volume and coupling to the resonant cavity.

With expressions for the emitter Hamiltonian H_e in Eq.(4), the field Hamiltonian H_f in Eq.(5), and the interaction Hamiltonian H_i in Eq.(13), we have arrived at the Jaynes-Cummings Hamiltonian for a lossless emitter-field system:

$$H = \frac{\hbar\nu}{2}\sigma_z + \hbar\omega\left(a^\dagger a + \frac{1}{2}\right) + i\hbar\left(g^*(\vec{r}_E)a^\dagger\sigma_- - g(\vec{r}_E)\sigma_+ a\right) \tag{19}$$

Bibliography

[1] P. Sekatski, N. Sangouard, F. Bussieres, C. Clausen, N. Gisin, and H. Zbinden. Detector imperfections in photon-pair source characterization. *J. Phys. B: At. Mol. Opt. Phys. 45, 124016*, Sep 2011.

[2] E Knill, R Laflamme, and GJ Milburn. A scheme for efficient quantum computation with linear optics. *Nature*, 409(6816):46–52, January 2001.

[3] Vittorio Giovannetti, Seth Lloyd, and Lorenzo Maccone. Quantum-enhanced measurements: Beating the standard quantum limit. *Science*, 306(5700):1330–1336, 2004.

[4] M. Kaliteevski, I. Iorsh, S. Brand, R. A. Abram, J. M. Chamberlain, A. V. Kavokin, and I. A. Shelykh. Tamm plasmon-polaritons: Possible electromagnetic states at the interface of a metal and a dielectric bragg mirror. *Phys. Rev. B*, 76:165415, Oct 2007.

[5] Dmitry I. Yakubovsky, Aleksey V. Arsenin, Yury V. Stebunov, Dmitry Yu. Fedyanin, and Valentyn S. Volkov. Optical constants and structural properties of thin gold films. *Opt. Express*, 25(21):25574–25587, Oct 2017.

[6] N Ahmad, J Stokes, Neil A Fox, M Teng, and MJ Cryan. Ultra-thin metal films for enhanced solar absorption. *Nano Energy*, 1(6):777–782, 2012.

[7] O. Gazzano, S. Michaelis De Vasconcellos, C. Arnold, A. Nowak, E. Galopin, I. Sagnes, L. Lanco, A. Lemaître, and P. Senellart. Bright solid-state sources of indistinguishable single photons. *Nature Communications*, 4(1), 2013.

[8] Xing Ding, Yu He, Z.-C. Duan, Niels Gregersen, M.-C. Chen, S. Unsleber, S. Maier, Christian Schneider, Martin Kamp, Sven Höfling, Chao-Yang Lu, and Jian-Wei Pan. On-demand single photons with high extraction efficiency and near-unity indistinguishability from a resonantly driven quantum dot in a micropillar. *Phys. Rev. Lett.*, 116:020401, Jan 2016.

[9] Lumerical Solutions Inc. (https://www.lumerical.com/products/fdtd/).

[10] M Planck. Über eine verbesserung der wienschen spektralgleichung. *Verhandlungen der Deutschen Physikalischen Gesellschaft*, 2:202–204, 1900.

[11] Rodney Loudon. *The quantum theory of light*. Oxford University Press, 2010.

[12] Paul A. M. Dirac. *The principles of quantum mechanics*. Clarendon Press, 2010.

[13] Mohsen Razavy. *Quantum theory of tunneling*. World Scientific, 2003.

[14] E. Schrödinger. Discussion of probability relations between separated systems. *Mathematical Proceedings of the Cambridge Philosophical Society*, 31(4):555–563, 1935.

[15] S. Al-Kathiri, W. Al-Khateeb, M. Hafizulfika, M. R. Wahiddin, and S. Saharudin. Characterization of mean photon number for key distribution system using faint laser. In *2008 International Conference on Computer and Communication Engineering*, pages 1237–1242, 2008.

[16] M. D. Eisaman, J. Fan, A. Migdall, and S. V. Polyakov. Invited review article: Single-photon sources and detectors. *Review of Scientific Instruments*, 82(7):071101, 2011.

[17] Alessandra Gatti and Enrico Brambilla. Heralding pure single photons: A comparison between counterpropagating and copropagating twin photons. *Phys. Rev. A*, 97:013838, Jan 2018.

[18] Nijil Lal, Anindya Banerji, Ayan Biswas, Ali Anwar, and R. P. Singh. Photon statistics of twisted heralded single photons. *Journal of Modern Optics*, 67(2):126–132, 2020.

[19] Sonia Buckley, Kelley Rivoire, and Jelena Vuckovic. Engineered quantum dot single-photon sources. *Reports on Progress in Physics*, 75(12):126503, 2012.

[20] H Jeff Kimble, Mario Dagenais, and Leonard Mandel. Photon antibunching in resonance fluorescence. *Physical Review Letters*, 39(11):691, 1977.

[21] P Michler, A Kiraz, C Becher, WV Schoenfeld, PM Petroff, Lidong Zhang, E Hu, and A Imamoglu. A quantum dot single-photon turnstile device. *Science*, 290(5500):2282–2285, 2000.

[22] Marlan O. Scully and M. Suhail Zubairy. *Quantum Optics*. Cambridge University Press, 1997.

[23] Michael Varnava, Daniel E Browne, and Terry Rudolph. How good must single photon sources and detectors be for efficient linear optical quantum computation? *Physical review letters*, 100(6):060502, 2008.

[24] H Fearn and R Loudon. Quantum theory of the lossless beam splitter. *Optics communications*, 64(6):485–490, 1987.

[25] Chong-Ki Hong, Zhe-Yu Ou, and Leonard Mandel. Measurement of subpicosecond time intervals between two photons by interference. *Physical Review Letters*, 59(18):2044, 1987.

[26] Richard Jozsa. Fidelity for mixed quantum states. *Journal of Modern Optics*, 41(12):2315–2323, 1994.

[27] Gregg Jaeger. *Quantum Information: An Overview*. Springer, 2007.

[28] D Leonard, M Krishnamurthy, CMv Reaves, Steven P DenBaars, and Pierre M Petroff. Direct formation of quantum-sized dots from uniform coherent islands of ingaas on gaas surfaces. *Applied Physics Letters*, 63(23):3203–3205, 1993.

[29] Claude Fabreet al. *Quantum Optics and Nanophotonics*. Oxford University Press, 2016.

[30] James Binney and David Skinner. *The physics of quantum mechanics*. Oxford University Press, 2015.

[31] Seungwon Lee, Olga L. Lazarenkova, Fabiano Oyafuso, Paul von Allmen, and Gerhard Klimeck. Effect of wetting layers on the strain and electronic structure of inas self-assembled quantum dots.

[32] Johann Reithmaier, Grzegorz Sęk, A Löffler, C Hofmann, S Kuhn, S. Reitzenstein, L Keldysh, Vladimir Kulakovskii, T Reinecke, and A Forchel. Strong coupling in a single quantum dot semiconductor microcavity system - art. no. 61151m. *Nature*, 432:197–200, 11 2004.

[33] Edward Mills Purcell. Spontaneous emission probabilities at radio frequencies. *Physical Review*, page 681, 1946.

[34] Howard Carmichael. *Statistical methods in quantum optics: master equations and Fokker-Planck equations*. Springer, 2011.

[35] Stefan A. Maier. *Plasmonics: fundamentals and applications*. Springer, 2007.

[36] Pochi Yeh. *Optical waves in layered media*. Wiley, 2005.

[37] Alexei A. Maradudin, J. Roy. Sambles, and William L. Barnes. *Modern plasmonics*. Elsevier, 2014.

[38] Joseph R. Lakowicz. Radiative decay engineering 5: Metal-enhanced fluorescence and plasmon emission. *Analytical Biochemistry*, 337(2):171–194, 2005.

[39] R. De L. Kronig, William George Penney, and Ralph Howard Fowler. Quantum mechanics of electrons in crystal lattices. *Proceedings of the Royal Society of London. Series A, Containing Papers of a Mathematical and Physical Character*, 130(814):499–513, 1931.

[40] Pochi Yeh, Amnon Yariv, and Chi-Shain Hong. Electromagnetic propagation in periodic stratified media. *J. Opt. Soc. Am.*, 67(4):423–438, Apr 1977.

[41] Robert D. Meade, Karl D. Brommer, Andrew M. Rappe, and J. D. Joannopoulos. Electromagnetic bloch waves at the surface of a photonic crystal. *Phys. Rev. B*, 44:10961–10964, Nov 1991.

[42] D Kossel. Analogies betwaeen thin-film optics and electron-band theory of solids. In *Journal of the Optical Society of America*, volume 56, page 1434. American Institute Physics Circulation Fulfillment, 1966.

[43] Pochi Yeh, Amnon Yariv, and Alfred Y Cho. Optical surface waves in periodic layered media. *Applied Physics Letters*, 32(2):104–105, 1978.

[44] Aleksei P Vinogradov, Aleksandr V Dorofeenko, Aleksandr M Merzlikin, and Aleksandr A Lisyansky. Surface states in photonic crystals. *Physics-Uspekhi*, 53(3):243–256, jun 2010.

[45] AP Vinogradov, AV Dorofeenko, SG Erokhin, M Inoue, AA Lisyansky, AM Merzlikin, and AB Granovsky. Surface state peculiarities in one-dimensional photonic crystal interfaces. *Physical Review B*, 74(4):045128, 2006.

[46] Felix J. Lawrence, Lindsay C. Botten, Kokou B. Dossou, R. C. McPhedran, and C. Martijn de Sterke. Photonic-crystal surface modes found from impedances. *Phys. Rev. A*, 82:053840, Nov 2010.

[47] Francisco Villa and JA Gaspar-Armenta. Electromagnetic surface waves: Photonic crystal–photonic crystal interface. *Optics communications*, 223(1-3):109–115, 2003.

[48] I Tamm. A possible binding of the electrons on a crystal surface. *Zh. Eksp. Teor. Fiz*, 3:34–35, 1933.

[49] SH Tsang, SF Yu, XF Li, HY Yang, and HK Liang. Observation of Tamm plasmon polaritons in visible regime from ZnO/Al_2O_3 distributed Bragg reflector–Ag interface. *Optics Communications*, 284(7):1890–1892, 2011.

[50] M. Parker, E. Harbord, A. Young, P. Androvitsaneas, J. Rarity, and R. Oulton. Tamm plasmons for efficient interaction of telecom wavelength photons and quantum dots. *IET Optoelectronics*, 12(1):11–14, 2018.

[51] ME Sasin, RP Seisyan, MA Kalitteevski, S Brand, RA Abram, JM Chamberlain, A Yu Egorov, AP Vasilev, VS Mikhrin, and AV Kavokin. Tamm plasmon polaritons: Slow and spatially compact light. *Applied physics letters*, 92(25):251112, 2008.

[52] C. Symonds, G. Lheureux, J. P. Hugonin, J. J. Greffet, J. Laverdant, G. Brucoli, A. Lemaitre, P. Senellart, and J. Bellessa. Confined Tamm Plasmon Lasers. *Nano Letters*, 13(7):3179–3184, 2013.

[53] Kane Yee. Numerical solution of initial boundary value problems involving Maxwell's equations in isotropic media. *IEEE Transactions on Antennas and Propagation*, 14(3):302–307, 1966.

[54] Uhrig R. The transfer matrix method seen as one method of structural analysis among others. *Journal of Applied Physics*, 42(9):136–148, 1966.

[55] Thomas H. Cormen, Charles E. Leiserson, Ronald L. Rivest, and Clifford Stein. *Introduction to algorithms*. MIT Press, 2014.

[56] Allen Taflove. *Computational electrodynamics : the finite-difference time-domain method*. Artech House, Boston, 2005.

[57] A. Taflove. Application of the finite-difference time-domain method to sinusoidal steady-state electromagnetic-penetration problems. *IEEE Transactions on Electromagnetic Compatibility*, EMC-22(3):191–202, 1980.

[58] Wenhua Yu and R. Mittra. A conformal finite difference time domain technique for modeling curved dielectric surfaces. *IEEE Microwave and Wireless Components Letters*, 11(1):25–27, 2001.

[59] K. L. Silverman, R. P. Mirin, S. T. Cundiff, and A. G. Norman. Direct measurement of polarization resolved transition dipole moment in InGaAs/GaAs quantum dots. *Applied Physics Letters*, 82(25):4552, June 2003.

[60] Jean-Pierre Berenger et al. A perfectly matched layer for the absorption of electromagnetic waves. *Journal of computational physics*, 114(2):185–200, 1994.

[61] J. Alan Roden and Stephen D. Gedney. Convolution PML (CPML): An efficient FDTD implementation of the CFS-PML for arbitrary media. *Microwave and Optical Technology Letters*, 27(5):334–339, 2000.

[62] S. D. Gedney and B. Zhao. An auxiliary differential equation formulation for the complex-frequency shifted PML. *IEEE Transactions on Antennas and Propagation*, 58(3):838–847, 2010.

[63] Edward D. Palik. *Handbook of optical constants of solids*. Academic Press, 1998.

[64] R. E. Fern and A. Onton. Refractive index of AlAs. *Journal of Applied Physics*, 42(9):3499–3500, 1971.

[65] P. B. Johnson and R. W. Christy. Optical constants of the noble metals. *Phys. Rev. B*, 6:4370–4379, Dec 1972.

[66] Mike Adams, Ben Cemlyn, Ian Henning, Matthew Parker, Edmund Harbord, and Ruth Oulton. Model for confined Tamm plasmon devices. *J. Opt. Soc. Am. B*, 36(1):125–130, Jan 2019.

[67] Matthew Parker, Edmund Harbord, Lifeng Chen, Edmund Clarke, Kenneth Kennedy, John Rarity, and Ruth Oulton. Telecommunication wavelength confined Tamm plasmon structures containing InAs/GaAs quantum dot emitters at room temperature. *Phys. Rev. B*, 100:165306, Oct 2019.

[68] Matthew Parker. Optical Tamm states for novel optical and quantum optical devices.